UNIVERSITÉ DE MONTRÉAL

AXIAL COMPRESSOR BLADE DESIGN FOR DESENSITIZATION OF AERODYNAMIC
PERFORMANCE AND STABILITY TO TIP CLEARANCE

ENGIN ERLER
DÉPARTEMENT DE GÉNIE MÉCANIQUE
ÉCOLE POLYTECHNIQUE DE MONTRÉAL

THÈSE PRÉSENTÉE EN VUE DE L'OBTENTION
DU DIPLÔME DE PHILOSOPHIÆ DOCTOR
(GÉNIE MÉCANIQUE)
DÉCEMBRE 2012

UNIVERSITÉ DE MONTRÉAL

ÉCOLE POLYTECHNIQUE DE MONTRÉAL

Cette thèse intitulée :

AXIAL COMPRESSOR BLADE DESIGN FOR DESENSITIZATION OF AERODYNAMIC PERFORMANCE AND STABILITY TO TIP CLEARANCE

présentée par : ERLER Engin
en vue de l'obtention du diplôme de : Philosophiæ Doctor
a été dûment acceptée par le jury d'examen constitué de :

M. REGGIO Marcelo, Ph.D., président
M. VO Huu Duc, Ph.D., membre et directeur de recherche
M. TRÉPANIER Jean-Yves, Ph.D., membre
M. ALLAN William D.E., DPhil, membre

Dedication

to my mother . . .

Acknowledgments

First of all, I would like to express my profound gratitude to my supervisor, Assoc. Prof. Huu Duc Vo, for the patient guidance, encouragement and invaluable advices that he has provided throughout my research project. As a supervisor, he responded to my questions but also his help to settle in Montreal is greatly appreciated.

I would like to thank the Pratt & Whitney Canada, not only for providing the project financial budged, but also for providing an opportunity to work in such an innovative project. In particular, I would like to thank Dr. Hong Yu for his valuable comments and suggestions.

I am grateful to have such nice roommates in my office and I want to thank them for their friendship. Especially, I want to thank Shubhankar Ghosh for his helps in Gambit, Javad Hosseini for his helps in French, Martial Dumas for his helps in CFX-Solver and French. Also, I would like to thank all my friends in Montreal for their support.

I am also very grateful to all jury members and those, who has given me friendship and provided me practical help. In particular, I would like to thank one of the jury members, Billy Allan, for his extensive comments on thesis organization.

Finally, I want to present my special thanks to my husband Eray Akcayoz, for his continued support and encouragement with his endless energy. Furthermore, I would like to send my gratitude to my mother, my sister and my grandparents for their spiritual support to study abroad.

Résumé

L'écoulement de jeu d'aube est l'écoulement qui passe à travers le jeu entre le bout de l'aube du rotor et le carter d'une turbomachine, tels qu'un compresseurs ou une turbine. Cet écoulement est entraîné par la différence de pression à travers l'aube (charge aérodynamique) dans la région du bout de l'aube et constitue une source majeure de perte de performance et de stabilité aérodynamique des compresseurs axiaux de moteurs d'avions modernes. Une augmentation du jeu d'aube peut survenir de façon temporaire en raison de la dilatation différentielle radiale entre l'aube et le carter en opération transitoire ou permanente en raison de l'usure du moteur ou à cause des tolérances de fabrication sur de petites aubes. Cette augmentation augmente l'écoulement de jeu d'aube et se traduit par une plus grande consommation de carburant et un risque plus élevé de calage du moteur. Une conception du compresseur qui permet de réduire la sensibilité de la performance et stabilité aérodynamique de ce dernier à l'augmentation du jeu d'aube aurait un impact majeur à court et à long terme sur la performance et l'enveloppe d'opération du moteur. Alors que de nombreuses recherches ont été menées sur l'amélioration de la performance nominale du compresseur, peu a été fait sur la désensibilisation à l'accroissement du jeu d'aube au-delà des observations isolées que certains designs d'aubes, comme l'inclinaison amont en corde, semblent être moins sensibles à l'augmentation du jeu d'aube. Ce projet vise à identifier à travers une étude numérique les caractéristiques de l'écoulement et les mécanismes associés qui réduisent la sensibilité des rotors de compresseurs axiaux au jeu d'aube et à proposer des stratégies de conception de lames qui exploitent ces résultats.

La méthodologie commence par la conception d'un rotor de compresseur axial conventionnel de référence suivie d'une étude paramétrique avec des variations de ce design par la modification de la ligne de cambrure et de la ligne d'empilage des profils de pale long de l'envergure. Il est à noter que la méthode de désensibilisation la plus simple serait de réduire la charge aérodynamique dans la région du bout de l'aube, ce qui réduirait l'écoulement de jeu d'aube et la proportion de sa contribution à la perte de performance. Cependant, avec la plus grande partie du travail sur l'écoulement qui se fait dans cette région, cette approche entraînerait une pénalité de la performance nominale. Par conséquent, la philosophie choisie de conception du rotor vise à maintenir le chargement aérodynamique constant le long de l'envergure de l'aube pour éviter de sacrifier performance au profit de la désensibilisation. Les designs résultant de cet exercice sont simulées dans ANSYS CFX à différentes tailles de jeu d'aube. La variation de leur performance par rapport à la taille du jeu (sensibilité) est comparée au niveau intégral en termes de rapport de pression et de rendement adiabatique, ainsi qu'au niveau détaillé en termes de pertes aérodynamiques et de blocage liés à l'écoulement de jeu d'aube. La sensibilité de la stabilité aérodynamique est évaluée soit di-

rectement par le biais des simulations de la caractéristique du rotor jusqu'au point de décrochage (coûteux en temps et en ressources) pour quelques designs ou indirectement par la position de l'interface entre l'écoulement entrant et celui de jeu d'aube par rapport au plan du bord d'attaque du rotor. Cette dernière approche est basée sur un critère de décrochage qui est généralement observé dans compresseurs axiaux modernes. Les designs de rotors sont ensuite évalués en fonction de leur sensibilité par rapport à celle du rotor de référence pour détecter les caractéristiques qui peuvent expliquer la tendance observée de la sensibilité au jeu d'aube. Ces caractéristiques peuvent alors être validées et les mécanismes associés expliqués via des simulations numériques de l'écoulement et la modélisation.

L'analyse de la base de données de l'étude paramétrique du rotor montre que la tendance observée de sensibilité ne peut pas être expliquée par le déplacement de la charge aérodynamique le long de la corde de l'aube, une hypothèse initiale basée sur la revue de la littérature. Par contre, deux caractéristiques de l'écoulement ont été trouvées pour réduire la sensibilité de la performance et de la stabilité à l'agrandissement du jeu d'aube: une augmentation de la quantité de mouvement méridional entrant dans la région du bout de l'aube et une réduction/élimination du double écoulement de jeu d'aube. Le double écoulement de jeu d'aube est l'écoulement qui sort du jeu d'une aube pour ensuite entrer dans le jeu de l'aube adjacent au lieu de convecter en aval hors du passage d'aube local. Ces caractéristiques de l'écoulement sont isolés et validés en se basant sur le design de référence du rotor par des changements dans la condition de pression totale d'entrée pour modifier la quantité de mouvement entrant et du nombre d'aubes afin de varier la quantité de double écoulement de jeu d'aube. Au niveau du mécanisme, le double écoulement de jeu d'aube s'avère nuisible à la performance et la stabilité, et l'augmentation de sa proportion suite à un agrandissement du jeu d'aube, explique l'augmentation de la sensibilité en sa présence, et à l'inverse, la désensibilisation qui résulte de sa réduction ou de son élimination. L'augmentation de la quantité de mouvement méridional entrant dans la région du bout de l'aube réduit la sensibilité au jeu d'aube via sa réduction du double écoulement de jeu d'aube ainsi que par un mélange amélioré avec l'écoulement de jeu d'aube, tel que démontré par un modèle analytique sans double écoulement de jeu d'aube.

Les résultats ci-dessus impliquent que toute stratégie de conception des aubes qui exploite les deux caractéristiques de désensibilisation permettrait de réduire la sensibilité de la performance et de la stabilité au jeu d'aube. L'augmentation de la quantité de mouvement méridional entrant dans la région du bout de l'aube peut être réalisée par l'inclinaison amont en corde de l'aube. La diminution du double écoulement de jeu d'aube peut être obtenue par la réduction de l'angle de décalage des aubes dans la région près du carter. Des exemples de designs associés à ces stratégies sont présentés et leur réduction avec succès de la sensibilité au jeu d'aube est démontrée avec des simulations CFX.

Abstract

Tip clearance flow is the flow through the clearance between the rotor blade tip and the shroud of a turbomachine, such as compressors and turbines. This flow is driven by the pressure difference across the blade (aerodynamic loading) in the tip region and is a major source of loss in performance and aerodynamic stability in axial compressors of modern aircraft engines. An increase in tip clearance, either temporary due to differential radial expansion between the blade and the shroud during transient operation or permanent due to engine wear or manufacturing tolerances on small blades, increases tip clearance flow and results in higher fuel consumption and higher risk of engine surge. A compressor design that can reduce the sensitivity of its performance and aerodynamic stability to tip clearance increase would have a major impact on short and long-term engine performance and operating envelope. While much research has been carried out on improving nominal compressor performance, little had been done on desensitization to tip clearance increase beyond isolated observations that certain blade designs such as forward chordwise sweep, seem to be less sensitive to tip clearance size increase. The current project aims to identify through a computational study the flow features and associated mechanisms that reduces sensitivity of axial compressor rotors to tip clearance size and propose blade design strategies that can exploit these results.

The methodology starts with the design of a reference conventional axial compressor rotor followed by a parametric study with variations of this reference design through modification of the camber line and of the stacking line of blade profiles along the span. It is noted that a simple desensitization method would be to reduce the aerodynamic loading of the blade tip which would reduce the tip clearance flow and its proportional contribution to performance loss. However, with the larger part of the work on the flow done in this region, this approach would entail a nominal performance penalty. Therefore, the chosen rotor design philosophy aims to keep the spanwise loading constant to avoid trading performance for desensitization. The rotor designs that resulted from this exercise are simulated in ANSYS CFX at different tip clearance sizes. The change in their performance with respect to tip clearance size (sensitivity) is compared both on an integral level in terms of pressure ratio and adiabatic efficiency, as well as on a detailed level in terms of aerodynamic losses and blockage associated with tip clearance flow. The sensitivity of aerodynamic stability is evaluated either directly through the simulations of the rotor characteristics up to the stall point (expensive in time and resources) for a few designs or indirectly through the position of the interface between the incoming and tip clearance flow with respect to the rotor leading edge plane. The latter approach is based on a generally observed stall criteria in modern axial compressors. The rotor designs are then assessed according to their sensitivity in comparison to that of the reference rotor design to detect features that can explain the trend in sensitivity to tip clearance size. These

features can then be validated and the associated flow mechanisms explained through numerical simulations and modelling.

Analysis of the database from the rotor parametric study shows that the observed trend in sensitivity cannot be explained by the shifting of the aerodynamic loading along the blade chord, as initially hypothesized based on the literature review. Instead, two flow features are found to reduce sensitivity of performance and stability to tip clearance, namely an increase in incoming meridional momentum in the tip region and a reduction/elimination of double leakage flow. Double leakage flow is the flow that exits the tip clearance of one blade and proceeds into the clearance of the adjacent blade rather than convecting downstream out of the local blade passage. These flow features are isolated and validated based on the reference rotor design through changes in the inlet total pressure condition to alter incoming flow momentum and blade number count to change double leakage rate. In terms of flow mechanism, double leakage is shown to be detrimental to performance and stability, and its proportional increase with tip clearance size explains the sensitivity increase in the presence of double leakage and, conversely, the desensitization effect of reducing or eliminating double leakage. The increase in incoming meridional momentum in the tip region reduces sensitivity to tip clearance through its reduction of double leakage as well as through improved mixing with tip clearance flow, as demonstrated by an analytical model without double leakage flow.

The above results imply that any blade design strategy that exploits the two desensitizing flow features would reduce the performance and stability sensitivity to tip clearance size. The increase of the incoming meridional momentum can be achieved through forward chordwise sweep of the blade. The reduction of double leakage without changing blade pitch can be obtained by decreasing the blade stagger angle in the tip region. Examples of blade designs associated with these strategies are shown through CFX simulations to be successful in reducing sensitivity to tip clearance size.

Table of Contents

List of Figures

List of Tables

List of Appendices

Nomenclature

Variables

Latin

a	Speed of sound
A	Area
C	Coefficient
c	chord
h	Enthalpy per mass
k	Thermal conductivity or turbulent kinetic energy in $k - \omega$ and $k - \epsilon$ models
l	Turbulence length
M	Mach number
$\dot{m}$	Mass flow rate
P	Pressure
PR	Pressure Ratio
R	Radius
r	Radial coordinate
Re	Reynolds number
S	Static Entropy
s	Static Entropy per unit mass
SM	Stall Margin
T	Temperature
Tu	Turbulent intensity
U	Rotational speed
u	Velocity in x-axis
v	Velocity in y-axis
V	Velocity
w	Velocity in z-axis
x	Axial coordinate
y	Pitchwise coordinate
z	Cartesian coordinate normal to (x,y) plane
y^+	Non-dimensionalized boundary layer coordinate

Greek

α	Absolute frame flow angle
β	Relative frame flow angle
Δ	Change or difference
ϵ	Turbulent dissipation in $k - \epsilon$ model
Φ	Dissipation rate
φ	Flow coefficient
γ	Heat capacity ratio
η	Efficiency
μ	Dynamic viscosity
θ	Circumferential coordinate
ρ	Density
Ω	Angular velocity (rpm)
ω	Angular velocity (rad/s) or specific turbulent dissipation in $k - \omega$ model
ψ	Enthalpy based loading coefficient
ζ	Tip clearance

Subscripts

b	Blockage
c	Corrected
e	Edge
d.l.	Double leakage flow
gen	Generated
in	Inlet
int	Incoming/ tip clearance flow interface
m	Meridional
max	Maximum
min	Minimum
p	Pressure
ref	Reference
rel	Relative
s	Static
ss	Suction side
str	Streamwise
t	Total

tip	Blade tip plane
t.c.	Tip clearance flow
tc	Tip clearance flow
t.l.	Total tip leakage flow
ts	Total-to-Static
tt	Total-to-Total

Abbreviations

ACS	Aft Chordwise Sweep
BASE	Baseline Blade
BAS	Backward Axial Sweep
BL	Backward Lean
CFD	Computational Fluid Dynamics
DNS	Direct Numerical Simulation
DL	Double Leakage Flow
DP	Design Point
FAS	Forward Axial Sweep
FC	Forward Camber
FCS	Forward Chordwise Sweep
FFCS	Full Forward Chordwise Sweep
FL	Forward Lean
HMMT	High Meridional Momentum at Tip
LE	Leading Edge
LES	Large Eddy Simulation
LMMT	Low Meridional Momentum at Tip
ND	Negative Dihedral
OP	Operating Point
PD	Positive Dihedral
PLS	Partially Low Stagger
PS	Pressure Side
PWC	Pratt & Whitney Canada
RANS	Reynolds Averaged Navier Stokes
SS	Suction Side
SST	Shear Stress Transport
TE	Trailing Edge

TL   Double Leakage Flow

VHMMT   Very High Meridional Momentum at Tip

Introduction

0.1 Background

   Axial compressors are major and crucial components of modern aircraft gas turbine engines. As shown in Figure 0.1, a typical axial compressor is composed of many stages, each of which has axially oriented rotational and stationary blades, named rotor and stator blades. A major parameter affecting the compressor performance and aerodynamic stability is the tip clearance, which is the clearance between the tip of the rotor and the stationary casing. It should be noted that there may also be a clearance between the stator and the hub for a cantilevered stator blade design, but this case is not common in modern compressors. Increased tip clearance resulting from differential thermal expansion between the casing and rotor blade encountered during transient excursions such as take-off, and from wear caused by rubbing during operational life, is highly detrimental to engine stability and fuel consumption. To appreciate the effects of tip clearance on engine aerodynamic performance and stability, this section briefly reviews the workings of an axial compressor.
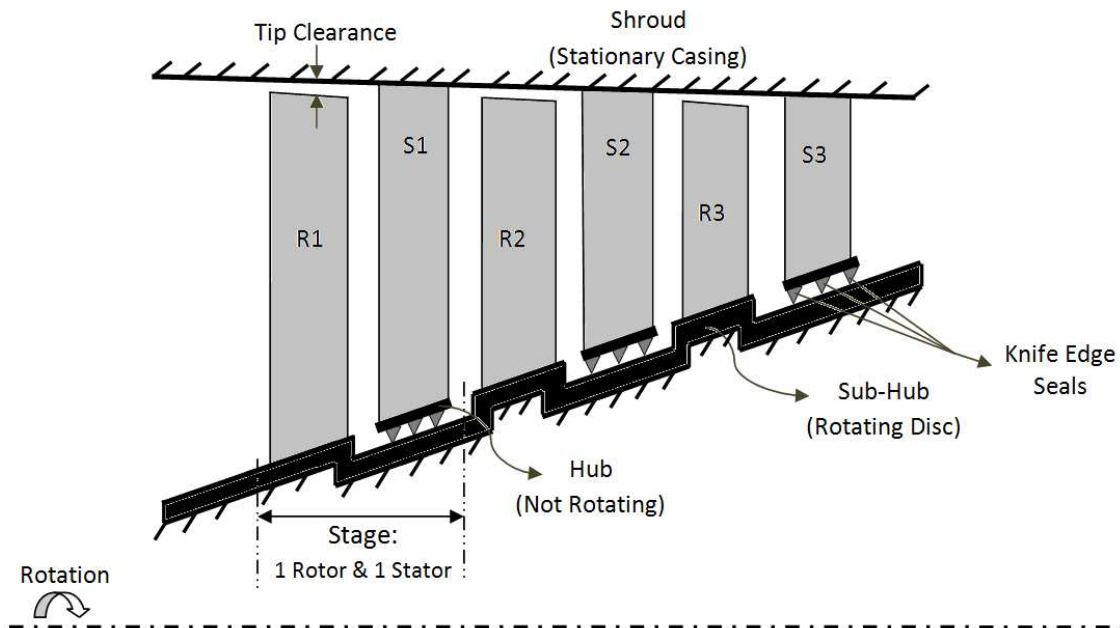
Figure 0.1: Schematic of a modern axial compressor

   Figure 0.2 shows a constant span cut of a simplified axial compressor stage. The velocity vectors in blue are in the stationary frame while those in red are in the rotating frame of the rotor and the velocity linking the two reference frames is the local circumferential rotor blade velocity

(U) vector, shown in black. The combination is referred to as a velocity triangle. It can be seen that the rotor and stator blade passages are laid out in their respective frame of reference as diffusers with increasing normal passage areas to increase the static pressure. However, the flow deflection of the rotor in the relative frame, combined with its rotation, translates into increased absolute flow velocity exiting the rotor. Thus, that is then converted into static pressure rise through the stator.
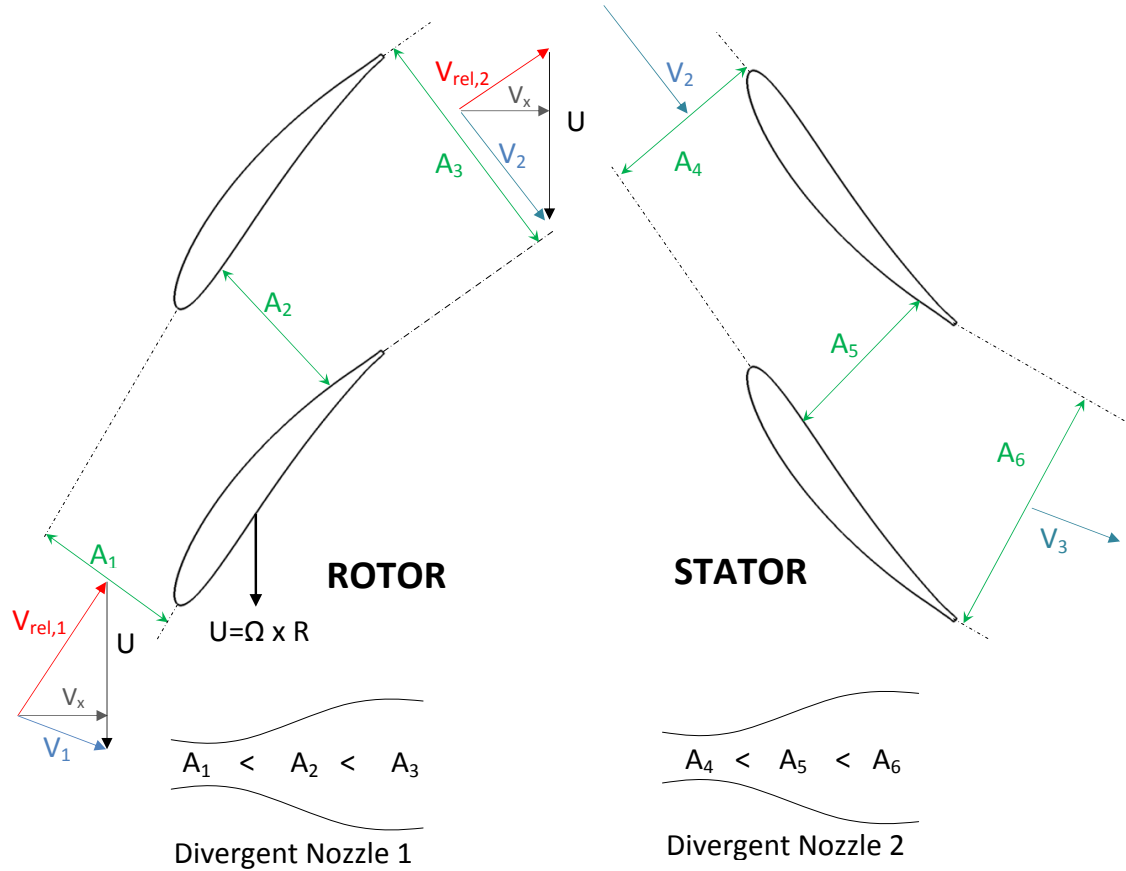
Figure 0.2: Rotor and stator blade profiles

From the above simplified two-dimensional (2D) explanation of axial compressor operation, one can already infer two factors that will reduce compressor performance as measured by pressure rise and efficiency. The first factor is the presence of boundary layers. The displacement thickness of the boundary layers reduces the effective area increase through the blade passages, causing reduced pressure rise. The viscous shear and mixing losses associated with the boundary layer also causes reduction in total pressure and consequently compression efficiency. It will later be seen that the rotor tip clearance will add similar three-dimensional (3D) aerodynamic effects.

The second factor reducing performance is off-design operation. Similar to an airfoil, there is an angle between the incoming flow velocity and airfoil leading edge called incidence angle) that will give the lowest loss and thus optimum efficiency. It can be inferred from Figure 0.2 that for a

particular compressor geometry at a given rotation speed (U), there is a mass flow, or axial velocity, that will give the optimum incidence angle and thus efficiency. Figure 0.3(a) shows the mass flow versus pressure ratio and efficiency at a constant speed (referred to as a speedline) to illustrate the effect of changing the axial velocity. At high mass flow (Figure 0.3(c)), the incidence angle to the rotor becomes negative with the relative inlet velocity increase. The increase in effective area across the rotor blade passage, and thus the pressure rise, is reduced, leading to choking of the passage when the local velocity reaches Mach 1 (like a convergent-divergent nozzle). Alternatively, when mass flow reduces below the design value, the thickness of boundary layer on the blade suction side and associated losses increase, countering the positive effect of increased effective area ratio, and the pressure rise starts to level-off with decreasing mass flow until sooner or later the boundary layer separates and aerodynamic instabilities, such as rotating stall can occur. This leftmost point on the speedline in Figure 0.3(a) is usually called the stall point (or sometimes surge point). The difference in flow value between choke and stall is usually referred to as the flow range and the difference in flow value between design point and stall is usually called the stall margin.

Rotating stall is an aerodynamic instability characterized by the formation a velocity deficiency that rotates at 50-70% of the compressor rotor speed which results in a drop in pressure rise (Vo *et al.*, 2008). Within an engine, rotating stall in the compressor usually triggers another more damaging aerodynamic instability called surge. Surge is an axisymmetric oscillation in mass flow across the entire engine and results in a sudden drop in power output, and often engine damage (Greitzer, 1976). The stability of a compressor is determined by stall margin and/or flow range.

The effects of off-design conditions can be also deduced from a compressor map, which is simply composed of different speedlines, as illustrated in Figure 0.4 where the optimum efficiency and pressure rise of design point both reduce with speed. The line that links the stall point of each speedline is called the surge or instability line and the line along which the compressor operates as the speed of the engine increases is called the operating or running line. The distance between the two lines is referred to as the surge margin, which is a safety margin left to account for the fact the running line curves upward during rapid engine acceleration and the surge line drops when the intake air is not uniform such as during cross-winds or when the tip clearance increases.

In a multi-stage compressor, the effect of off-design operation in one stage is greatly amplified. The compressor is designed such that the engine operates most of the time at the design point or *DP*, where all the stages operate at optimum efficiency. This is often called stage matching. At other operating conditions, in other words when a stage is not operating at its design point, the inlet conditions to the downstream stages are off-design as well, accumulating the negative effect on pressure rise and efficiency, even stalling or choking certain stages may occur. Figure 0.5 illustrates stage mismatch in a multistage compressor resulting from off-design operation. In this example, the compressor operates at a lower-speed such that first stage has reduced pressure rise.
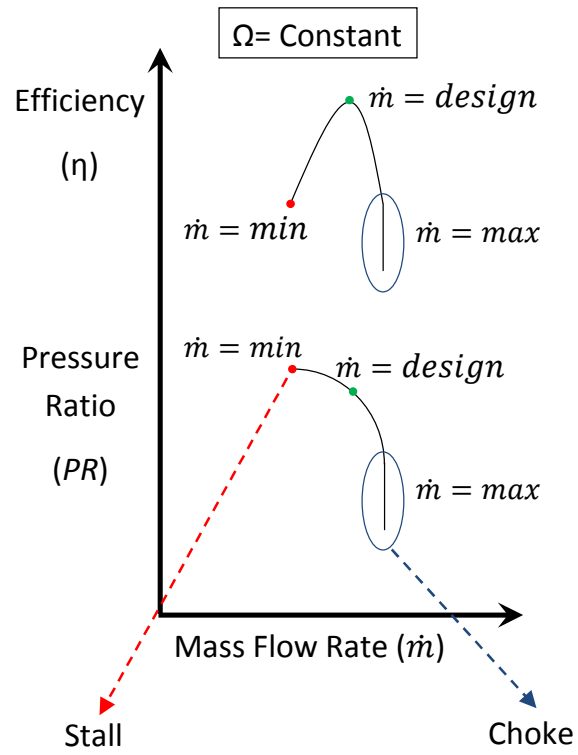
(a)
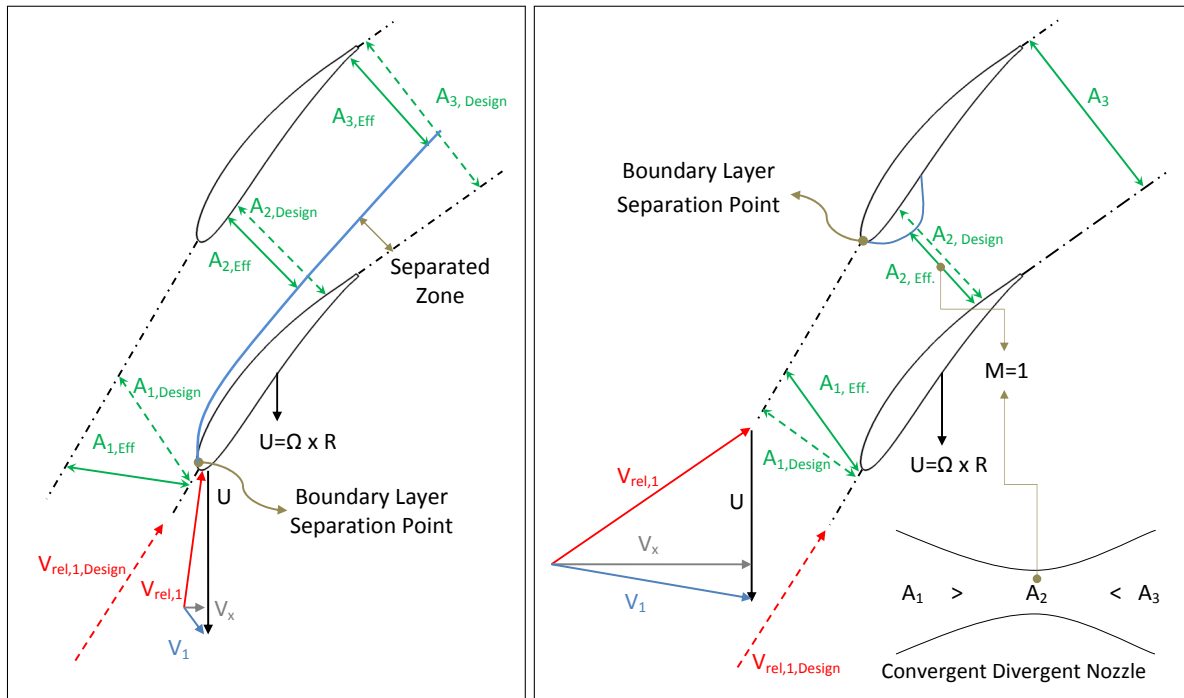
(b)

(c)

Figure 0.3: Off-design conditions
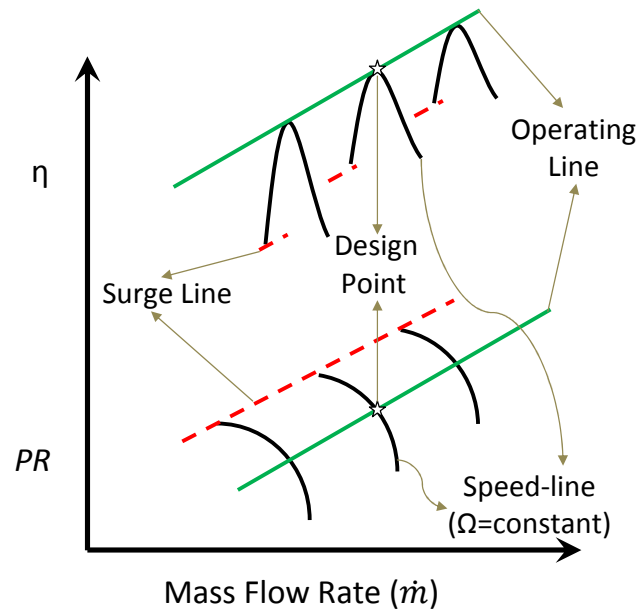
Figure 0.4: Schematic of a compressor map

As a result, the density of the air entering the second stage is smaller than the design value. Thus, the incoming velocity to the second stage is high resulting in choking of the second stage or of a downstream stage.
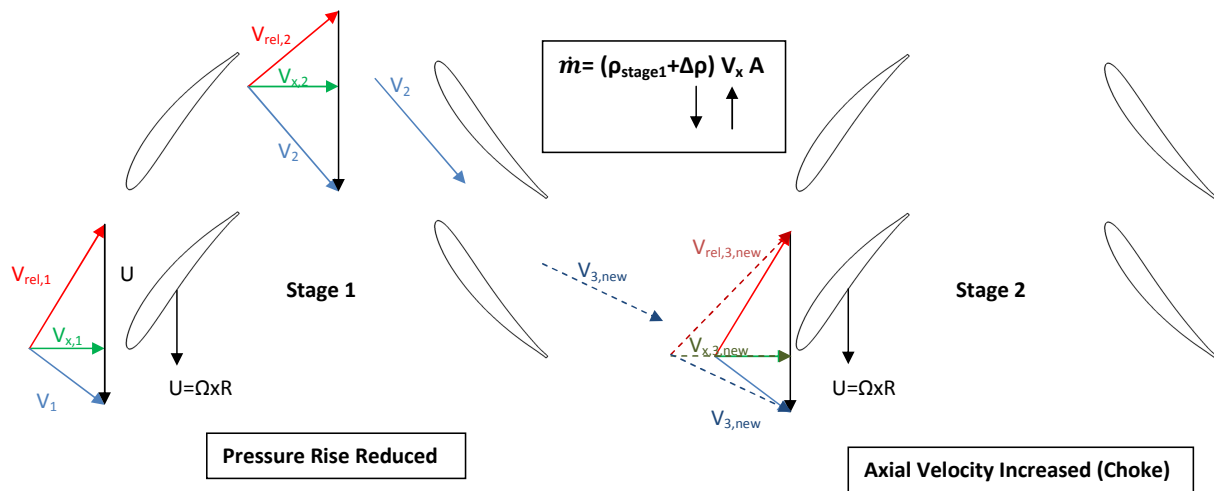
Figure 0.5: Effect of under-performed first stage on stage mismatching

0.2   The Problem of Tip Clearance

Section 1.1 described the compressor's working, performance and stability loss from a 2D perspective. In a real compressor, 3D effects brought about by tip clearance are major factors that come into play. Across the clearance between the rotor blade tip and the shroud, the pressure difference between the pressure side and the suction side of the blade induces a flow through the tip clearance, called tip clearance flow or tip leakage flow, from the pressure side to the suction side. This flow exiting the tip clearance interacts with the incoming flow to form a tip vortex and creating performance and stability losses as illustrated in Figure 0.6. The first source of performance loss induced by tip clearance flow is a shear/mixing loss. This loss is caused by the interaction and mixing of tip clearance flow with the incoming flow, which are almost perpendicular to each other, and it decreases the relative stagnation pressure (Storer and Cumpsty, 1994). This stagnation pressure loss creates losses in pressure rise and compressor efficiency. The second source of performance loss linked to tip clearance flow is the blockage which is a type of displacement thickness resulting from the momentum deficit in the streamwise direction. The blockage decreases the effective area, thus reduces the static pressure rise. Moreover, low streamwise velocity exiting the rotor tip region results in high incidence on the downstream stator, inducing an early stator stall. Therefore, the stall margin of the stage is reduced.
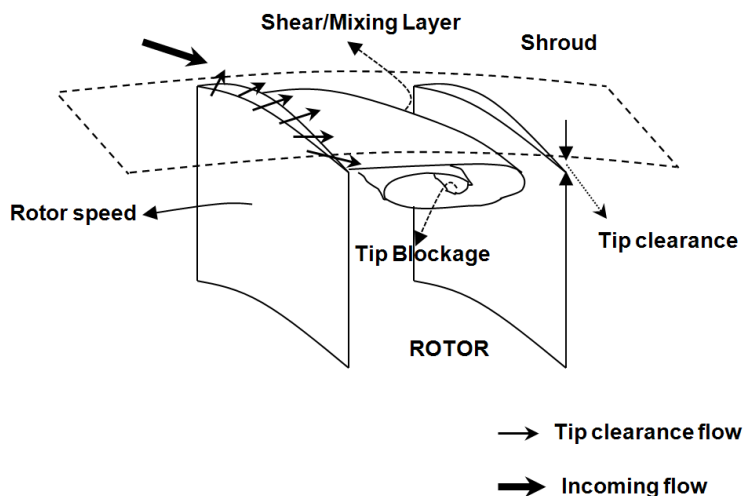
Figure 0.6: Schematic of tip clearance flow (Vo, 2001)

The detrimental effects of tip clearance flow on compressor performance and stability increases with tip clearance. Wisler (1985) demonstrated the effect of tip clearance on static pressure rise and efficiency on a low-speed axial compressor stage. A tip clearance increase from 1.38% span to 2.80% span decreased the peak efficiency by 1.5 percentage points, stall-margin by 11% and peak pressure rise by 9.7%.
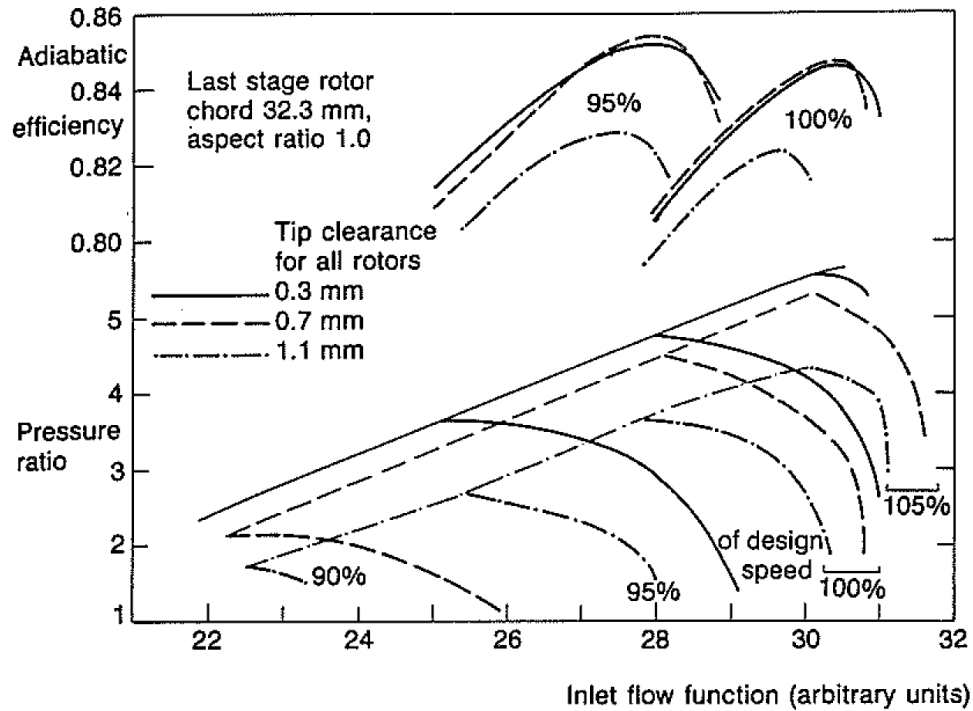
Figure 0.7: Effect of tip clearance and speed in a high-speed axial compressor (Freeman, 1985)

As speed increases, the effects of tip clearance flow are amplified. When the tip clearance from 0.3 mm to 1.1 mm in a high speed compressor, Freeman (1985) noted that flow range limitation becomes 3% and the peak efficiency drop became 2 percentage points. Figure 0.7 plots the compressor map of a high-speed axial compressor using four speed-lines (90%, 95%, 100%, 105%) for three different tip clearances (0.3 mm, 0.7 mm and 1.1 mm). It can be observed from Figure 0.7 that increasing tip clearance increases inclination of surge line at higher speeds. Thus, increasing tip clearance reduces flow range more drastically at higher speeds.

Furthermore, variation of tip clearance induces mismatching of stages. Domercq and Escuret (2007) explained this phenomena that increasing tip clearance increases the loss and the blockage causing the front stages to operate closer to the surge limit to compensate the pressure losses and the latter stages to operate inefficiently due to increased blockage at inlet. For example, Figure 0.8 shows pressure rise graphs for a two-stage axial compressor at nominal and high tip clearances. Figure 0.8(a) plots the first scenario, where the increase of tip clearance from nominal to high causes the pressure rise drop at the first stage and lower density in the entrance of second stage causes the second stage to work at a near choked condition. Moreover, increased blockage (due to tip clearance increase) from first stage lowers performance of second stage. Figure 0.8(b) plots the second scenario, where the first stage tries to compensate for lower pressure rise from both stages and works near stall. Again, the second stage is expected to work more inefficiently due to higher blockage upstream due to the first stage working near stall.
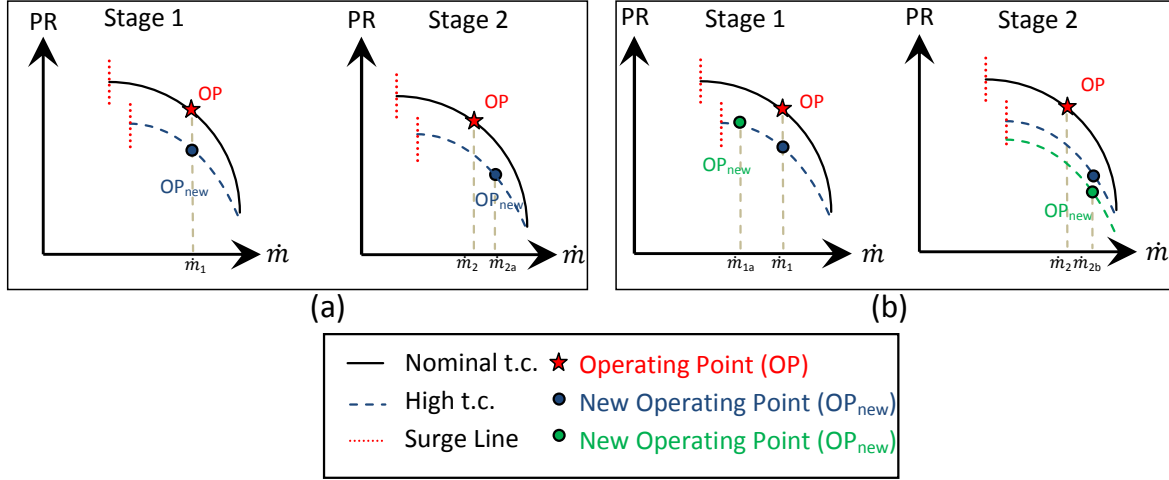
Figure 0.8: Effect of tip clearance increase on stage matching

In summary, many experimental and numerical studies have proved that increasing tip clearance decreases the efficiency, static and total pressure rise, maximum attainable pressure rise, and flow range. Changing operating conditions, such as increasing speed or increasing pressure rise amplifies effect of tip clearance. Moreover, increasing tip clearance induces mismatching and leads to under-performance in latter stages for tip clearances greater than 1% of chord in size (Cumpsty, 1989). However, the current design trend tends toward higher engine bypass ratio with more compact engine cores, resulting in small blades for which tip clearances 1% of chord become mechanically impractical to manufacture. Thus, there is a need to make compressor performance and stability less sensitive to tip clearance.

0.3   Research question

How can losses in performance and stability margin associated with tip clearance increase be reduced?

0.4   Motivation and Objectives

One obvious method to diminish performance and stability sensitivity to tip clearance is to reduce the aerodynamic loading (flow turning) in the tip region of the rotor since this loading directly influences tip clearance flow. However, since most of the work on the flow is done in the tip region, this method entails a penalty in nominal compressor performance. The challenge is to desensitize the compressor to tip clearance without comprising nominal performance.

Consequently, the objectives of this research are:

1. Identifying flow features and associated physical mechanisms that reduces performance loss and stability margin loss associated with tip clearance increase without reducing aerodynamic loading in the tip region,

2. Proposing blade design characteristics that exploit these flow features.

0.5   Outline of the Thesis

This thesis consists of five chapters. Following this introductory chapter, Chapter 2 presents a literature review of the physics of tip clearance flow and design features to reduce tip clearance losses as well as some previous work on performance desensitization to tip clearance. In Chapter 3, the methodology of the present research is presented, followed by the results in Chapter 4. Chapter 5 gives the conclusions and future work.

Chapter 1

Literature Review

There are few references in the open research literature that deal explicitly with reducing the sensitivity of compressor performance to tip clearance. Thus this chapter will start with a literature review of the research on the flow physics associated with tip clearance flow and blade design features adopted to increase performance and stability that can provide important clues for the current research. The literature review will conclude with the few references more directly linked to tip desensitization.

1.1   Tip Clearance Flow Physics

The effects of tip clearance flow have been studied since the 1970s. The review of those studies can be found in Wisler (1985) and Freeman (1985). However, studies on the physics of tip clearance flow and its relation to compressor losses and stability started in the 1990s.

Storer and Cumpsty (1991) analyzed the tip clearance flow experimentally and suggested decomposing the tip clearance flow velocity vectors at the exit of the tip clearance into tangential and normal components with respect to the local blade camber, as shown in Figure 1.1. The tangential component is the streamwise velocity in the core flow region closest to the blade tip at the local chord position. The normal component is induced by the pressure difference between the pressure side and the suction side of the blade tip. Therefore, the normal component, which is the tip clearance flow, is essentially a pressure-driven inviscid flow. A simple model is suggested to calculate the magnitude and the direction of the tip clearance flow velocity vectors, where the tangential component can be calculated from the oncoming axial velocity and blade camber, and the normal component can be derived from the pressure difference between pressure side and suction side. Moreover, they analyzed different tip clearances and concluded that, the pattern of blade loading and tip clearance flow are strongly related and these parameters are nearly invariant with tip clearance. However, the strength and size of the tip vortex increase with the tip clearance.

In a second paper, Storer and Cumpsty (1994) analyzed in detail the sources of losses associated with tip clearance flow. They specified that these losses can be classified under two categories; tip shear layer loss and tip blockage. The tip shear layer loss is caused by mixing of the tip clearance flow with the incoming flow which have different velocity magnitudes and directions, as shown by
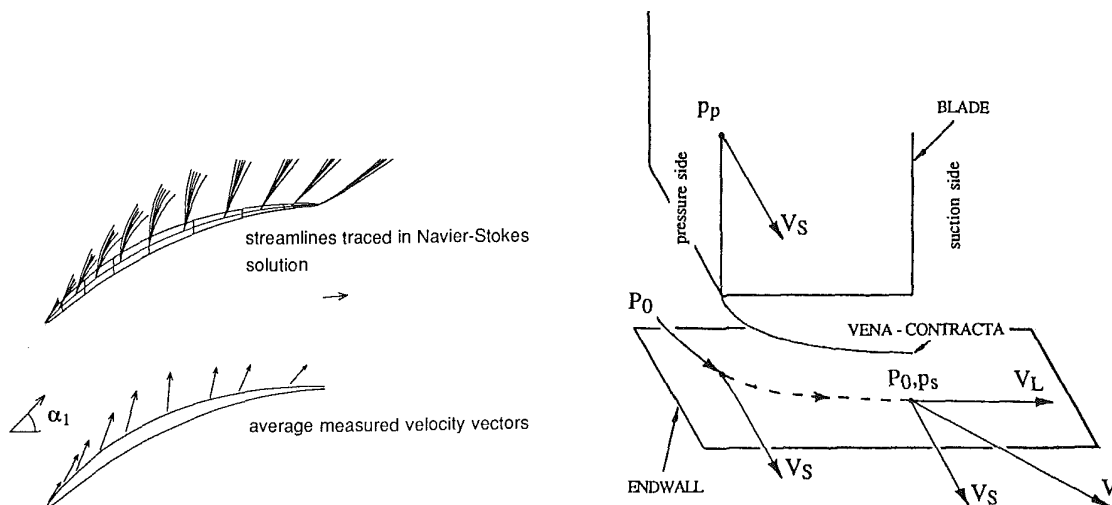
Figure 1.1: Tip clearance flow vectors (Storer and Cumpsty, 1991)

the schematic on the left illustration of Figure 1.2 and by the contours of viscous dissipation on the right plot of Figure 1.2, which is an evidence of a shear/mixing layer. The authors showed that most of the loss at the blade tip is caused by this shear/mixing layer and estimated this loss empirically. The tip blockage, on the other hand, is considered as a momentum-deficit caused by the tip shear layer loss, resulting in a reduction in effective passage area.

Tip blockage is studied extensively by Khalid *et al.* (1999). They suggested a formulation for quantifying blockage in the three-dimensional flow at the exit plane of the blade passage. They also proposed a model/mechanism for blockage generation and growth in a compressor blade passage in the form of a one-dimensional (1D) wake, which is equivalent to a 3D displacement thickness. The simplified model shown in Figure 1.3(a) suggests that the fluid exiting the tip clearance at leakage angle and total pressure, which can be determined from Storer and Cumpsty (1991), travels in a straight line until it meets the free stream flow. A control volume analysis of the mixing between the two streams with mass and momentum balance yields the size and direction of the blockage or velocity deficit. Next, the blockage is modelled as a wake moving up a pressure gradient, as seen in Figure 1.3(b), where the pressure gradient models the subsequent pressure rise at the rotor exit plane. The growth of blockage, between the mixing point and the exit plane, can be computed by a 2D integral wake analysis. Khalid (1995) compared values of blockage calculated using this simplified model, with values of blockage calculated via Computational Fluid Dynamics (CFD) simulations, wind-tunnel tests and rotating rig tests for different low-speed axial compressor/fan geometries and loadings with small (1.4% span) and large tip clearances (3% span). He found that the proposed blockage model reproduced the trends of CFD and wind tunnel tests, but slightly overestimated the tip blockage value. He concluded that the proposed model was good tool for fast estimates of tip blockage.

Figure 1.2: Shear/mixing layer representation (Storer and Cumpsty, 1994)

(a) Simplified blockage development

(b) Wake moving in pressure gradient

Figure 1.3: Blockage model (Khalid *et al.*, 1999)

Suder (1998) carried out a computational study of blockage development in a transonic compressor. His first conclusion was that the pressure and temperature rise near the end-wall region were directly related to tip blockage. Secondly, the tip blockage increased with blade loading, which was consistent with Khalid's study. Additionally, Suder (1998) analyzed the shock losses due to shock/tip leakage vortex interaction and shock/boundary layer interaction. The authors concluded that the shock strength and location had no direct relation to the tip blockage, but they have a direct effect on the blockage and associated losses induced by blade boundary layer.

Other research has investigated the role of tip clearance flow on aerodynamic instabilities in compressors, particularly rotating stall. The compressors for which rotating stall inception, as opposed to blade/hub boundary layer separation, is associated with tip clearance flow are usually referred to as tip-critical compressors. This is the case for most modern axial compressors. There are two known causes of rotating stall, and tip clearance flow can play a role in both. The first is called modal stall inception and is characterized by the relatively slow growth of circumferential flow perturbations into rotating stall cells when the stagnation-to-static pressure rise speedline reaches a zero-slope peak (Camp and Day, 1998). Moore and Greitzer (1986) showed that the positive slope of this speedline indicates negative damping of naturally-occurring perturbations, which grow into fully-developed rotating stall cells. A positive speedline slope can be caused by blockage and losses from the boundary layers or from tip clearance flow (Vo *et al.*, 2008). The other known, and most common, cause of rotating stall is spike stall inception, which is characterized by the formation of a localized sharp disturbance in the rotor tip region and its very rapid growth into a rotating stall cell. It occurs when the slope of the stagnation-to-static speedline is still negative (i.e. prior to the satisfaction of the criterion for modal stall inception). Day (1993) and Camp and Day (1998) showed experimentally that there was a critical rotor tip incidence for spike stall to occur, such that increasing tip clearance or reducing rotor tip incidence can cause change of spike to modal stall inception. Spike stall inception has been linked to tip clearance flow but the mechanism is not yet fully understood. However, recent research has proposed promising criteria based on tip clearance flow physics for predicting spike stall inception.

For low-speed axial compressors, Vo *et al.* (2008) proposed two criteria for spike stall inception based on a computational study of a low-speed axial compressor rotor. The first criterion is linked to the interface between the incoming flow and tip clearance flow, whose position is the result of a momentum balance between the low-entropy incoming and high-entropy tip clearance flow (Khalid *et al.*, 1999). As such, this interface is seen as a region of high entropy gradient. It moves toward the leading edge plane, as mass flow decreases, as a result of increased momentum of the tip clearance flow due to higher blade loading from increased blade incidence, and reduced momentum of the incoming flow. The first criterion is when this interface reaches the rotor tip leading edge plane as shown on the left of Figure 1.4(a), which marks the onset of tip clearance flow spillage
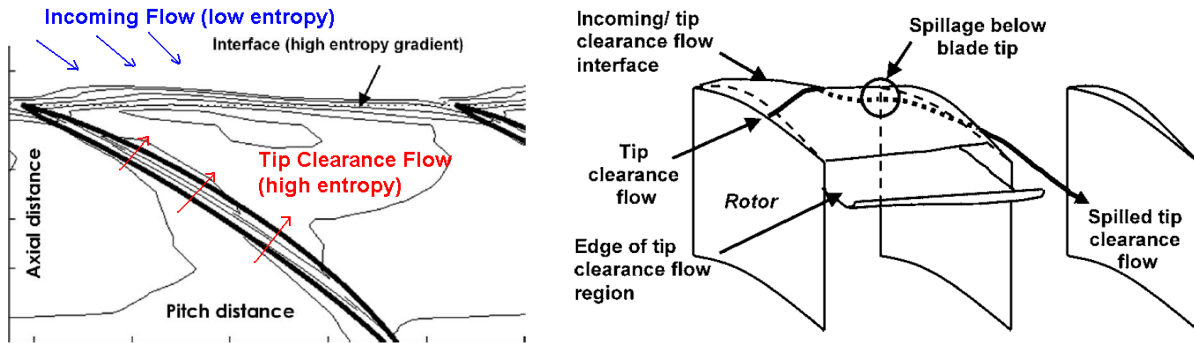
(a) Spike stall inception criterion 1
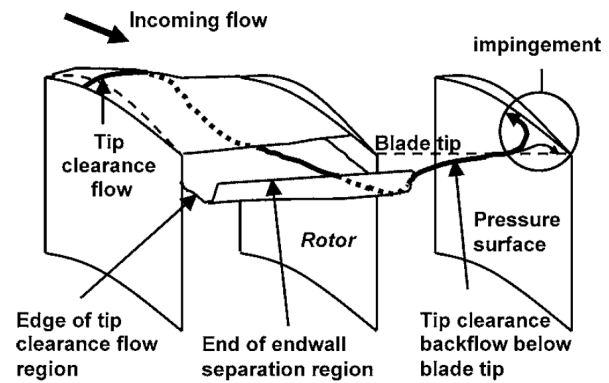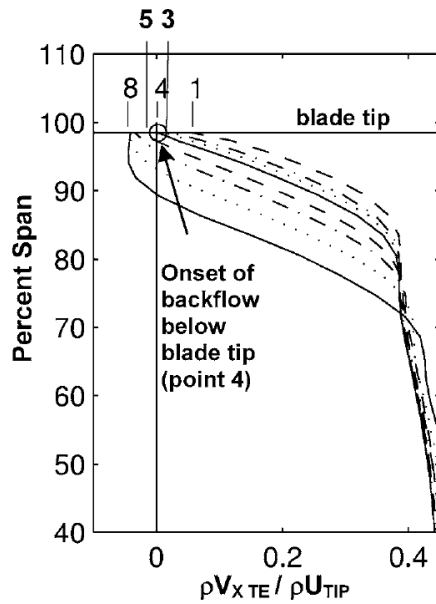
(b) Spike stall inception criterion 2

Figure 1.4: Rotating stall via spikes inception proposed by Vo *et al.* (2008)

ahead of the blade into the adjacent passage as illustrated on the right part of Figure 1.4(a). The second proposed spike stall inception criterion is the axially reversed flow of tip clearance fluid at the trailing edge and its impingement on the adjacent blade's pressure surface, as depicted on the right side of Figure 1.4(b). This criterion is indicated by the spanwise distribution of mass flow at the trailing edge plane, where the mass flow at the blade tip is reaching zero, as shown by the left plot of Figure 1.4(b). Vo *et al.* (2008) stated that both criteria must be satisfied for spike stall inception to occur. Although the generic nature of the backflow criterion is still under debate, the leading edge interface seems to be a common feature in rotating-stall via spikes (Hah *et al.*, 1999; Marz *et al.*, 2002; Deppe *et al.*, 2005).

Hah *et al.* (2006) carried out a similar numerical study for spike stall inception in a transonic compressor. Despite additional complications brought about by the tip clearance flow interaction with shocks, their simulations seemed to support the criteria proposed by Vo *et al.* (2008), as shown by tip clearance flow streamlines near and at stall in Figure 1.5.
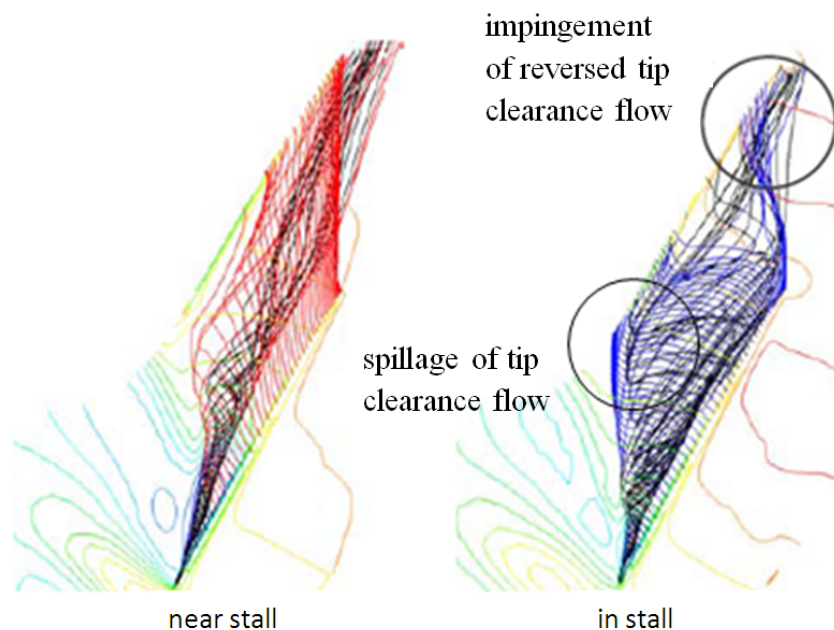
Figure 1.5: Tip clearance flow streamlines near and at rotating stall via spikes inception in high speed compressors (Hah *et al.*, 2006)

1.2 Blade Design Methodologies

Most of the literature on compressor design focuses on performance or stability improvement. A review of this research is carried out with particular attention given to decreasing losses associated with tip leakage flow at high subsonic and transonic Mach numbers. This work usually involved two blade design features: changing the camber-line and stacking line.

Before proceeding with the literature review into blade design, a brief introduction to blade design nomenclature is presented with the aid of figures 1.6 and 1.7. As shown in Figure 1.6(a), the chord is defined as the distance between the leading and trailing edges of the blade, the camber line is the mean line between the blade's upper and lower surfaces, and the distance between the chord and the camber line is the camber. Figure 1.6(b) illustrates the stacking line, which is the imaginary spanwise line connecting the two-dimensional blade profiles at their aerodynamic centre or the loading center where the pitching moment coefficient does not vary with angle of attack. This is generally assumed to be located at mid-chord for uniformly loaded blades. The stacking line can be bent axially, referred to as blade sweep, or circumferentially, known as blade lean, as shown in Figure 1.7.

(a) Schematic of camber

(b) Schematic of stacking-line
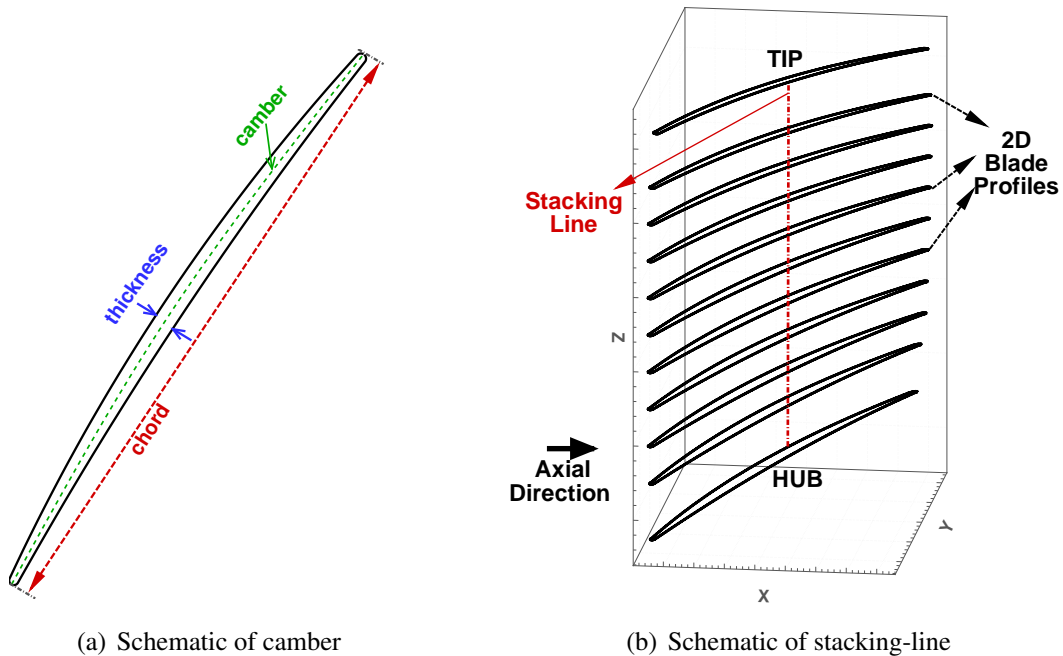
Figure 1.6: Schematics of camber and stacking line in a compressor blade

(a) Schematic of sweep in meridional plane (b) Schematic of lean in axial plane
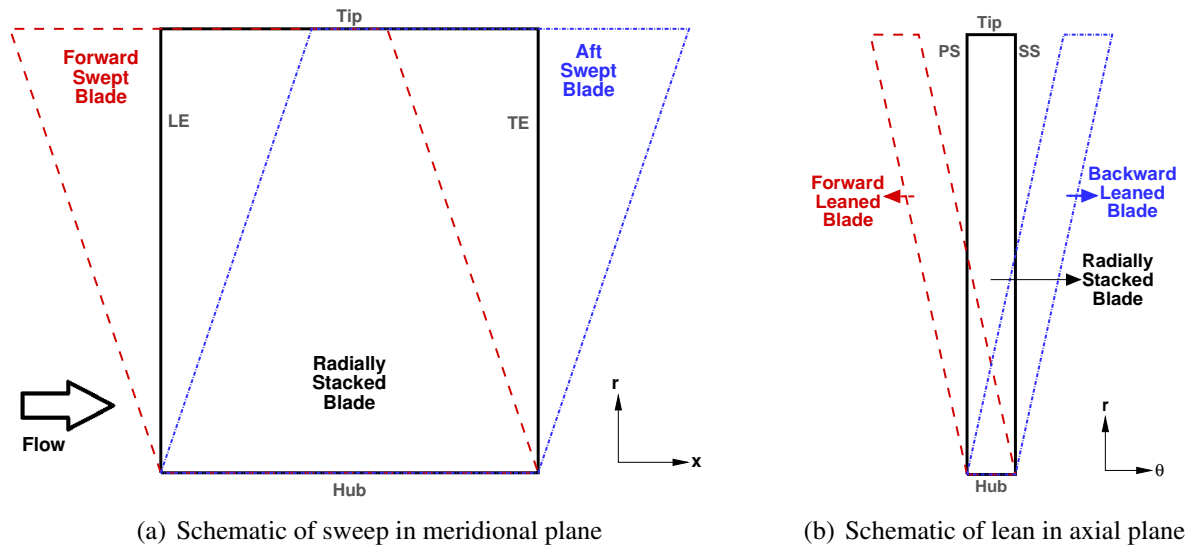
Figure 1.7: Schematic of sweep and lean in compressor blades

1.2.1 Camber-line Change

The camber-line shape has a direct influence on chordwise blade loading distribution. Simply, an aft-loaded blade is achieved by increasing the aft camber and decreasing the front camber, as shown in Figure 1.8.
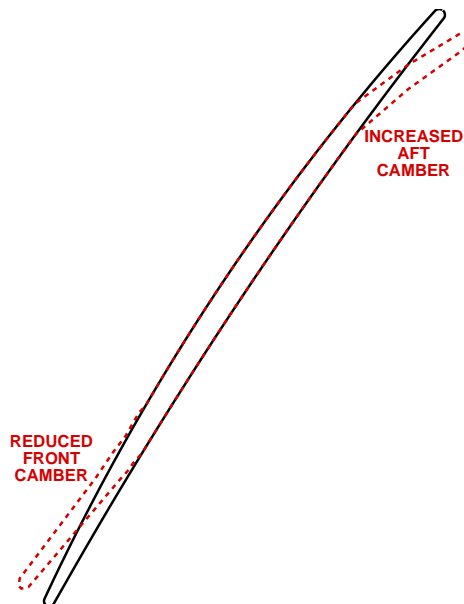
Figure 1.8: Creation of aft-loaded blade by modifying front and aft cambers

In subsonic flow regimes, front-loaded blades are used to reduce profile losses, and other types of blades (uniform-loaded and aft-loaded blades) are used for reducing secondary flow losses, such as boundary layer separation, corner separation, tip clearance flow, etc. However, in transonic flow regimes, aft-loaded blades are more common due to shock losses. Since a front-loaded blade would have a strong shock near the leading edge and perhaps even a second shock downstream if velocity increases enough. On the other hand, an aft-loaded blade delays the formation of the first shock to a downstream location, which decreases the possibility of second shock. Moreover, a downstream shock is weaker, since the compressor blade passage has partially diffused the flow and the velocity is thus lower upstream of this shock. Therefore, aft-loading decreases the shock related losses in transonic flows. Typical transonic and subsonic blade profiles are illustrated in Figure 1.9.

(a) An aft-loaded transonic blade: NASA Rotor 37   (b) A front-loaded low subsonic blade: NACA 65012
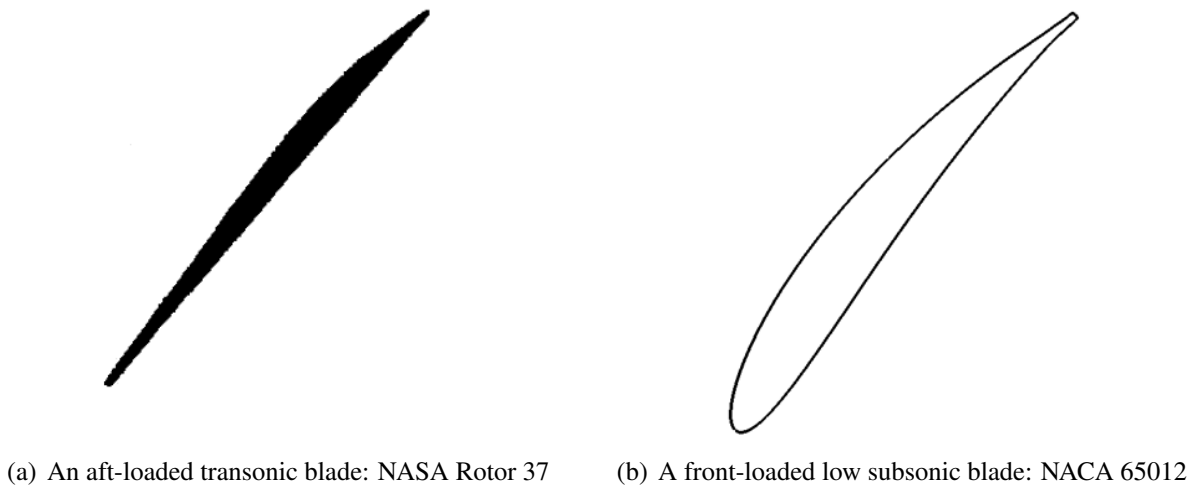
Figure 1.9: Typical blade profiles and their common application

The study of Gallimore *et al.* (2002a) is an example showing the effects of aft-loaded blades on both low-speed and high-speed axial compressors. They modified the blade profiles for higher efficiency by changing the camber at the blade tip to transfer high loading from the front to aft. The authors found that aft loading increased the efficiency in the tip region and attributed this increase to the reduction in the tip leakage losses. However, they did not provide any physical explanation.

Bonaiuti *et al.* (2007) found that aft-loading a transonic compressor blade increases the flow range and total pressure rise. However, excessive aft-loading and its associated high flow turning leads to suction side boundary layer separation and reduced peak efficiency. Thus, the authors optimized the amount of aft-loading on the blade for maximum efficiency while keeping the pressure ratio constant. The efficiency of the resulting blade increased by 1.3% when compared to the uniformly loaded baseline blade. In addition, they demonstrated that aft-loading the blade reduced the shock strength and changed the shock shape and position at the blade tip.

Shao *et al.* (2007) studied the effects of various design methods on tip losses on a transonic compressor rotor. They found that aft-loading created the least tip loss when compared to mid-loading and front-loading. They observed that having higher loading in the front region creates higher local tip loss, although they did not explain their findings.

1.2.2 Stacking-line Change

The stacking-line shape is known to influence both spanwise and chordwise loading, since a change in stacking line alters the spanwise pressure distribution, the low-energy secondary flows and the tip clearance flows. Studies on each type of stacking-line change such as blade sweep, blade lean and their combinations are reviewed next.

Blade Sweep

Denton and Xu (1998) studied the 3D flow effects of blade sweep analytically. They proposed that aft-sweeping the blade shifts the loading toward the leading edge. The reasoning is illustrated in Figure 1.10 for an aft swept blade. The pressure gradient normal to each endwall (*dP/dn*) should be zero since no flow would accelerate through the wall. Thus, near the blade tip the pressure gradient normal to the shroud should be low. At the blade tip trailing edge the loading would be low, since there is no blade section underneath and at the leading edge the loading would be high since there is loaded blade sections underneath. Thus, for the aft sweep design in Figure 1.10, the blade tip would be front loaded. The authors stated that in subsonic rotors, forward-sweeps are used to reduce leading edge load and aft sweeps are used to increase it.
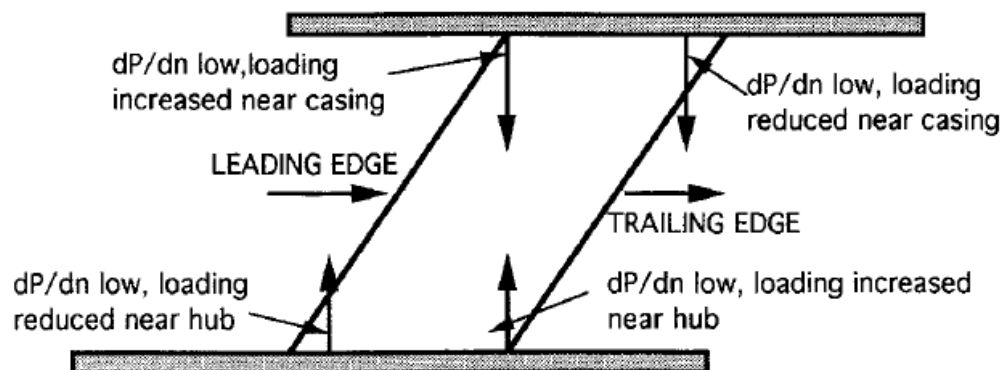
Figure 1.10: Change of loading induced by aft-sweep (meridional view from Denton and Xu (1998))

Passrucker *et al.* (2003) studied the effect of sweep on a transonic rotor analytically and numerically. They pointed out three effects of sweep: blade loading, shock position and accumulation

of low-momentum fluid near the end-wall. The first effect consists of a redistribution of the blade loading. The authors stated that the forward-sweep moved the blade loading aft, confirming the prediction of Denton and Xu (1998) and decreases the losses caused by tip leakage flow. Secondly, shock position near the blade tip was modified by the sweep, since blade tip loading was altered, as shown in Figure 1.11(a). Forward-sweep, which aft-loaded the blade tip, moved the shock at the blade tip to aft and decreased the shock losses. Moreover, the authors claimed that if the shock position were further downstream in the tip region, the stall margin would increase, since they postulated that rotor stall would occur when the shock detaches from the leading edge. The third effect suggested by the authors was that the radially outward migrating boundary layer fluid cannot reach the shroud region due to the forward-sweep of the blade, shown in Figure 1.11(b). Although, they confirmed that forward-sweep caused aft-loading and, thus, downstream shock with computational results, they did not prove detachment of the shock at rotor stall and radial migration of boundary layer fluid.

An experimental study by Bergner *et al.* (2005) showed that at the design point, forward-sweep redistributed the loading and caused the shock to move downstream on the suction side of the blade. However, this work did not support the theory of the Passrucker *et al.* (2003) about the shock position in stall. Their results showed that stall did not occur at the same shock position for different blades. For example the shock, which detaches from the leading edge for forward-swept blade in stall, stays attached to the leading edge for unswept blade.

Goller *et al.* (2005) also studied blade tip tailoring on a low-speed compressor rotor. To increase efficiency, the blade tip was forward-swept by 45°. Forward-sweep reduced the tip blockage for the same tip clearance which led to increases in efficiency and stability margin. This design reduced the tip leakage losses by 3% and increased the stall margin by 5%.

Jang *et al.* (2005) designed an aft-swept transonic rotor blade with tip clearance, and found that aft sweep had no effect on shock position or shape near stall. Nevertheless, they found that aft-sweep increased efficiency by 1.25 percentage points. The authors attributed this increase in efficiency to improvement of flow structure in the region below mid-span. Thus, it can be deduced that although forward-sweep is advantageous in tip region, the aft-sweep is beneficial for the region below mid-span.

In addition to looking at camber change, Bonaiuti *et al.* (2007) also investigated blade sweep numerically. Their observations on forward-sweep supported those of Passrucker *et al.* (2003) in terms of decreased radial migration of low momentum boundary layer fluid, and in terms of reduced shock strength.

Subsequently, Benini and Biollo (2007) investigated effects of sweep on transonic blades numerically to show that an optimized sweep orientation (forward-sweep up-to 70% span and aft-sweep up-to blade tip) increased the efficiency by 0.6 percentage point and operating range by 4%.
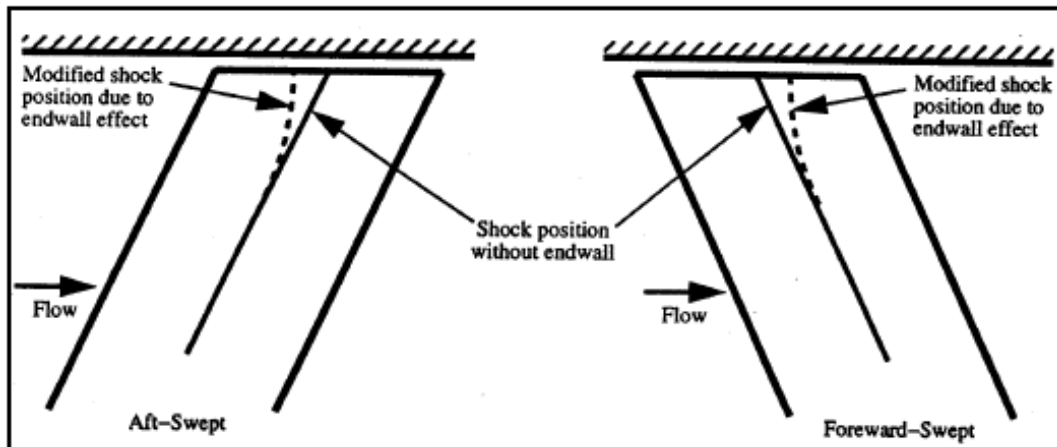
(a) Change in shock location
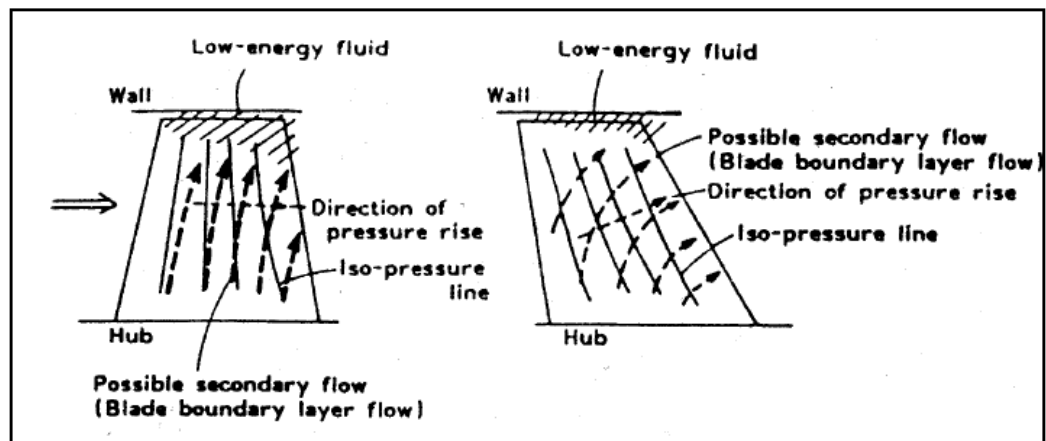
(b) Change in radial migration of boundary layer fluid

Figure 1.11: Effects of forward-sweep (Passrucker *et al.*, 2003)

The combined sweep changed the spatial orientation of shock. However, at the blade tip chordwise shock position is similar to unswept case, such that both the shock strength and the shock shape was similar at peak efficiency and near stall. Thus, the authors concluded that the performance and stability increase induced by sweep was neither related to shock shape nor strength.

Blade Lean

Denton and Xu (1998) also studied 3D flow effects of blade lean analytically. They first hypothesized that a forward-leaned blade is similar to a radially stacked blade, such that it would not have any spanwise variation in meridional velocity (V_m) as shown in Figure 1.12(a). This hypothetical forward-leaned blade would have parallel constant slope isobars suction surface and pressure surface. This would cause a positive normal pressure gradient (dP/dn) at the shroud and a negative normal pressure gradient at the hub, which was infeasible. Then, they concluded that leaning the blade induces a spanwise force (F_r) to equate these pressure gradients to zero, as shown in Figure 1.12(b). This spanwise force causes radial flow curvature in the meridional flow (V_m) to redistribute the spanwise pressure distribution. Radial equilibrium implies that a lower pressure occurs in the tip region and vice versa. This means, that forward-leaned blade will have lower loading at the tip. Since the forward-lean reduces tip loading, the authors noted that it is used to reduce tip losses.

(a) Hypothetical effect on loading (chordwise cut)   (b) Effect on flow, inducing radial force (meridional cut)
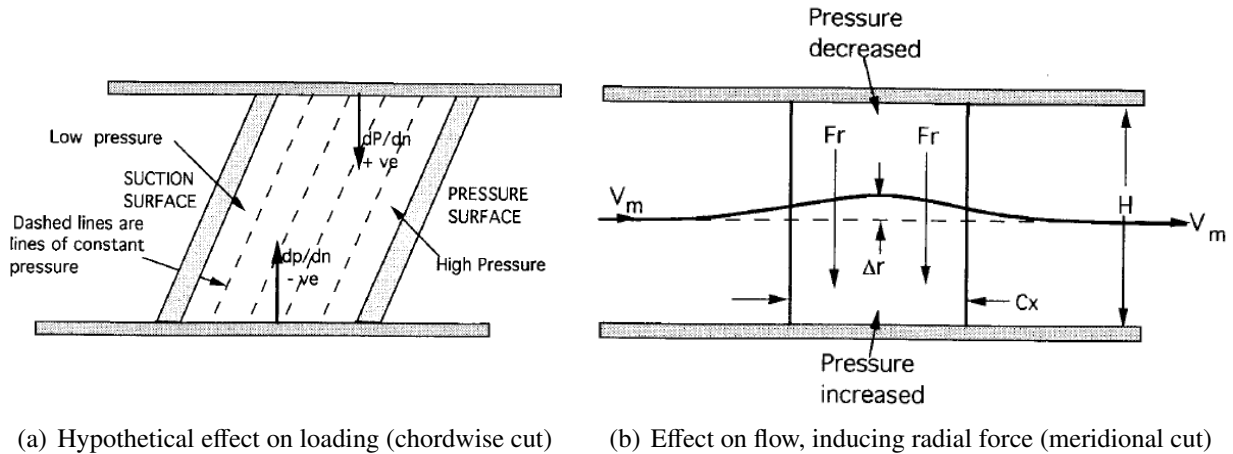
Figure 1.12: Effects of forward-sweep (Cx:Axial Chord, H:Span)(Denton and Xu, 1998)

Ahn and Kimi (2003) performed design optimization with CFD of blade lean on a transonic compressor rotor. It is found that a forward-leaned tip and back leaned mid-span increased the efficiency of the outer span noticeably. The authors attributed this to reduction of shock intensity and change of shock shape and position at the blade tip. The weaker shock decreased the shock losses and increased the efficiency 0.7 percentage point, with a small penalty in static pressure rise.

Instead of a rotor, Jang and Kim (2005) carried out a stator optimization using blade lean in a transonic compressor stage with a stator hub clearance. A stage efficiency increase of 2.5 percentage point was achieved, with a noticeable increase in total pressure, total temperature and static pressure rise. The optimized stacking line (forward-lean in the tip and hub regions) decreased the loading at the hub and the tip. Both near the hub and tip regions, the loading was reduced. Reduced loading in hub region caused lower hub clearance flow and associated losses, whereas reduced loading in the tip region lowered shock angle and shock losses. Therefore, the static pressure rise and efficiency was increased.

In addition to their work on blade sweep, Benini and Biollo (2007) also studied computationally, the effects of blade lean for a transonic compressor rotor. They found that forward-lean increases the efficiency by 1.3 percentage points, without changing the operating range. It also changes the shock shape at the tip near stall, such that the shock became more oblique and its strength is decreased.

Lee *et al*. (2008) worked on increasing efficiency of low-speed axial fan through forward blade lean, achieving an efficiency increase of 1.5 percentage points. Leaning the blade was observed to reduce the loading at the tip. Although it is not mentioned by the authors, decreasing the blade tip loading should decrease the tip clearance flow and the losses associated with tip clearance flow, namely shear/mixing layer loss and tip blockage.

Alternative Methods

Deviation of stacking line in the direction normal and parallel to the chord line, as shown in Figure 1.13, has also been studied. Deviation normal to the chord-line in the direction of the blade suction side (i.e. against rotation) is referred to as positive dihedral. The deviation against the flow direction in chordwise direction is called as positive or forward chordwise sweep. These alternative stacking line changes are basically combinations of the common (axial) blade sweep and (circumferential) blade lean previously discussed.

Vad and Corsini (2002) investigated chordwise sweep experimentally for enhancement of performance and stability. An unswept blade geometry and one with $35°$ forward chordwise sweep were compared. The forward chordwise sweep was found to be beneficial for extending the operational range. The efficiency near peak pressure rise was also increased by 2%. A supporting numerical study was made by Corsini and Rispoli (2004) to analyze the flow structures of forward chordwise sweep. For highly loaded fan blades, the forward chordwise sweep reduced tip loading, hence reducing tip leakage flow. Moreover, tip loading was redistributed by unloading the leading edge. Also, radial migration of low-momentum flows from the region below mid-span were reduced, and the stall point moved to a lower mass flow rate. Aft-loading of the blade tip, decrease in radial migration of low-momentum fluid and increase in stall margin are similar to the effects at-
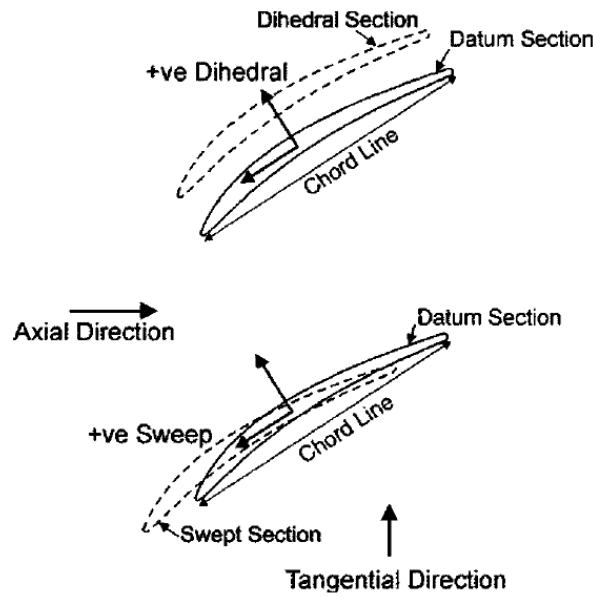
Figure 1.13: Schematic of dihedral and chordwise sweep (Gallimore *et al*., 2002a)

tributed to forward (axial) sweep, while the lower tip loading and lower tip leakage flow are similar to forward (circumferential) lean effects.

Gallimore *et al*. (2002a) also studied numerically the effect of chordwise sweep and dihedral on a low-speed compressor. Forward chordwise swept (20°), aft chordwise swept (-20°), and unswept rotor blades were compared, both with and without tip clearance. The forward chordwise swept geometry was found to increase efficiency and flow range by reducing shock losses for blades without tip clearance. However, tip loss reduction was not found for blades with tip clearance. Also, the aft chordwise swept design was found to have best mid-span efficiency, as suggested earlier for aft (axial) sweep by Jang *et al*. (2005). Gallimore *et al*. (2002a) also mentioned that the beneficial effect of sweep also depended on the sweep angle. Moreover, positive dihedral was found to decrease the tip loading and the authors claimed that this was beneficial as it reduced tip clearance flow and its associated losses. The authors also validated their results experimentally (Gallimore *et al*., 2002b). Although the stall margin and the trends of pressure ratio and efficiency predicted by numerical simulations were found to be correct, the peak efficiency was higher than predicted by numerical simulations.

Finally, Biollo and Benini (2008) combined axial sweep and circumferential lean, and optimized the stacking line for higher efficiency in a transonic compressor rotor. They curved the blade with forward-lean and forward-sweep (which may correspond to forward chordwise sweep, but it is not stated as such by the authors) at the tip and at the hub, and achieved an efficiency increase of 1.2 percentage points and operating range increase of 8%. The authors showed that the optimized

design reduced the tip loading, the tip leakage flow and moved the shock downstream. Moreover, the authors claimed that as a result of these effects, the shock and tip leakage losses were reduced, the efficiency was enhanced and the operational range was extended.

1.3 Desensitization to Hub or Tip Clearance Size

Research on desensitizing the performance and stability to tip clearance is very limited. The literature review on this subject is thus extended to include desensitization both by blading design and by casing treatment.

1.3.1 Desensitization to Hub or Tip Clearance Size by Blading Design

While most researchers are interested in performance or stability increase, a few have looked into the effect of blade design on performance sensitivity to tip clearance. Their work show promising results with respect to the reduction of sensitivity.

The experimental and numerical study of McNulty *et al*. (2004) investigated the effects of forward chordwise sweep on a low-subsonic axial compressor rotor. The study compared a radially stacked blade with a forward chordwise sweep blade, both designed with the same spanwise and chordwise loading distribution at two different configurations (i.e. four designs in total). The first configuration had high tip loading, tip stagger and tip solidity to produce strong tip leakage flows and associated losses, whereas the second configuration had moderate tip loading, tip stagger and tip solidity, which caused moderate tip leakage flows. To keep chordwise loading the same as the unswept blades, the forward swept blades (for both configurations) were also front cambered so as to isolate the effects of sweep on tip leakage flow reduction. Forward chordwise sweep was shown to reduce sensitivity of static pressure coefficient, efficiency and stall margin for both configurations. However, the effect of forward chordwise sweep was more evident in strong tip leakage flow configuration. Moreover, forward-sweep reduced tip total pressure loss due to tip shear/mixing layer loss, tip blockage and double leakage for both configurations. Furthermore, the authors noted that forward chordwise sweep reduced local static pressure coefficient at the tip, which induced higher axial flow near the tip region. Additionally, forward chordwise sweep reduced the reversed flow in tip clearance region, which was attributed to double leakage reduction, without calculating double leakage nor showing the streamlines.

A similar numerical study was performed by Wadia *et al*. (2004) using tip-critical radially stacked and forward chordwise swept rotors in a transonic axial compressor. Although, forward chordwise sweep increased efficiency and stall margin, performance and stability desensitization was not significant. While these results may contradict to those of McNulty *et al*. (2004), the

amount of tip loading of the blades was not stated in this study, thus, they may have used blades with moderate or low tip loading, stagger and solidity, which reduced the favourable effect of chordwise sweep. Moreover, the sweep angle, which was not given in the study, may not have been optimized for significant desensitization effect.

A study on effects of stator hub and rotor tip clearance variation on different blade designs was performed by Tschirner *et al*. (2006). The authors redesigned the stators in a four-stage compressor to desensitize engine performance to stator hub and rotor tip clearance variation between 1.3% and 5% chord. The stator blade stacking line was modified for all four stages at the hub and shroud by 30° circumferential end bends (i.e. circumferential lean), as shown in Figure 1.14. The rotor is kept as a radially stacked blade to isolate effect of the stator design. The new design reduced the stator hub loading by redistributing spanwise load. Reduction in stator hub loading increased the flow range, reduced total pressure loss (shear/mixing loss) in the hub region and the hub blockage. For the overall compressor sensitivity of pressure rise and efficiency to stator hub and rotor tip clearance were reduced in both numerical and experimental studies. Even though both studies showed the same trend, there was a small inconsistency between the numerical and experimental study's efficiency results. The authors attributed in this difference to measurement errors and unsteady effects from adjacent stages.

(a) Initial Design   (b) Modified Design
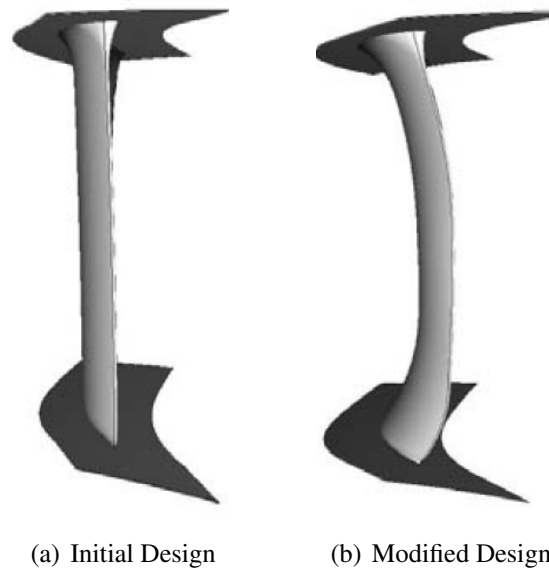
Figure 1.14: The stator design modification proposed by Tschirner *et al*. (2006)

The effects of tip clearance and sweep have been studied extensively by Ramakrishna and Govardhan (2009a,b,c, 2010). Ramakrishna and Govardhan (2009b) analyzed numerically the effect of tip clearance and sweep for a low-speed compressor stage. The pressure rise and stall margin for rotor blades with three angles of forward chordwise sweep (30°, 20° and unswept), were compared

at three tip clearances (0, 0.7% and 2.7% chord). The first observation was that forward chordwise sweep reduced total pressure loading above mid-span and reduced blade boundary layer migration toward the casing, which results in increased stall margin. The second observation was that the increase in stall margin was reduced with tip clearance increase. Moreover, the optimum desensitization was achieved by 20° forward chordwise sweep. For same value of sweep the drop in energy coefficient (static pressure rise coefficient) with increasing tip clearance was reduced when compared to the drops encountered by unswept geometry. In other words, a properly selected forward chordwise sweep angle can reduce the sensitivity of pressure rise to tip clearance.

A recent study by Ramakrishna and Govardhan (2010) redesigned two rotors: one with a 20° forward chordwise sweep and the other with a 20° axial sweep. At optimum efficiency, axially sweeping of the rotor reduced the sensitivity of static pressure difference between pressure and suction surfaces to tip clearance more than chordwise sweep. It was found that axial sweep reduced local incidence at the blade tip, which lowered tip loss and blockage. This was concluded to be the source of desensitization.

1.3.2 Desensitization to Tip Clearance Size by Casing Treatment

Two studies on desensitization of performance and stability to tip clearance through casing treatment were found in the literature. Analyzing desensitization methods by casing treatment may provide clues about the flow mechanism of tip clearance flow and its desensitization.

An extensive experimental study was performed by Takata and Tsukuda (1977) on a low-speed axial-flow compressor, in which effects of many casing treatments are analyzed for stability increase at different tip clearances. Figure 1.15 shows the most effective casing treatments used by Takata and Tsukuda (1977): axial-radial skewed slots, axial slots and circumferential grooves. They showed that all these three casing treatments increased stall margin and reduced sensitivity of stall margin, with the axial-radial skewed slots being the best of the three.

The authors associated the effectiveness of axial-radial skewed slots in improving stall margin and desensitizing stall margin to four factors. The first is that stall margin improvement and desensitization were not attained by angle of attack reduction near the blade tip, such that blade incidence angle near the stall of axial-radial skewed slots was higher than that of other treatments. Since stall margin of axial-radial skewed slots is higher than other treatments, it is normal to have higher incidence near stall conditions. The second factor was that the axial-radial skewed slots redistributed the axial momentum at the outlet plane, such that the upper span has higher axial velocity, although radial distribution of inlet axial velocities was not changed. In other words, tip blockage lowered and that may be one of the causes in the reduction sensitivity of stall margin to tip clearance. The third factor was that the axial-radial skewed slots reduced the tip loss such that the upper span rela-

(a) Axial-Radial Skewed Slots   (b) Axial Slots   (c) Circumferential-Grooves
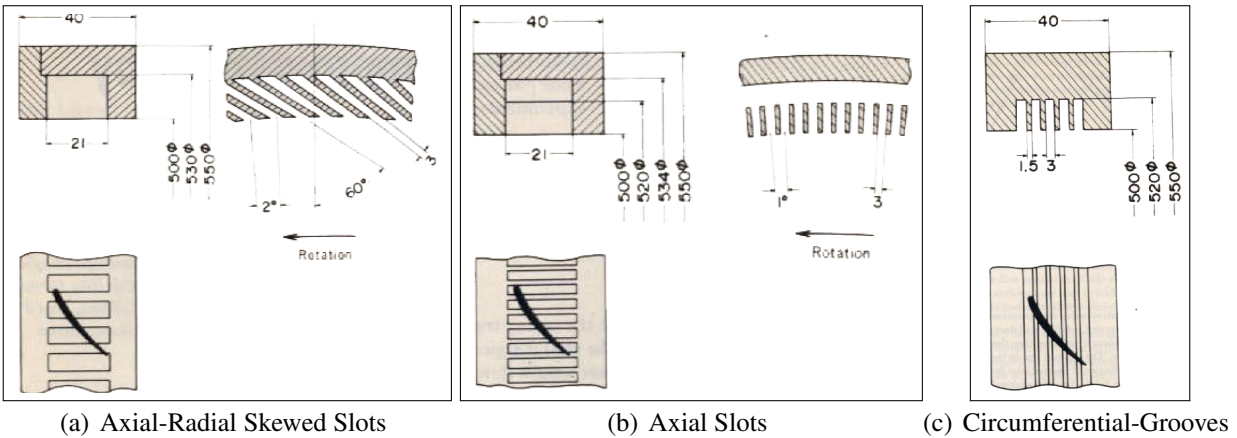
Figure 1.15: The most effective casing treatments used by Takata and Tsukuda (1977)

tive total pressure loss was almost equal to mid-span loss for operation past the optimum efficiency point and near stall. The last factor was that the axial-radial skewed slots redistributed the relative tangential momentum at the outlet plane, such that the upper span had higher relative tangential velocity.

A numerical study of Beheshti *et al*. (2004) on transonic axial compressor explored the effect of circumferential grooves on performance and stability with different tip clearances. The authors showed that the circumferential grooves increased stall margin and efficiency at higher tip clearances, such that the sensitivity of stall margin and efficiency was reduced considerably. This effect was attributed to the fact that circumferential grooves decreased loading at the tip, and the interaction of passage flow and tip clearance flow. Consequently, the tip shear/mixing layer loss was reduced. Moreover, it was stated that the axial flow at the blade tip region was increased by introducing circumferential grooves, because the suction of tip leakage flow by the grooves left more axial flow at the aft-part of tip region thus reducing the tip blockage. However, it was found that the circumferential grooves slightly degraded total pressure ratio.

1.4   Summary

From the literature review, the elements that can be used in this research are:

- The effects of tip clearance flow can be summarized based on three important parameters: tip loss, tip blockage and the interface between the incoming and tip clearance flows, where the former two are related to the performance, and the latter to stability.
- In terms of designing blade for lowering losses associated with tip clearance flow; aft-loading, forward-sweep and forward-lean and their combinations were found to reduce tip shocks, tip losses and tip blockage. Aft-loading by camber reduced shock losses and there-

fore, increased efficiency. Forward-sweep had an aft-loading effect and reduced secondary flow losses, which resulted in increased efficiency and stall margin. Forward-lean, on the other hand, reduced tip loading and thus, tip clearance flow-related losses, and also shock losses, which resulted in an increase in efficiency.

- In terms of designing blade for desensitization, forward-chordwise-sweep in the rotor design seemed to be effective in reducing sensitivity of pressure rise, efficiency and stall margin to tip clearance. Reducing tip blockage, local blade incidence and double leakage, increasing local axial and circumferential flows at the tip may be linked to desensitization.

Based on the literature review two hypotheses can be made about the most sensitive parameter associated with tip clearance flow and the desensitizing flow features.

1.4.1   Hypothesis on Most Sensitive Tip Clearance Flow Parameter

From tip clearance flow physics, the effects of tip clearance flow can be divided into three parameters: tip loss, tip blockage and the interface between incoming and tip clearance flows. A hypothesis with respect to the most sensitive parameter to tip clearance can be made.

- The position of incoming/tip clearance flow interface is set by momentum balance between these two flows. The tip clearance flow distribution along the chord is set by blade loading distribution and tip clearance. As the tip clearance increases, both incoming flow and tip clearance flow will increase. Thus, it can be assumed that the interface position is actually set by the blade loading distribution.
- Shear/mixing layer loss is affected by difference in tip clearance flow and incoming flow vectors. Thus, it is dependent on blade loading.
- Tip blockage, on the other hand, depends on tip clearance flow and pressure rise through the blade passage.

If one can infer that blade loading is relatively insensitive to tip clearance for small to moderate tip clearances, so too, are the shear/mixing layer loss and the interface position, which leaves tip blockage as the most sensitive parameter to tip clearance.

1.4.2   Corollaries on Desensitizing Flow Features

If the tip blockage is the most sensitive parameter to tip clearance, one can hypothesize that any method that can reduce the contribution of tip blockage to performance will help desensitize performance to tip clearance. Therefore, two corollaries can be made. First one is *shifting the tip clearance flow distribution toward the trailing edge* would reduce the tip blockage, hence the sensitivity to tip clearance. Second is *changing the flow path into tip clearance* would reduce the tip blockage, hence the sensitivity to tip clearance..

The first corollary, based on the work by Khalid *et al.* (1999), will minimize the generation and growth of blockage from tip clearance size flow by controlling the chordwise tip clearance flow distribution and minimizing the pressure rise that the tip clearance fluid undergoes to reach the blade-passage trailing edge plane. Figure 1.16 shows schematically the effect of first method, whereby the zone of maximum tip clearance (largest "wake" in Khalid *et al.* (1999)'s model) is shifted to the rear passage by shifting loading aft. This also minimizes the distance traveled (and hopefully the pressure rise experienced) by this flow to the trailing edge plane, thus reducing tip blockage. The literature review showed that shifting the loading aft can be achieved by moving the location of maximum camber aft or by sweeping and/or leaning the blade forward.
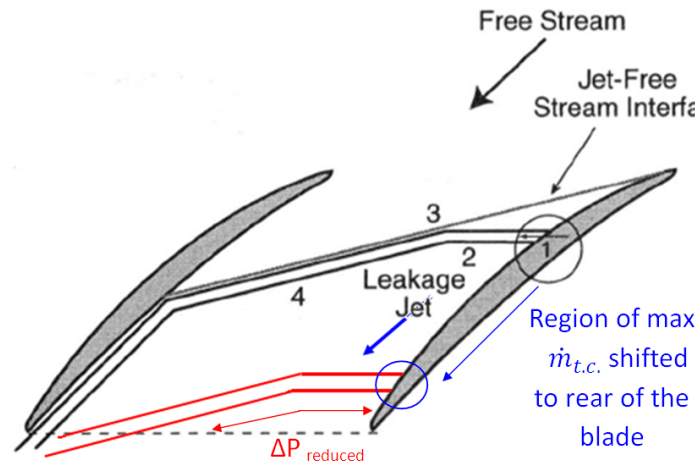
Figure 1.16: Effect proposed by changing the tip loading distribution (modified from Khalid *et al.* (1999))

The second corollary, on the other hand, aims to decrease the tip leakage flow by obstructing the tip leakage flow path. Figure 1.17 shows schematically the effect of second method on the tip leakage flow, whereby the blade tip is leaned forward, to obstruct the tip clearance fluid flow path.
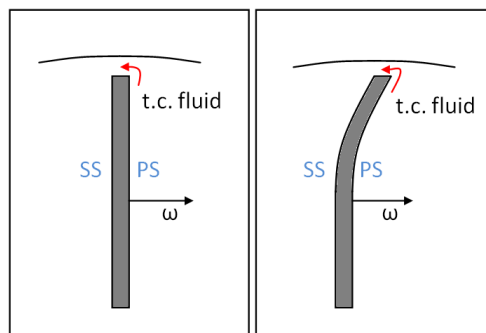
Figure 1.17: Effect proposed by changing the tip clearance flow path

Chapter 2

Methodology

A computational approach is chosen for this research to allow practical and detailed study of different design parameters on desensitization of performance and stability to tip clearance. As such, the methodology can be divided into four phases. The first consists of the computational tool setup. Phase 2 involves an assessment of the performance and stability sensitivity to tip clearance for a multitude of rotor designs from a design parametric study. From this database Phase 3 identifies and validates desensitizing flow features. Lastly, the blade design characteristics exploiting these desensitizing flow features are proposed in Phase 4.

2.1 Phase 1: Computational Tool Setup

In Phase 1, the computational tool is selected, a mesh quality study is carried and the computational setup is validated with simulations of a well-established reference blade geometry. The computational tool should capture boundary layer flow and its separation, integral flow variables such as pressure ratio and efficiency accurately.

2.1.1 Computational Tool and Mesh Selection

The computational tool chosen for this research is ANSYS CFX version 13. It was a commercial Reynolds-Averaged-Navier-Stokes (RANS) Computational Fluid Dynamics (CFD) code commonly used for turbomachinery and recommended by Pratt & Whitney Canada (PWC). Although superior computational techniques such as Large Eddy Simulation (LES), Direct Numerical Simulation (DNS) exist, they required more computational time and resources than was practically available for the current research.

ANSYS CFX 13 had a node-centered, pressure-based, implicit flow solver, which could handle both structured and unstructured grids. Among the common turbulence models available in CFX were the two-equation models such as $k - \omega$, $k - \epsilon$ and Shear Stress Transport (SST). SST was the superior model to $k - \epsilon$ and $k - \omega$, since it combines the benefits of both models. Near a wall boundary $k - \omega$ was used as it provided more accurate results compared to $k - \epsilon$. Away from wall boundaries, the SST turbulence model calls upon the $k - \epsilon$ model which was faster and more accurate in this region. In between these layers, the SST turbulence model used a special

function to assure continuity. ANSYS (2006) recommended the $k - \epsilon$ turbulence model for more robust solutions and SST turbulence model for more accurate solutions. Moreover, Liu *et al*. (2008) showed that in axial compressor rotors, tip vortices are predicted best by the SST model. Thus, the SST model was selected as the turbulence model.

Boundary Conditions and Other Properties of Simulation Setup

Figure 2.1 shows boundary conditions used for the computational domain in all simulations. A single rotor blade passage was solved in the rotating frame of reference with a periodic condition applied to the circumferential boundaries of the computational domain, as illustrated in Figure 2.1(a). The inlet and outlet axial planes are taken at least one blade pitch away from the blade leading and trailing edges, respectively. This distance will ensure that the amplitude of any perturbation with a circumferential wavelength at or below one-pitch, attenuates in the blade passage to zero at the inlet/exit boundaries to respect the circumferential pressure uniformity conditions at these boundaries. Figure 2.1(b) shows that a viscous wall boundary condition (i.e. no-slip condition) was applied at all solid surfaces with the shroud taken as a counter-rotating wall in the frame of reference of the rotor.

(a) Spanwise cut (b) Meridional cut
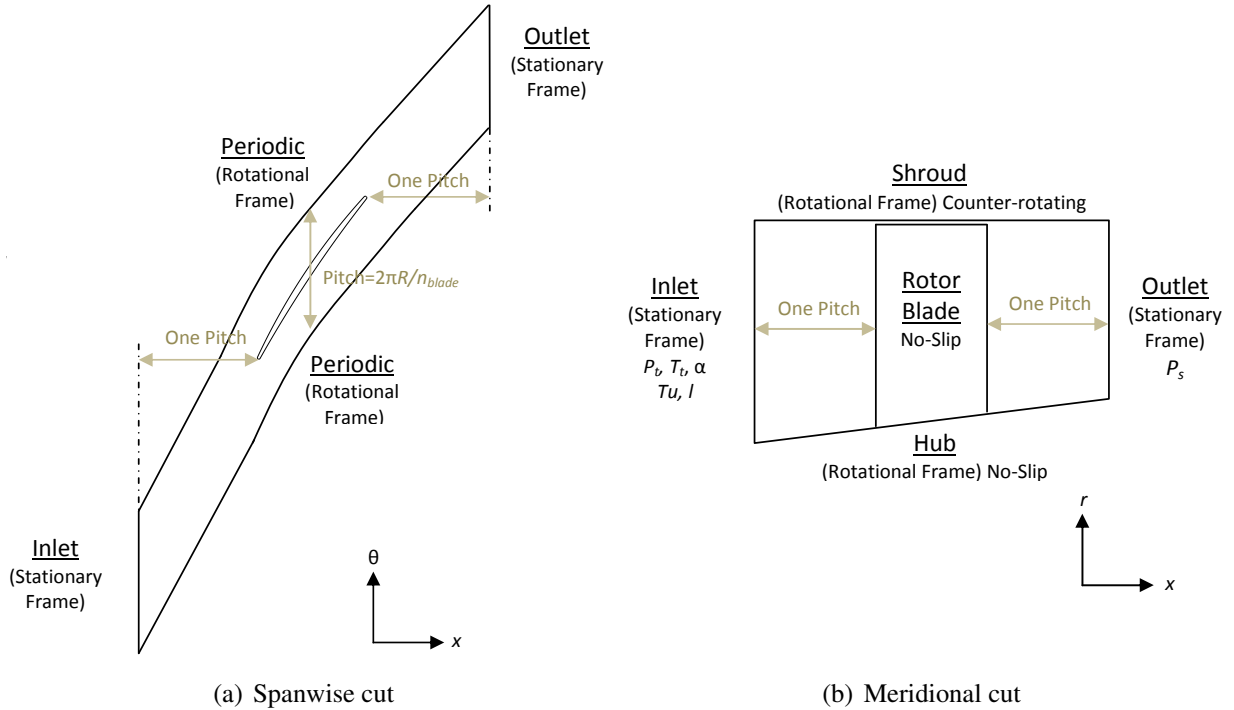
Figure 2.1: The initial conditions defined at the boundaries

At the inlet of the computational domain (which is defined in the stationary frame), spanwise distributions of stagnation pressure (P_t), stagnation temperature (T_t) and flow swirl angle (α) are assigned and an average static pressure (P_s) value was specified at the domain exit, as shown in Figure 2.1(b). The inlet turbulence was set at medium intensity (Tu=5%) with a local length (l=0.5 span). The outlet static pressure (back-pressure) was varied to achieve the designed mass flow.

Air was taken as an ideal gas since high-speed flows are simulated. The flow was assumed to be fully turbulent, such as a boundary layer transition model was not used, since the Reynolds number based on axial chord was between 5×10^5 and 7×10^5 and the compressor blade passage had a generally positive pressure gradient. Additionally, for solving high-speed flows, temperature change should be calculated accurately. Therefore, the total energy equation was solved including the viscous work term.

Mesh Selection

Structured grids were used to mesh the computational blade domain in this research. The grid was generated by ANSYS CFX 13 Turbogrid. A mesh convergence study was conducted to select the adequate mesh density in the streamwise and spanwise directions. The pitchwise mesh density was kept proportional to streamwise mesh density at all times: In the streamwise direction 48, 66, 82, 98 nodes are first assessed with 100 spanwise nodes. The corresponding total number of nodes were 3×10^5, 4×10^5, 5×10^5 and 7.5×10^5, respectively. The mesh density was selected according to achieve similar pressure ratio and efficiency with the highest mesh density. Next, the selected streamwise mesh size was experimented with 50, 75, 100, 150 nodes in the spanwise direction.

All grids had high mesh density at the leading and trailing edge regions. Knowing the Reynolds number range was between 5×10^5 and 7×10^5, the starting length (y^+) was set around 1, the common approach for a no-slip boundary condition. ANSYS (2006) recommended 10 nodes in the boundary layer for accurate results with the SST turbulence model. Thus, to be safe, 15 nodes were put in the blade boundary layers without violating the maximum recommended grid stretching ratio of 1.2. The spanwise mesh quality was chosen in accordance with Van Zante *et al*. (2000), who provided widely accepted recommendations in terms of mesh quality for solving compressor tip clearance flow accurately. These recommendations were:

- 75 spanwise cells in the spanwise direction;
- 12 spanwise cells in the tip clearance for a tip clearance of 1.3% tip chord; and,
- In the tip clearance, the mesh size expands from $y^+ \approx 1$ at the shroud to higher y^+ at the blade tip without violating grid stretching rules. Therefore, the tip clearance is meshed with non-uniformly spaced spanwise cells.

It is noted that at the blade tip y^+ value is greater than 1, which may exceed the viscous sub-

layer, which was limited by y^+ value of 5. However, ANSYS (2006) explained that SST turbulence model switches between no-slip condition to wall-function automatically, if y^+ value is greater than 5. As long as 10 nodes existed in the boundary layer, where 15 is used, the SST model could solve the flow near the wall accurately with higher y^+ values.

2.1.2 Computational Tool Validation

As a standard high-speed compressor geometry, NASA Rotor 37 was chosen for validation purpose. The design characteristics of NASA Rotor 37 are presented in Table 2.1 and its geometry is shown at Figure 2.2. NASA rotor 37 is a transonic compressor blade designed by Reid and Moore (1978) which has been tested by many researchers and has often been used as a validation case. Thus, extensive experimental measurements and numerical results are available for this geometry.

Table 2.1: Properties of Rotor 37 (Reid and Moore, 1978)

Property	Value
Number of Blades	36
Nominal Tip Clearance	0.356 mm
Rotational Speed	17188.7 rpm
Tip Speed	454.14 m/s
Tip Mach Number	1.48
Span at Leading Edge	0.0749 m
Aspect Ratio	1.19
Design Mass Flow Rate	20.19 kg/s
Design Pressure Ratio	2.1
Design Efficiency	87%

(a) Meridional View of Blade (Denton, 1997)   (b) Blade Profile
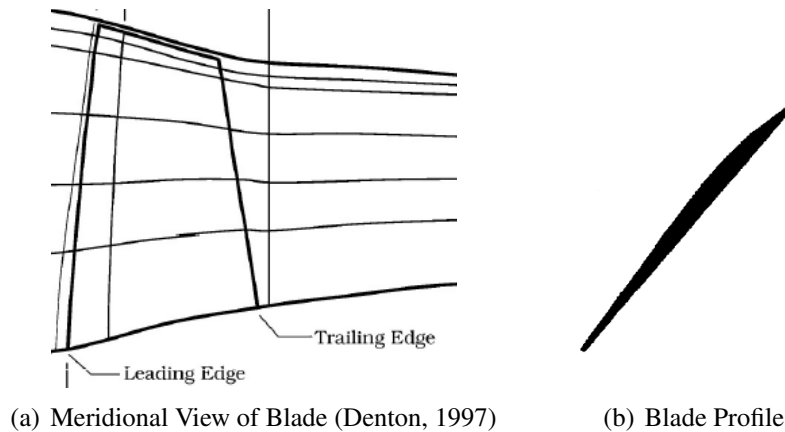
Figure 2.2: Geometry of Rotor 37

Among the published work on Rotor 37, the experimental studies of Suder *et al.* (1995) and Suder and Celestina (1996) characterize the behaviour of the flow in the tip region at the design point. Moreover, the numerical studies by Arima *et al.* (1999) and Hah (2009) show the extend of current computational technology to simulate the flow field. Arima *et al.* (1999) used RANS with $k - \epsilon$ turbulence closure, whereas Hah (2009) uses Large Eddy Simulation (LES) to solve the flow field. Both of the authors successfully validated their codes with available experimental data and estimated the performance characteristics with less than 0.5% error.

In the present validation process, the blade passage flow field at the 70% and 95% span, and the calculated total pressure ratio at the design point are compared to the data from the above experimental (Suder *et al.*, 1995; Suder and Celestina, 1996) and numerical studies (Arima *et al.*, 1999; Hah, 2009).

2.2   Phase 2: Sensitivity Study

The sensitivity study with respect to tip clearance size is carried out on two levels: The first, or general level, involves integral parameters such as pressure ratio, efficiency and stall margin, for an assessment of the effect of tip clearance on performance and stability. The second, or detailed level, involves the sources of loss and stability to identify the element(s) that is (are) most sensitive to tip clearance.

The sensitivity study is carried out in three steps: a preliminary sensitivity study with a PWC axial rotor, an assessment of sensitivity variation with blade design features and the provision of a database for identification of desensitizing flow features. These steps allow most sensitive flow parameter(s) to tip clearance, beneficial design and flow features for desensitization of performance and stability.

It is noted here that tip clearance increase was performed by shroud expansion, as recommended by PWC, rather than span reduction.

2.2.1   Sensitivity Study Parameters

The main parameters of the sensitivity study were defined before starting the study. These parameters were calculated by ANSYS CFX Post and Matlab using the flow field variables of the ANSYS CFX Solver.

The integral performance parameters assessed in the general sensitivity study were total-to-total pressure ratio and total-to-total efficiency. The calculations were carried out at planes located at the computational domain inlet (Plane 1), 10% chord upstream of the leading edge (Plane 2), 10% chord downstream of the trailing edge (Plane 3) and at the computational domain outlet (Plane

4). The stagnation properties were mass-averaged and the static properties are area-averaged. The general stability parameter was the stall margin.

The formulations of general performance and stability parameters are listed below:

- Corrected mass flow ($\dot{m}_c$) was defined as shown in Equation 2.1.

$$\dot{m}_c = \frac{\dot{m}\sqrt{T_{t,2}/T_{ref}}}{P_{t,2}/P_{ref}} \tag{2.1}$$

   where $T_{t,2}$ and $P_{t,2}$ are total temperature and pressure, respectively, in the stationary frame at Plane 2, while T_{ref} and P_{ref} are reference temperature (288.15 K) and pressure(101.325 kPa), respectively, for the International Standard Atmosphere at the sea level.

- The total-to-total pressure ratio (PR_{tt}) is defined as shown in Equation 2.2.

$$PR_{tt} = \frac{P_{t,3}}{P_{t,2}} \tag{2.2}$$

   where $P_{t,3}$ and $P_{t,2}$ are total pressures in the stationary frame at Plane 2 and Plane 3, respectively.

- The total-to-total efficiency (η_{tt}) is defined with the assumption of air as an ideal gas with constant specific heats as shown in Equation 2.3.

$$\eta_{tt} = \frac{(P_{t,3}/P_{t,2})^{\frac{\gamma}{\gamma-1}} - 1}{(T_{t,3}/T_{t,2}) - 1} \tag{2.3}$$

   where $T_{t,3}$ and $T_{t,2}$ are total temperatures in the stationary frame at Plane 2 and Plane 3, respectively, and γ is the specific heat ratio for air, taken as 1.4.

- The stall margin ($S.M.$) is defined here as the difference in corrected mass flow rate between the stall point ($\dot{m}_{c,stall}$) and the design point ($\dot{m}_{c,design}$) (i.e. corrected mass flow rate at maximum efficiency) non-dimensionalized by the latter, as shown in Equation 2.4.

$$SM = \frac{\dot{m}_{c,stall} - \dot{m}_{c,design}}{\dot{m}_{c,design}} \tag{2.4}$$

The detailed sensitivity study assesses the sources of performance loss associated to tip clearance flow, namely tip blockage and shear/mixing layer loss, and the most widely agreed upon criterion for spike rotating stall inception: the interface between the incoming and tip clearance flows lying at the rotor tip leading edge plane. Therefore, the tip blockage, the tip loss and the

position of the incoming/tip clearance flow interface with respect to the rotor tip leading edge plane are computed and plotted versus tip clearance.

The formulations of detailed performance and stability parameters are listed below:

- Tip blockage was defined by the 3-D streamwise velocity deficit at the rotor trailing edge plane caused by tip clearance flow and was quantitatively obtained with the formulation proposed by Khalid *et al.* (1999). The delimitation of the blockage region associated with tip clearance flow was carried out using spanwise entropy gradients and velocity gradients. The details are explained in Appendix A.1. The blockage formulation is given in Equation 2.5:

$$A_b \quad = \quad \iint_{A_{tip}} \left(1 - \frac{\rho V_{str}}{\rho_e V_e} \right) dA \tag{2.5}$$

where A_b is the blockage area, ρ and u_{str} are the local density and streamwise velocity component, and ρ_e and u_e are the density and streamwise velocity component at the edge, in other words the nearest point of the core flow region. A_b was plotted after being non-dimensionalized by the edge area (A_e).

- Tip loss was defined by the rate of entropy generation associated with mixing of the incoming/core and tip clearance flows. The rate of entropy generation formulation is based on Iandoli and Sciubba (2010), where the loss is defined as addition of viscous losses and heat losses. The viscous and heat losses were defined by velocity and temperature gradients which were easily calculated with CFD. Volume-integrating these gradients in the tip blockage region gave the tip loss. The details are explained in Appendix A.2. The tip loss formulation is given in Equation 2.6:

$$\dot{S}_{gen} \quad = \quad \iiint_{Volume_{tip-block}} \left(\mu \frac{\Phi}{T} + k \frac{\nabla^2 T}{T^2} \right) dV \tag{2.6}$$

where $\dot{S}_{gen}$ stands for the entropy generation rate, μ is the dynamic viscosity, T is local temperature, k is the thermal conductivity of air, and Φ is the dissipation rate, which is a function of velocity gradients. $\dot{S}_{gen}$ was plotted after being non-dimensionalized by the ratio of rotor power and total temperature at inlet ($\dot{W}_{rotor} / T_{t,1}$).

- The incoming/tip clearance flow interface was located at the highest entropy gradient line at the rotor tip plane. The position of interface was defined by the intersection of this highest entropy gradient line and the 85% pitch line from the suction surface of the blade tip. The 85% pitch was selected to be as close to pressure side as possible and without being affected

by pressure side boundary layer entropy gradient. Figure 2.3 illustrates the interface location for an axial rotor. Interface position (x_{int}) was measured from the leading edge plane, since stall criterion would be satisfied when incoming/tip clearance flow interface reaches the leading edge plane. x_{int} was plotted after being non-dimensionalized by the axial chord (c_x). Since having interface position at leading edge means the blade is stalled, the interface position can also substitute for stall margin in cases where the speedline is not simulated all the way to the stall point.
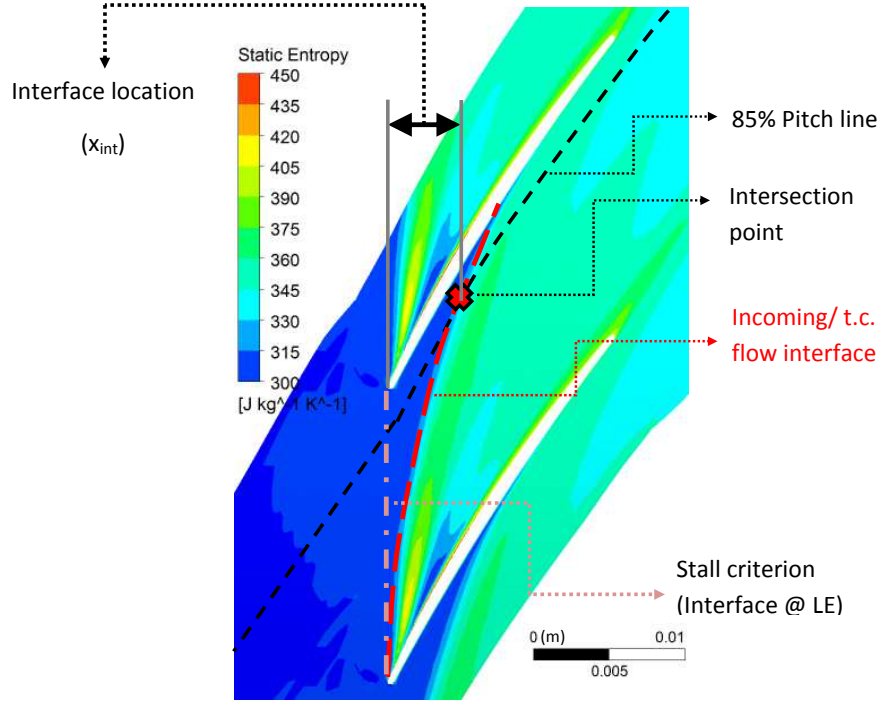
Figure 2.3: Definition of interface position

2.2.2 Preliminary Sensitivity Study

The objective of the preliminary sensitivity study was to assess the most sensitive flow parameter(s) in order to deduce design strategies. This study will prove or refute the first hypothesis that tip blockage is the most sensitive parameter of tip clearance flow (Section 1.4.1).

A reference high-pressure transonic compressor rotor was chosen for study. The selected reference geometry for the baseline sensitivity study was a PWC compressor rotor with transonic tip speed whose main design features are shown in Table 2.2.

The main tip clearances used were 0.4% , 0.9% and 1.8% chord (c). The speedlines for each tip clearance simulated design rotational speed through an increase in the exit static pressure from

Table 2.2: Characteristics of PWC Rotor (Provided by PWC)

Property	Value
Number of Blades	45
Nominal Tip Clearance	0.4% chord
Rotational Speed	24286 rpm
Tip Mach Number	0.9
Design Corrected Mass Flow Rate	3.49 kg/s

near-choke toward near-stall values. It was essential to ensure that there were points with the same corrected mass flows across the different speedlines. After finishing the speedlines, the sensitivity study consisted of plotting the relevant parameters versus tip clearance for the same corrected mass flow near choke, at design (at optimum efficiency) and near stall. The most sensitive parameter(s) was/were extracted to prove or refute the first hypothesis presented in Section 1.4.1.

2.2.3 Assessment of Sensitivity Variation with Blade Design Features

The subsequent sensitivity study aimed to identify desensitizing blade design characteristics and to provide a database to identify common flow features which contributed to the desensitization. The blade design characteristics investigated were: camberline change, sweep, lean, chordwise sweep and dihedral.

A new baseline reference rotor blade design, over which one has more control than the proprietary PWC geometry, was first produced and design variations were applied to this design. A sensitivity study was carried out for the new baseline and each design variation. The details of blade design program can be found in Appendix B.

To assess each design variation, such as camber change, sweep, lean, chordwise sweep or dihedral, the variation was applied upon the new baseline blade design in a supposedly positive (beneficial) and opposite directions. Considering both trends would provide clues for the desensitization mechanism. To validate the predicted trends and quantify the change in sensitivity, speedline simulations at different tip clearances were performed, ensuring sensitivity studies carried out for each of the two opposite designs. Second, in the case that the hypothesis and/or the corollary(s) failed, the sensitivity results would provide the necessary database to continue the studies.

To ensure a fair comparison with the baseline design, for each design variation the design corrected mass flow is kept constant by changing the leading edge angle by altering the flow incidence to achieve the same maximum efficiency flow coefficient. The total pressure ratio and spanwise loading were kept constant by changing the trailing edge angle by altering the flow turning along the span. The spanwise loading was plotted using enthalpy based loading coefficient (ψ), whose

formulation is presented Equation 2.7, where $h_{t,3}$ and $h_{t,2}$ represents total enthalpy in stationary frame at 10% away from trailing edge plane and leading edge plane, respectively.

$$\psi \;\; = \;\; \frac{h_{t,3} - h_{t,2}}{U^2} \tag{2.7}$$

For each design variation, speedlines are obtained to find optimum mass flow rate for 0.4%, 0.9% and 1.3% chord. To assess the effect of chordwise blade loading, the pressure loading difference ($C_{p,ps}$-$C_{p,ss}$) at the blade tip and tip clearance flow is checked. The pressure difference is taken 0.001 inch below the blade tip. The formulation for tip loading ($C_{p,ps}$-$C_{p,ss}$) is given in Equation 2.8.

$$(C_{p,ps} - C_{p,ss}) \;\; = \;\; \frac{P_{ps} - P_{ss}}{\frac{1}{2}\,\rho_2\,U_{tip}^2} \tag{2.8}$$

Next, the general and detailed sensitivity studies were performed for each design variation. Stability sensitivity was analyzed via interface position since, simulating speedlines up to stall point for each design variation would take too much computational time.

2.3 Phase 3: Identification, Validation and Explanation of Desensitizing Flow Features

In Phase 3, identification of the desensitizing flow features was performed first using the database provided by the blade design variation in Section 2.2.3. This database was divided into lower and higher sensitivity group. In both sensitivity groups a trend was searched using detailed flow field analysis and using the clues from literature review, i.e. reducing local blade incidence, increasing local axial momentum and circumferential momentum at the tip, reducing double leakage and having higher stall margin. This trend gave the desensitizing flow features. Next, the desensitizing flow features were validated using simple numerical experiments or simulations. In the validation, the desensitizing flow features were applied to the baseline designs by changing boundary conditions or number of blades to see if the trend could be isolated. Last but not least, the physical mechanism(s) behind the desensitizing flow features were explained based on the flow physics.

2.4 Phase 4: Blade Design Characteristics to Exploit Desensitizing Flow Features

The last phase of this research, blade design characteristics that incorporated the desensitizing flow features were proposed and assessed. The assessment was carried out by designing blades, checking the intended desensitization flow feature and then making a sensitivity analysis to confirm the design. The outcome of this exercise would provide newly desensitized (or reduced sensitivity) blade designs, which could be used as basic design features for future blade designs.

Chapter 3

Results

In this Chapter, results are presented according to the four phases of the methodology.

3.1   Phase 1: Computational Setup

3.1.1   Computational Tool and Mesh Selection

Two mesh studies, which are streamwise and spanwise, were conducted to validate computational setup using the NASA Rotor 37 blade profile. The streamwise (and pitchwise) mesh resolutions are given in Table 3.1 and the convergence of both total-to-total pressure ratio and total-to-total efficiency were checked graphically, as shown in Figure 3.1. Both the pressure ratio and efficiency converged at a streamwise fine mesh of 82 nodes.

Table 3.1: Mesh resolutions for streamwise mesh convergence study

Direction	Number of Nodes			
Streamwise	48	66	82	98
Pitchwise	54	62	70	78
Spanwise	100	100	100	100
Total	~3×10^5	~4×10^5	~5×10^5	~7.5×10^5

Spanwise mesh resolutions are given in Table 3.2 and the convergence of both total-to-total pressure ratio and total-to-total efficiency are presented graphically in Figure 3.2. While all but the coarse (50 nodes) case gave similar values of pressure ratio and efficiency, 100 nodes was selected for conservatism to keep tip clearance mesh density high, as recommended by Van Zante *et al.* (2000).

Table 3.2: Mesh resolutions for spanwise mesh convergence study

Direction	Number of Nodes			
Streamwise	82	82	82	82
Pitchwise	70	70	70	70
Spanwise	50	75	100	150
Total	~3×10^5	~4×10^5	~5×10^5	~7.5×10^5
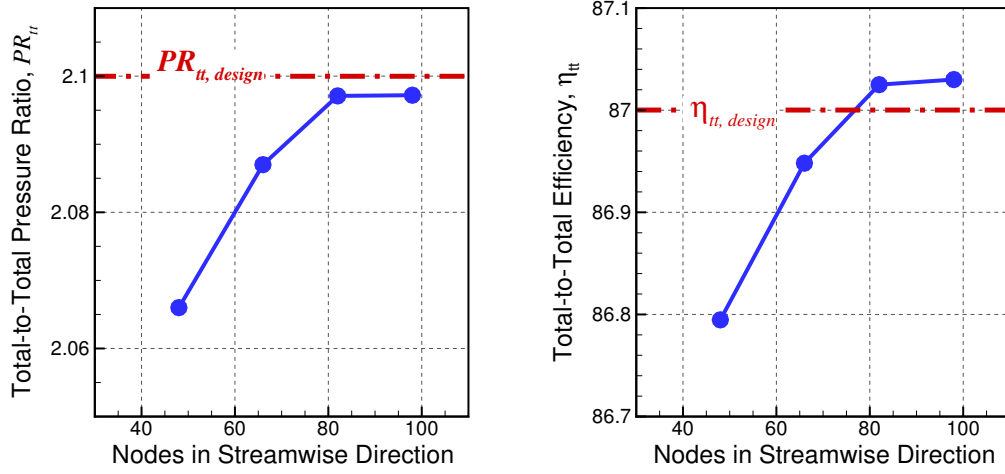
Figure 3.1: Rotor 37 streamwise mesh convergence of total-to-total pressure ratio and efficiency
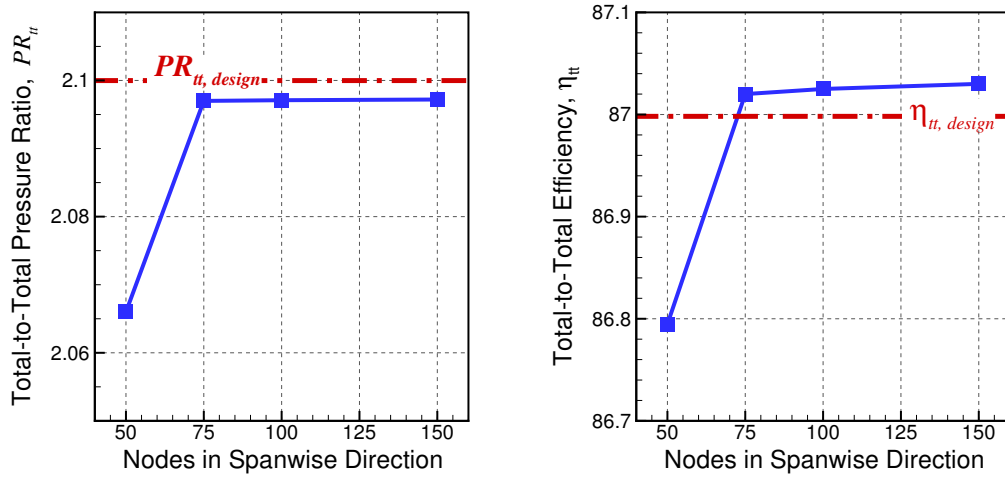
Figure 3.2: Rotor 37 spanwise mesh convergence of total-to-total pressure ratio and efficiency

Based on the above results, the mesh resolution selected was 82 streamwise, 70 pitchwise and 100 spanwise nodes for nominal tip clearance of 0.4% chord. Same mesh resolution was used for solving passage flows around the PWC Rotor and DCA Rotor profiles for the same nominal tip clearance. For higher tip clearances, two cells were added for each additional 0.1% chord tip clearance in spanwise direction. In other words, a blade passage with a 0.9% chord tip clearance had 110 spanwise nodes and with a 1.3% chord tip clearance corresponded to 120 spanwise nodes, etc.

3.1.2   Computational Tool Validation

In terms of integral performance, design mass flow rate, total pressure ratio and peak efficiency values were compared to experimental values (Suder and Celestina, 1996) in Table 3.3. The results from the simulation with CFX were within 0.5% error.

Table 3.3: Validation of Computational Setup with Rotor 37

Property	Experiment	CFX	Error [%]
Corrected Design Mass Flow Rate	20.19 kg/s	20.19 kg/s	0.0
Design Pressure Ratio	2.1	2.097	0.4
Peak Efficiency	87	87.025	0.03

Simulated blade passage flow field at design corrected mass flow were compared with experimental (Suder *et al*., 1995) and other numerical results (Hah, 2009; Arima *et al*., 1999) using relative Mach contours at 70% span in Figure 3.3. This comparison was important to show that the solver was capable of capturing the flow field accurately. As observed from the figure, the current CFX solver with SST turbulence model and other numerical studies captured very well the shock trajectory, which extended from the 40% chord of lower blade's suction side to the leading edge of upper blade's pressure side. Moreover, the main Mach contours in the passage and wake were also relatively well captured. Thus, it can be concluded that the lower span passage flow field was well simulated.

The relative Mach contours at 95% span (the blade tip is at 99.5% span) from experimental (Suder *et al*., 1995) and other numerical studies (Hah, 2009; Arima *et al*., 1999) are compared in Figure 3.4. The figure indicates although the main flow features such as wakes and Mach contours away from the shock captured by CFX resembled those of the experimental flow field, the shock trajectory was not as well-captured near the suction side. The experimental flow field shows that the shock lays slightly upstream of the leading edge and its trajectory turned downstream near mid-pitch and then upstream near the suction side. These features seemed to be well-captured by LES simulations of Hah (2009), but the CFX simulations with SST turbulence model seemed to

(a) Experimental Measurements using Laser Anemometer (Suder *et al.*, 1995)

(b) Numerical Study with LES (Hah, 2009)

(c) Numerical Study with RANS using $k - \epsilon$ Turbulence model (Arima *et al.*, 1999)

(d) Current Numerical Study with CFX (RANS using SST Turbulence model)

Figure 3.3: Comparison of relative Mach contours of Rotor 37 at 70% span
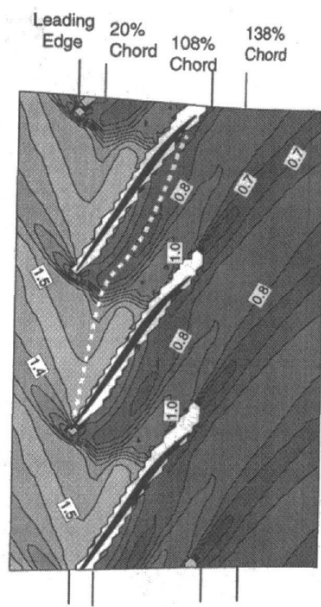
(a) Experimental Measurements using Laser Anemometer (Suder *et al*., 1995)
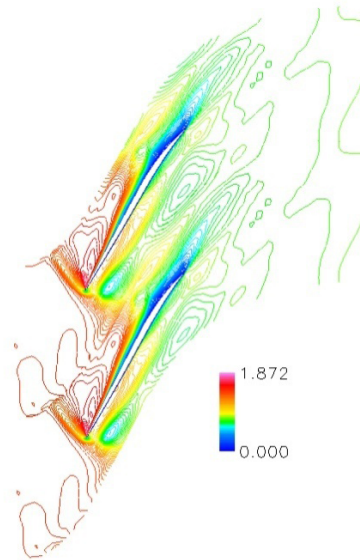
(b) Numerical Study with LES (Hah, 2009)
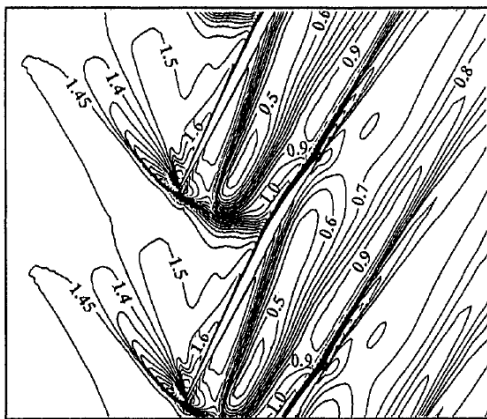
(c) Numerical Study with RANS using $k - \epsilon$ Turbulence model (Arima *et al*., 1999)
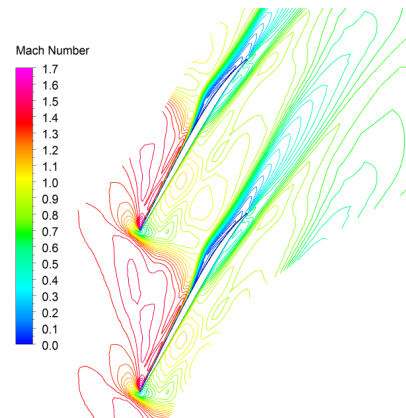
(d) Current Numerical Study with CFX (RANS using SST Turbulence model)

Figure 3.4: Comparison of relative Mach contours of Rotor 37 at 95% span

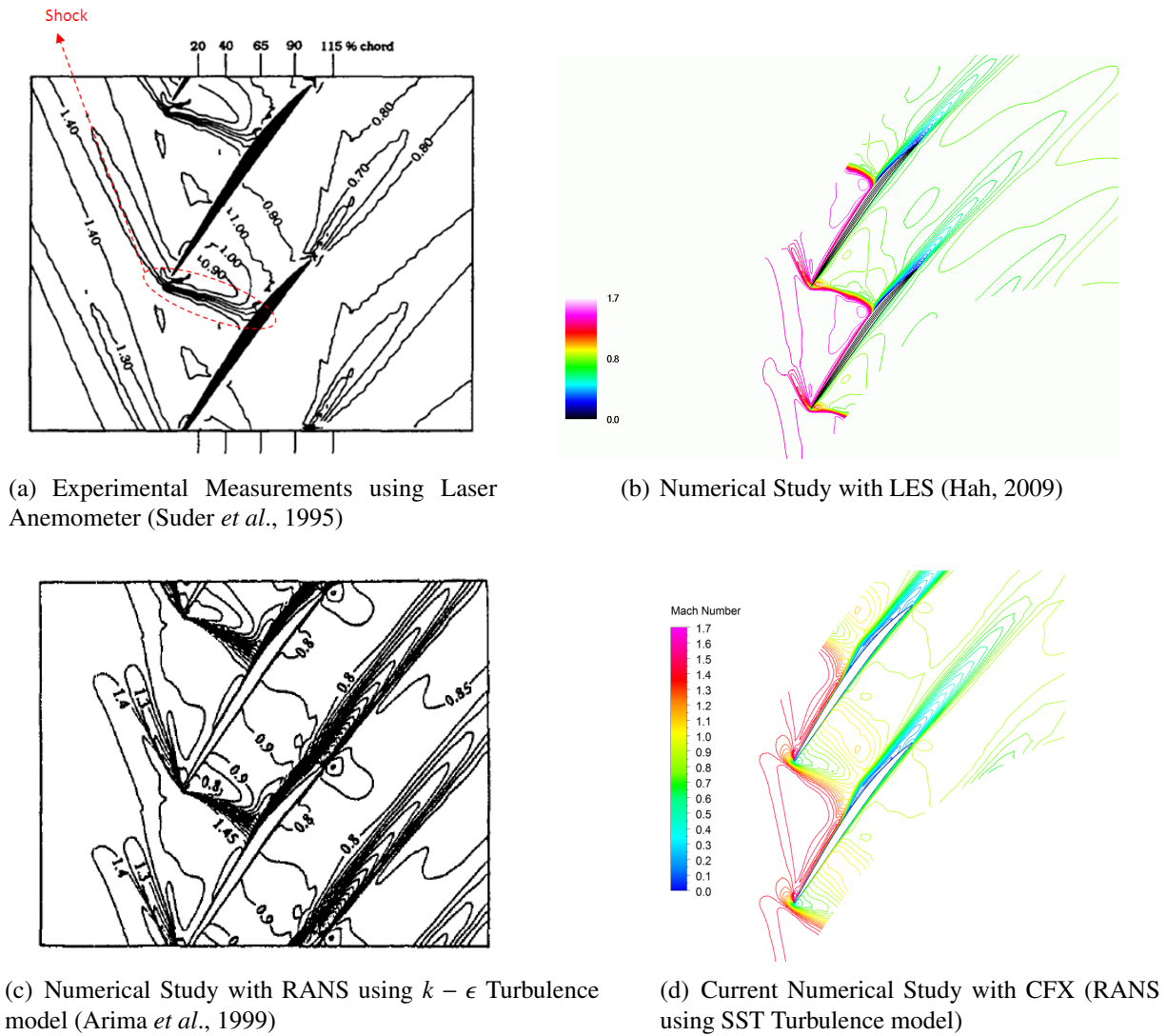underestimate the curvature of the shock trajectory. However, the simulation from Arima *et al.* (1999) with $k - \epsilon$ turbulence model performed even worse and also puts the shock at the leading edge. Thus, it can be seen that the CFX simulations with SST were superior to those using RANS with $k - \epsilon$ model solutions, but not as good as LES solutions. The LES model had the highest fidelity among numerical solutions compared, however, it costs more in terms of computational time and resources.

The CFX 13 Solver provided good results in the axial compressor rotor passage and its blade tip region at design point. Although, the shock trajectory in tip region flow field was not captured with high accuracy, the aim of this study was to analyze integral performance and stability and not the exact positions of shocks. In addition, since only trends are important for the current research, the CFD solver chosen was judged to be adequate.

3.2   Phase 2: Sensitivity Study

3.2.1   Preliminary Sensitivity Study

The results from the basic sensitivity study carried out on the Pratt & Whitney Canada rotor geometry to verify the hypothesis that tip blockage is the most sensitive parameter to tip clearance are presented in Figures 3.5 to 3.8.

The variation of total pressure ratio and efficiency with corrected mass flow rate for different tip clearances is given in Figure 3.5. As expected, the pressure ratio and efficiency drop as the tip clearance increases. The maximum efficiency occurs at a corrected mass flow rate of 3.49 kg/s for all three simulated tip clearances.

It is noted that, for a general sensitivity study capturing the stall point was highly challenging due to slow convergence of transient simulations at lower mass flow rates. Lowering mass flow rate by back static pressure had its limits in capturing stall point, since this approach could not capture any solutions (including the stall point), that lay at mass flows lower than the zero-slope peak of the (constant) domain inlet total-to-domain exit static pressure rise characteristic. The variation of total-to-static pressure ratio (domain inlet P_t to domain exit P_s) with corrected mass flow rate for different tip clearances is given in Figure 3.6, which indicates that the last points of simulation had almost the zero-slope peak of the total-to-static pressure rise. Thus, numerical simulations could not capture solutions at lower mass flows.

Further analysis revealed that the PWC rotor was not a tip-critical blade, since it stalled due to hub/boundary layer separation. The flow field analyses showed that hub/boundary layer separation bubbles appeared in lower mass flow rates, expanding near stall and ultimately causing stall through corner/boundary layer separation. Details are given in Appendix C.
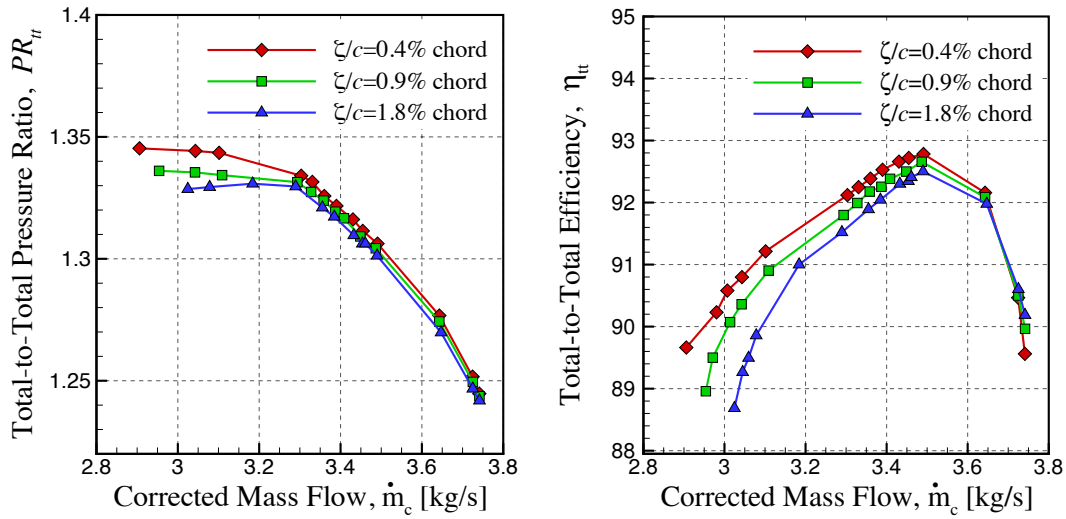
Figure 3.5: Total-to-total pressure ratio and efficiency curves for PWC rotor geometry at different tip clearances
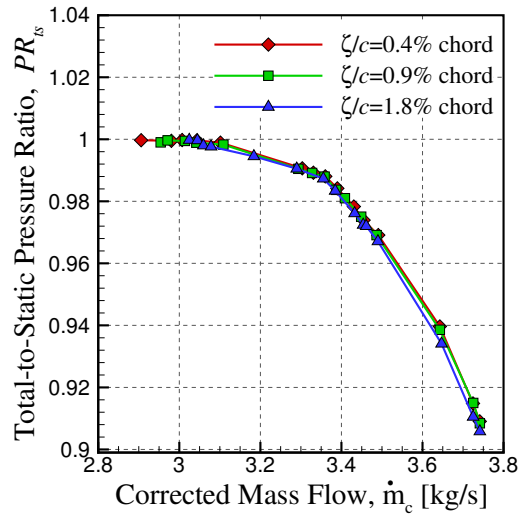
Figure 3.6: Total-to-static pressure ratio curves for PWC rotor at different tip clearances

The results of the general sensitivity study in terms of performance and stability parameters are shown in Figure 3.7, which plots the pressure ratio, efficiency and stall margin versus tip clearance at different corrected mass flow rates. The general sensitivity study showed that all the parameters decreased with tip clearance increase and the most drastic change occurred near stall. It is noted here that the slope of parameters indicate the sensitivity of each parameter to tip clearance and a zero slope would mean that a parameter is insensitive tip clearance size.
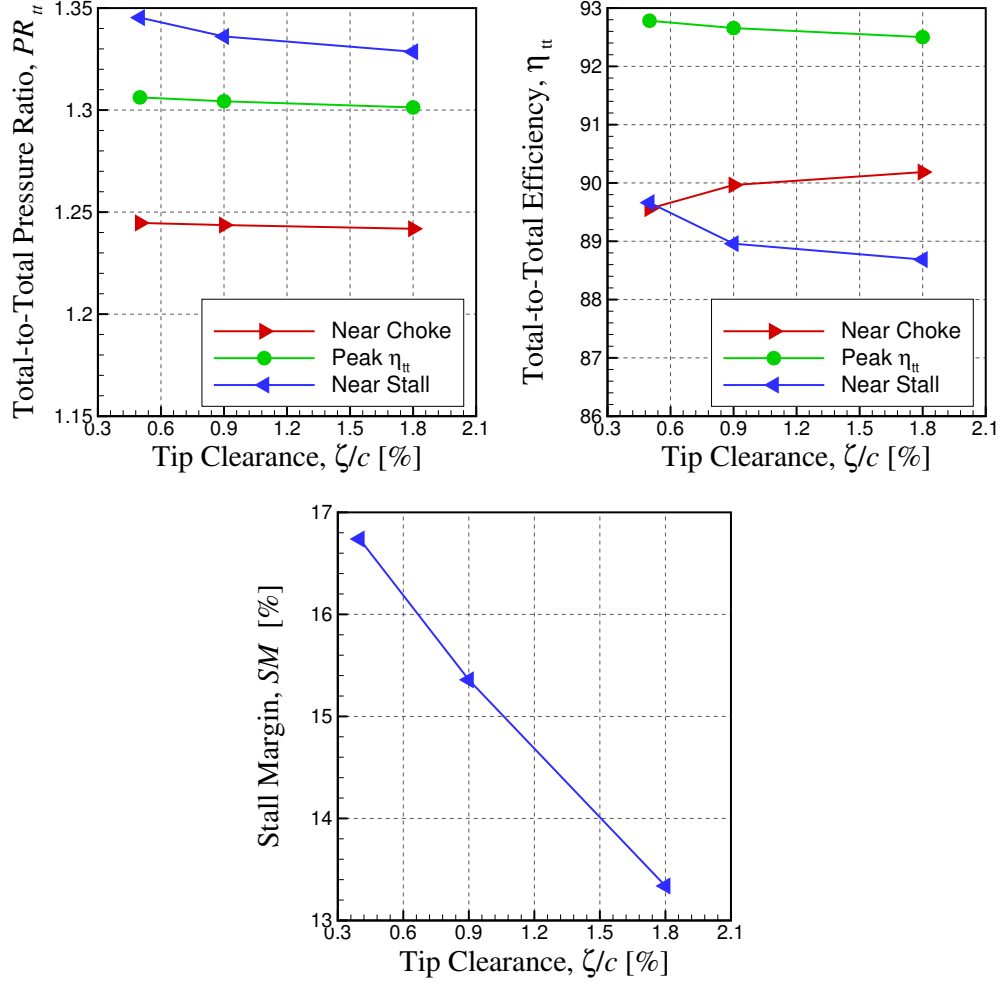
Figure 3.7: General sensitivity analysis for the PWC rotor

Next, a detailed sensitivity study was conducted in terms of loss and stability parameters, as shown in Figure 3.8 which plots the tip blockage, tip loss and incoming/tip clearance flow interface position versus tip clearance size at different corrected mass flow rates. The main observation was that tip blockage and tip loss were the most sensitive parameter to tip clearance. On the other hand, the incoming/tip clearance flow interface position stayed almost constant with tip clearance. This observation contradicted and disproved the hypothesis made in section 1.4.1, which predicted that tip blockage would be the only sensitive parameter to tip clearance.

Figure 3.8 shows that the incoming/tip clearance flow interface positions were not zero near stall. Were PWC rotor a tip-critical design, this would imply that the convergence limits in Figure 3.5 would not be the stall points and that the stall points might lay past the zero-slope peak.
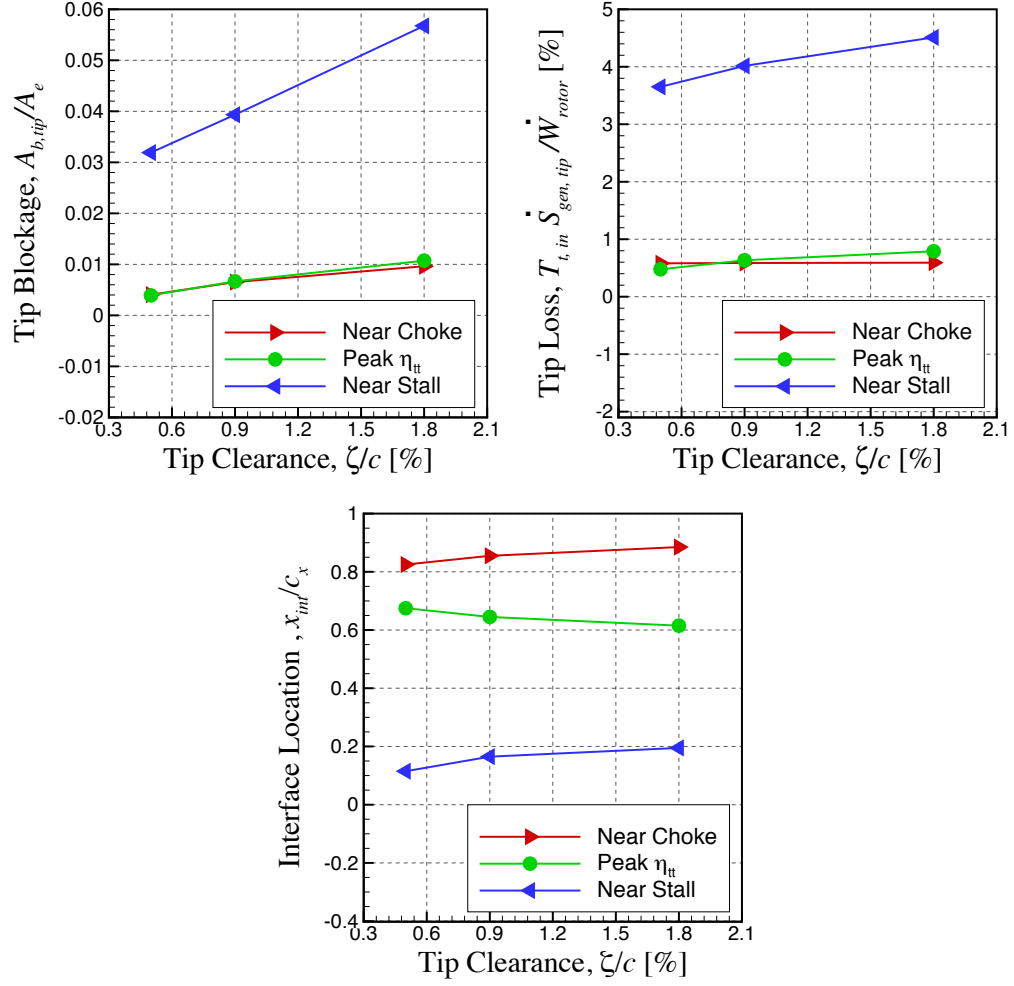
Figure 3.8: Detailed sensitivity analysis for the PWC rotor

3.2.2 Assessment of Sensitivity Variation with Blade Design Features

The hypothesis about tip blockage being the most sensitive parameter to tip clearance has been disproved, however, this only implies that desensitization mechanisms may be more complex than simply shifting the chordwise loading toward the trailing edge. Thus, the parametric study of design variations on sensitivity is more important to provide the clues to resolve these mechanisms.

It should be noted that only the speedlines of a few pertinent geometries were simulated all the way to the stall point. In view of the computational time and resources associated with simulating each speedline to the stall point, the stall margin was evaluated indirectly using the position of the incoming/ tip clearance flow interface. This was based on the assumption that all design variations were tip-critical because they should have the same spanwise loading as the reference blade, which was designed to be tip-critical.

The nominal performance of all design variations studied can be found in Appendix E.1.

Reference Blade

A reference rotor blade, which was a much simpler design compared to the PWC rotor, was designed to ensure ease of modifications according to design variations chosen in this study. It also served as a control/reference geometry for the evaluation of the design variations. Unlike the PWC rotor blade, this reference rotor blade was designed to be tip-critical, thus the effect of design variations on sensitivity of performance and stability to tip clearance would be more evident. The chosen reference design had the following features :

- *Double circular arc (DCA) profile*: It was composed of one circular pressure side arc and one circular suction side arc. It was a high-speed/transonic speed rotor profile for axial turbomachinery similar to the PWC Rotor.
- *Radially stacked*: It had neither lean nor sweep, thus, it was easier to sweep or lean and understand the effects of design changes.
- *Uniform circular arc camber*: It had one circular arc camber in an attempt to distribute the loading uniformly along the chord. This camber could then be changed to shift the loading toward the front or rear to assess the effects of camberline change.

A blade design program, whose details can be found in Appendix B, was used to generate the blade shape. The reference radially stacked DCA blade was designed with the design parameters shown in Table 3.4 whose values were based on the PWC rotor and the loading distribution of the PWC rotor at the first iteration. The schematic of the blade is given in Figure 3.9 and the details can be found in Appendix D.1.

Table 3.4: Input design parameters for the reference (BASE) rotor

Property	Value
Inlet Total Pressure	195.218 kPa
Inlet Total Temperature	483.35 K
Tip Mach	0.9
Hub-to-Shroud Radius Ratio	0.806738
Shroud Radius	0.141277 m
Flow Coefficient	0.5
Number of Blades	45
Mean Solidity	0.8
Mean Chord	0.0273 m
Stacking Line	0.5 chord

(a) Radially Stacked Blade, 3D View

(b) Tip Profile
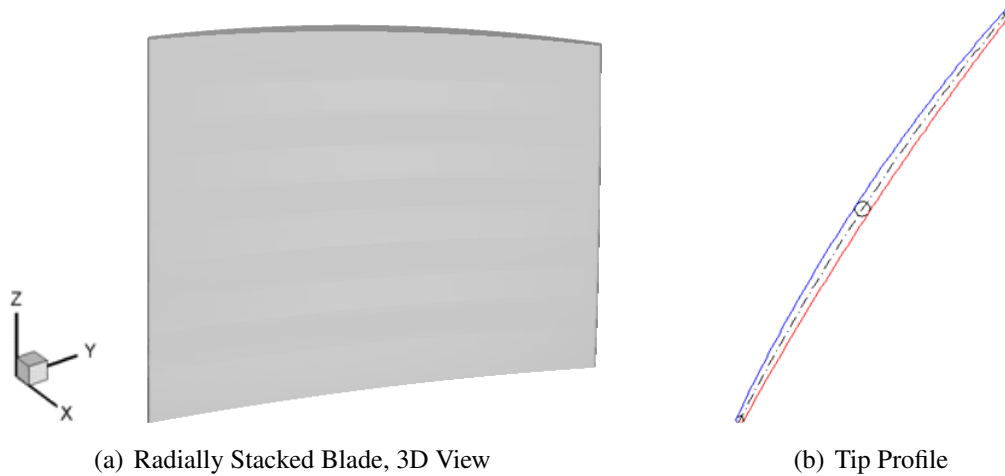
Figure 3.9: Schematic of the reference (BASE) rotor

Changes were made in gas path and inlet conditions from the PWC Rotor to simplify the design. First, the inlet flow was axial rather than swirling as in the case of the PWC rotor. Second, shroud radius was kept constant while the hub radius increased instead of decreasing hub and shroud radii as for the PWC rotor case. Keeping shroud radius constant provided ease of changing tip clearance especially for the eventuality that the design led to a real rotor for testing. Lastly, uniform inlet total pressure and temperature distributions were applied instead of the radial variable distribution of the PWC design that came with being a downstream stage.

The input loading distribution of the PWC rotor was changed throughout the design iterations for the reference. This change was due to hub/blade boundary layer separation resulting from high incidence and high flow turning in the hub region. The reference blade design was iterated to avoid hub/blade boundary layer separation. In the iteration process, the loading in the tip region was

set equal to or higher than that of the PWC rotor, to avoid prejudicing the sensitivity results with reduced tip loading and thereby penalizing the nominal performance. The details of the design iteration process can be found in Appendix D.2.

The spanwise loading distribution of final reference blade design, henceforth referred as BASE, is compared with that of the PWC rotor in Figure 3.10 (Formulation of the loading coefficient can be found in Appendix B). Figure 3.10 indicates that PWC rotor was highly loaded in hub, whereas the BASE rotor is evenly loaded. The BASE rotor's properties are compared with the PWC rotor in Table 3.5, which indicates that total efficiency and the stall margin were similar to that of PWC rotor while the total pressure ratio was slightly higher and the design mass flow was slightly lower. Unlike PWC rotor, which experiences stall due to hub/blade boundary separation, BASE rotor hypothesized and proved to be a tip-critical rotor such that it had no hub/blade boundary separation near stall and stall occurred when incoming/tip clearance interface reaches the tip leading edge plane. The speedlines of BASE rotor and proof of tip criticality are provided in Appendix D.3.
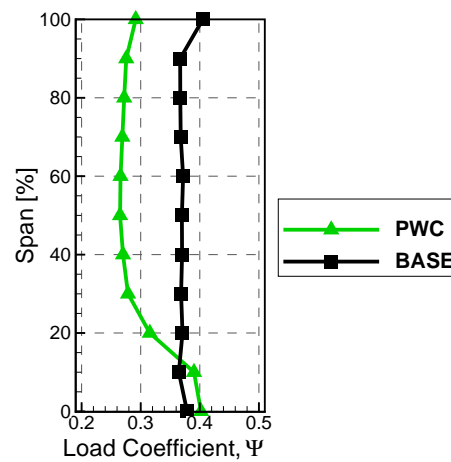
Figure 3.10: Loading distribution of final reference blade (BASE) design

Figure 3.11 plots the general sensitivity results for the BASE and PWC rotors. As expected, the BASE rotor had higher performance and stability sensitivity to tip clearance than the PWC Rotor, since the PWC rotor had lower tip loading. However, being more sensitive and tip-critical, the effects of design variations on BASE rotor should be more evident. Therefore, this reference rotor geometry formed the basis for studying the effect of design variations on sensitivity to tip clearance.

Table 3.5: Comparison of final parameters of reference blade (BASE) with those of PWC rotor

Property	PWC Rotor	BASE Rotor
Profile Type	Four CA (Special design)	DCA (Standard)
Hub Thickness	11% chord	7% chord
Tip Thickness	6% chord	3% chord
Nominal Tip Clearance	0.4% chord	0.4% chord
Corrected Design Mass Flow Rate ($\dot{m}_{c,design}$)	3.49 kg/s	3.04 kg/s
Total-to-Total Pressure Ratio (@ $\dot{m}_{c,design}$)	1.306	1.361
Total-to-Total Efficiency (@ $\dot{m}_{c,design}$)	92.78%	92.24%
Stall Margin	16.74%	16.61%
Tip Critical	No	Yes
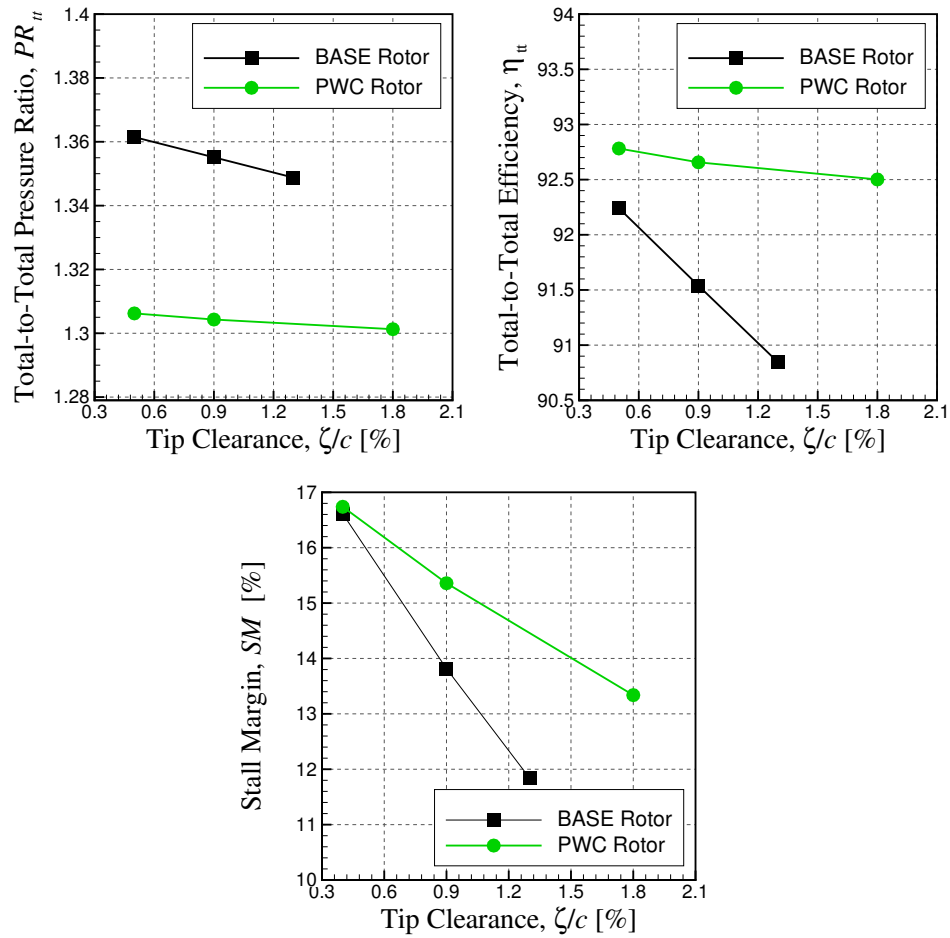
Figure 3.11: General sensitivity analysis of the BASE and PWC rotors at their corrected design (peak efficiency) mass flows ($\dot{m}_{c,BASE}$=3.04 kg/s, $\dot{m}_{c,PWC}$=3.49 kg/s)

Effect of Chordwise Camberline Change

The camberline change was achieved by modifying the chordwise camber at each spanwise location beyond mid-span. The chordwise camber was modified such that the flow turning was kept constant, but the shape of the camberline was changed. For the first iteration of a rear loaded blade, the distance between leading edge and mid-chord was unloaded by introducing linear camber, the portion from mid-chord to the trailing edge was loaded by introducing a circular arc camber which did all the necessary flow turning at the given span location. Since the double circular arc profile forced uniform camber distribution, a four-circular-arc profile was used for forward and rear-cambered blades. Boundary layer separations occurred for all blade design iterations, thus only 25% of the camberline was ultimately chosen to be linear for both forward and rear-cambered blades. Figure 3.12 compares the three blade designs with camberline variations, namely uniform-camber (BASE), rear-camber (RC) and front-camber (FC). One can notice that the rear-cambered blade had higher thickness at the aft region after the mid-chord and forward cambered has higher thickness at the forward region compared to the BASE blade. This change in thickness distribution was also made to avoid blade boundary layer separation.

(a) BASE   (b) RC   (c) FC
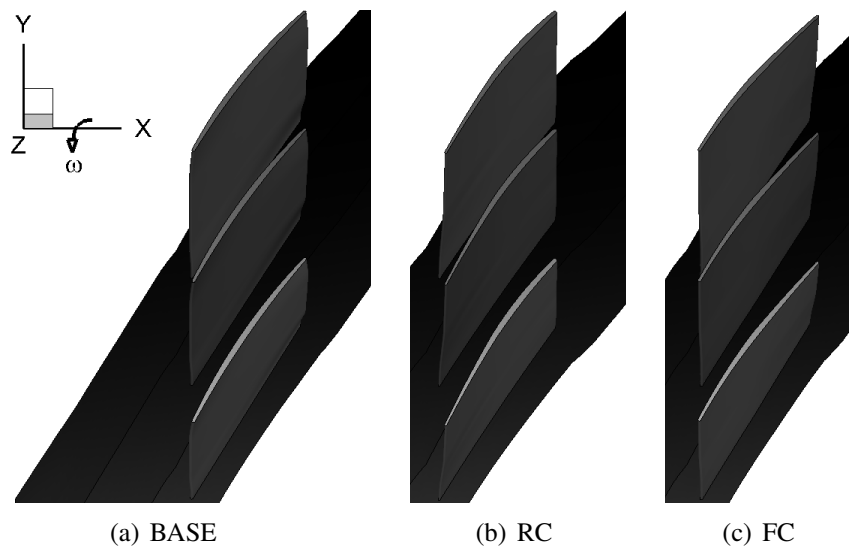
Figure 3.12: Design Variation 1: Chordwise Camber

First, the spanwise loading distributions for the designs with camberline variation are plotted in Figure 3.13(a) for the FC, RC and BASE rotors for nominal tip clearance of 0.4% chord at a corrected mass flow of 3.04 kg/s, which was the design corrected mass flow. Figure 3.13(a) shows that all blades had similar spanwise loading, ensuring that the sensitivity changes would not be caused by tip loading reduction. Figure 3.13(b) compares the chordwise distribution of the tip loading and tip clearance mass flow for these rotors. It shows that the maximum loading point

(and maximum tip clearance flow), which was almost at the leading edge (x/c =0) for the BASE blade, moved downstream by 0.4 chord in the rear cambered blade, but hardly moved in the front cambered design. Higher rear camber would further shift this point but it would cause boundary layer separation on the blade suction side. Therefore, camberline change has limited leverage on chordwise tip clearance flow distribution, at least for the blade design method and thickness distribution used.

(a) Spanwise loading distribution

(b) Chordwise distribution of tip loading and tip clearance mass flow
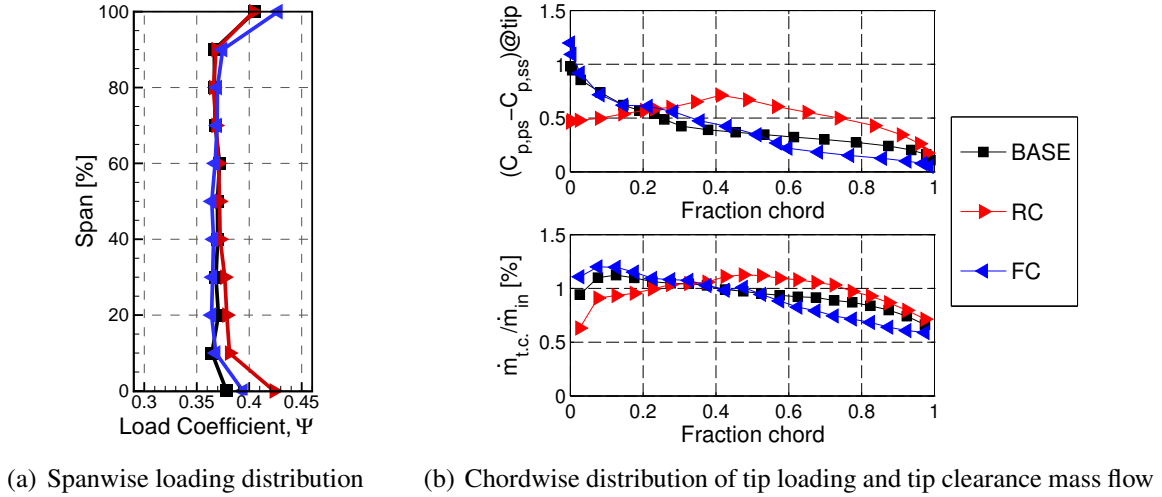
Figure 3.13: Spanwise and chordwise distributions for different camber lines at design corrected mass flow rate and nominal tip clearance

The results of the general sensitivity study in terms of the total pressure ratio and efficiency are shown in Figure 3.14. They indicate that, FC resulted in a reduction in efficiency and pressure ratio sensitivity to tip clearance, whereas the first corollary presented in Section 1.4.2 would have predicted the RC rotor to have less sensitivity. Therefore, the first corollary in Section 1.4.2 is refuted.

Figure 3.15 plots the results for the detailed sensitivity study, which confirmed the trends observed in Figure 3.14 by showing that tip blockage, tip loss and incoming/ tip clearance flow interface position for FC rotor were the least sensitive to tip clearance size. The only disadvantage of forward camber was the upstream position of the incoming/ tip clearance flow interface indicating lower nominal stall margin. Additionally, literature show that forward camber was not preferred in transonic applications since it increases shock strength.
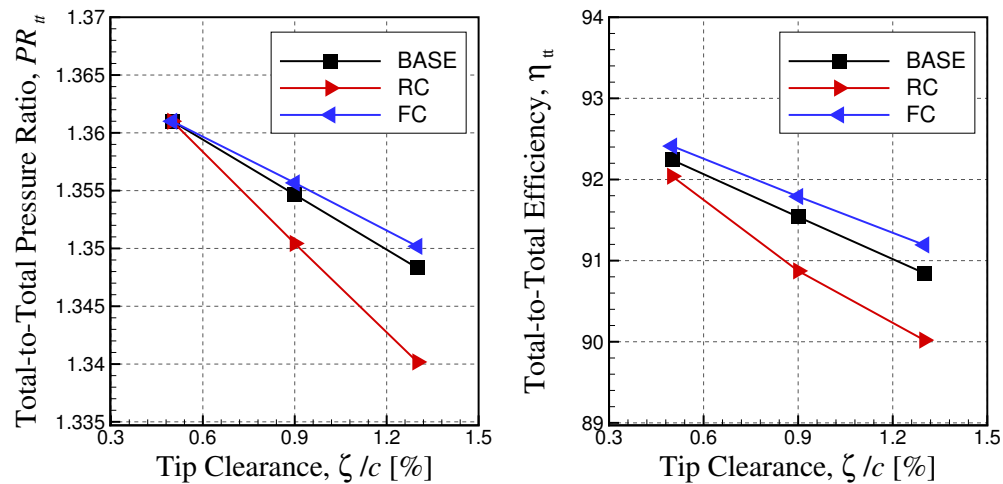
Figure 3.14: General sensitivity to tip clearance for different tip chordwise cambers
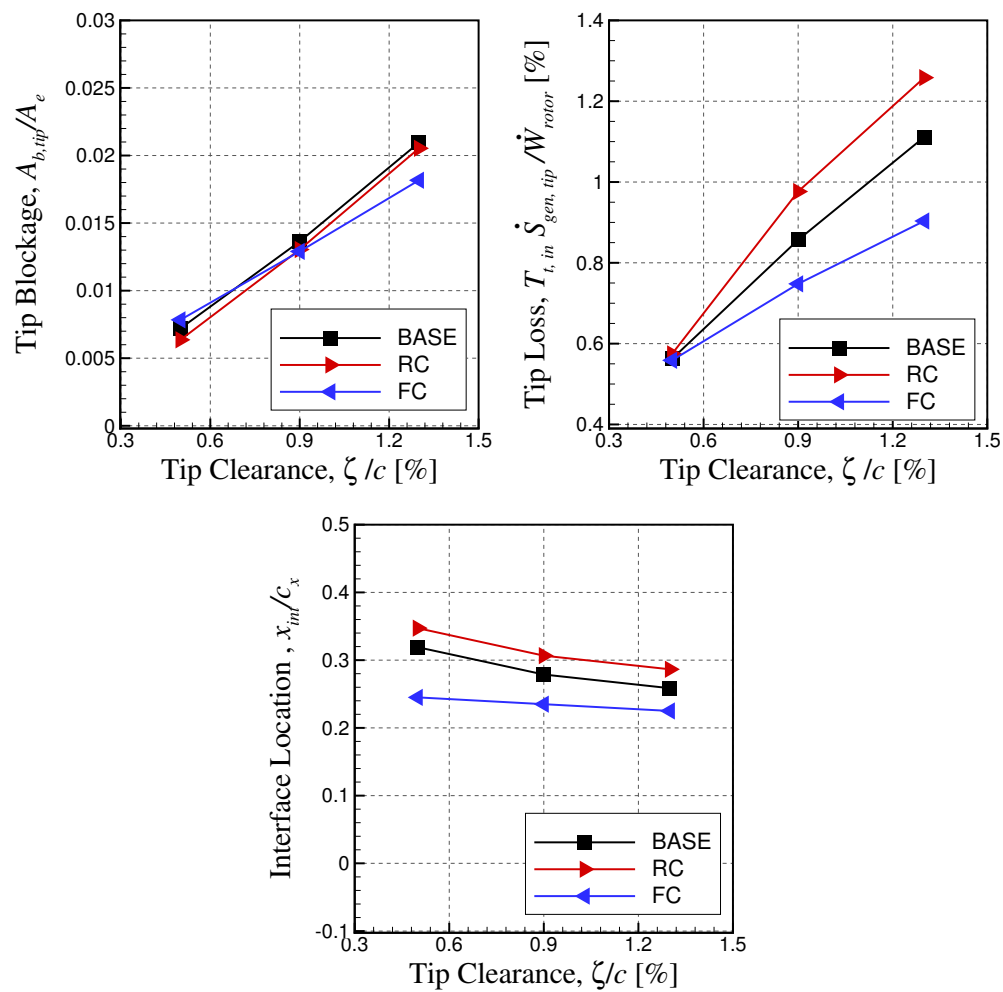
Figure 3.15: Detailed sensitivity to tip clearance for different tip chordwise cambers

Effect of Axial Sweep Change

To assess the effect of sweep on sensitivity, the BASE blade hub and tip was swept through axial deviation of the blade stacking line. The opposite angled hub and tip swept blades are compared against the radially stacked BASE rotor in Figure 3.16. Both blades had 20° sweep angle calculated from the mid-span both at the hub and tip regions. The 20° sweep angle was applied at both hub and tip regions because the literature review (McNulty *et al.*, 2004; Bonaiuti *et al.*, 2007; Ramakrishna and Govardhan, 2009a, 2010) reveal that the sweeps around 20° gave beneficial results in terms of nominal performance, stability and sensitivity of these to tip clearance. Whereas at higher (30°) or lower (10°) sweeps the effect was reduced (Bonaiuti *et al.*, 2007; Ramakrishna and Govardhan, 2009a) and at higher sweep angles machining and/or structural problems would be incurred.

(a) BASE   (b) FAS   (c) BAS
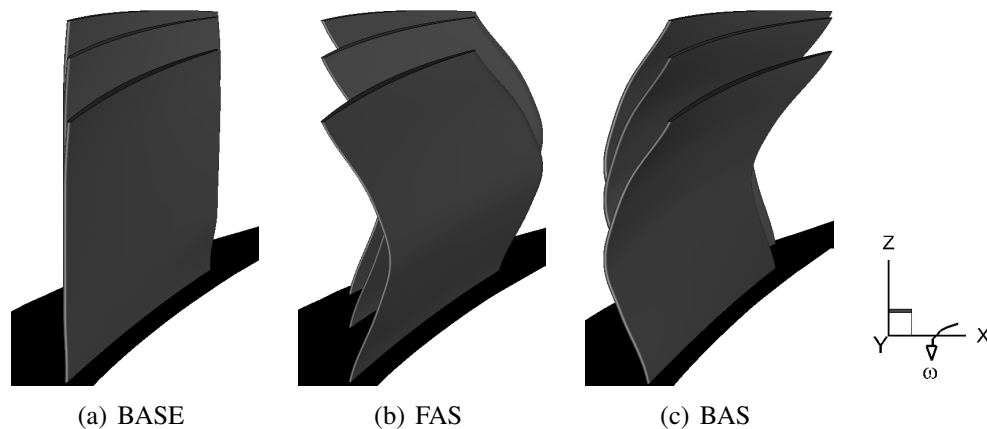
Figure 3.16: Design variation 2: Sweep

Figure 3.17(a) compares the spanwise (enthalpy) loading distribution of BASE, forward axial sweep (FAS) and backward axial sweep (BAS) for nominal tip clearance of 0.4% chord at the design corrected mass flow of 3.04 kg/s. Figure 3.17(a) indicates that FAS and BASE blade had similar spanwise loading, however, BAS had lower loading below the mid-span and higher loading above the mid-span. The lower spanwise loading below the mid-span of the BAS rotor was designed to eliminate blade boundary layer boundary layer separation near hub. To compensate, the loading is increased beyond mid-span to keep nominal performance similar to the BASE blade. As observed, between 90% to 100% span near the blade tip there was a increase in (enthalpy) loading coefficient of 0.03. This increase in (enthalpy) loading coefficient could increase the tip pressure loading and sensitivity to tip clearance. Therefore, in the following figures, the effect this increase in loading on tip pressure loading and sensitivity is checked.

The effect of sweep on chordwise distribution of tip loading and tip clearance flow are presented in Figure 3.17(b) for FAS, BAS and BASE rotors at the same corrected mass flow of 3.04 kg/s.

The results indicated that forward sweep shifted maximum loading and tip clearance mass flow downstream by about 0.2 chord, while backward sweep had hardly any effect. Moreover, the effect of higher enthalpy loading coefficient in the tip region for the BAS rotor (Figure 3.17(a)) was not evident in the pressure loading plot in Figure 3.17(b). Thus, a change of loading coefficient along the span within 0.03 was henceforth considered acceptable for assuming similar tip pressure loading. A comparison of Figure 3.17(b) with Figure 3.13(b) indicates that sweep seems to be less influential for shifting the chordwise distribution of blade loading and tip clearance flow than chordwise camberline change.

(a) Spanwise loading distribution   (b) Chordwise distribution of tip loading and tip clearance mass flow

Figure 3.17: Spanwise and chordwise distributions for different sweeps at design corrected mass flow and nominal tip clearance

The results from the general sensitivity study for sweep in Figure 3.18 indicated that FAS provided a reduction in efficiency sensitivity, but not in pressure ratio sensitivity to tip clearance. On the other hand, BAS reduces the pressure ratio sensitivity, at least at low tip clearance.

The results for the detailed sensitivity study are shown in Figure 3.19. BAS reduced tip blockage sensitivity and slightly the tip loss sensitivity to tip clearance, which was consistent with reduced pressure ratio sensitivity to tip clearance. The lower loss sensitivity of FAS translated into lower efficiency sensitivity. Additionally, BAS increased interface position, indicating a higher nominal stall margin, and both FAS and BAS seemed to reduce slope of interface position, indicating a lower stall margin sensitivity. These results further indicated that there was much more to desensitization mechanism than chordwise blade loading.
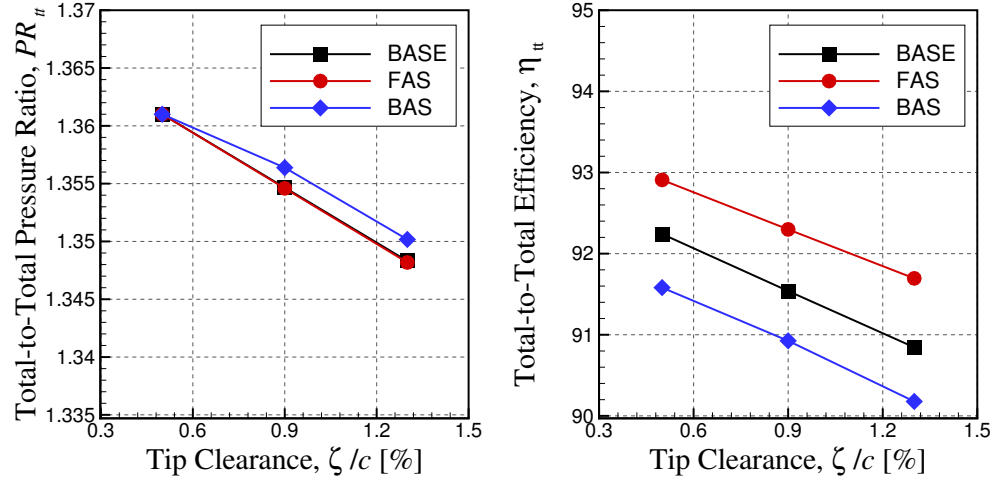
Figure 3.18: General sensitivity study for different axial sweeps
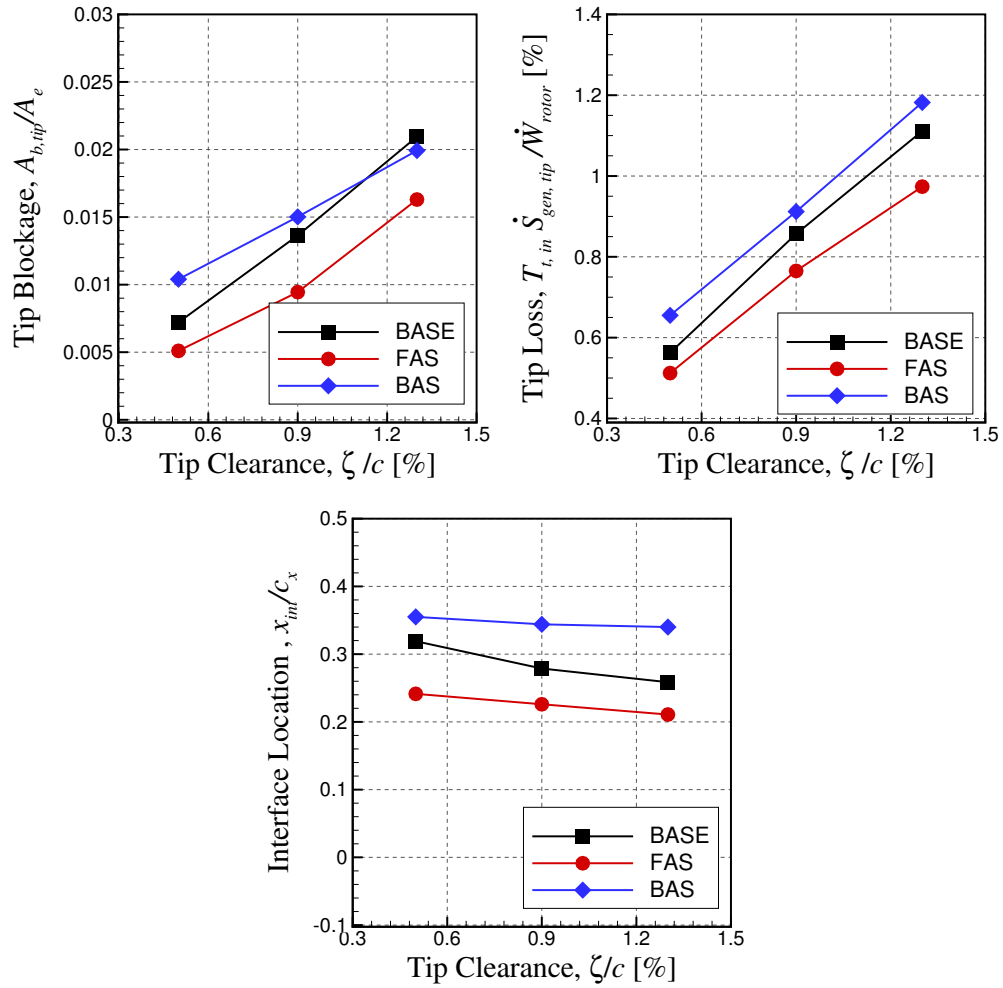
Figure 3.19: Detailed sensitivity study for different axial sweeps

Effect of Lean Change

For the evaluation of blade lean on sensitivity to tip clearance, the BASE blade was leaned in the tangential direction by 25° in either direction for the upper 50% span to produce the forward lean (FL) and back lean (BL) designs. FL and BL designs were compared against the BASE rotor in Figure 3.20. The literature review (Gallimore *et al.*, 2002a; Tschirner *et al.*, 2006) suggested that a lean angle around 25° would give better results in terms of nominal performance, stability and their sensitivity.

(a) BASE

(b) FL

(c) BL
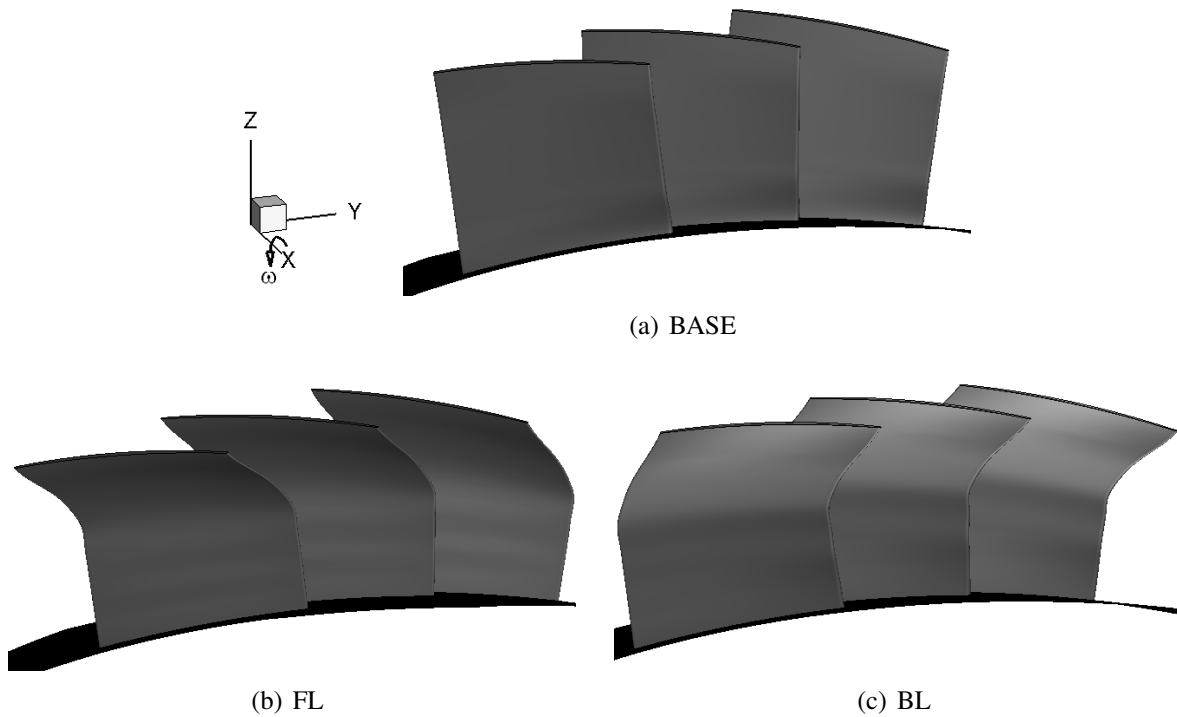
Figure 3.20: Design variation 3: Lean

Figure 3.21 presents the spanwise loading and the chordwise tip loading and tip clearance flow for FL, BL and BASE at their design corrected mass flow of 3.04 kg/s for nominal tip clearance. The spanwise loadings were again similar and the direction of the shift in the maximum blade loading and tip clearance flow was as expected. For the FL rotor, the highest loading point moved from the leading edge to 0.35 chord. Moreover, the FL rotor considerably reduced the tip clearance flow upstream of the maximum loading point compared to camberline change(Figure 3.13(b)) and sweep (Figure 3.17(b)), and exhibited the best behaviour in terms of tip clearance flow reduction. As expected, BL resulted n more tip loading and tip clearance flow near leading edge.

The designs with FL, BL and BASE are compared for performance sensitivity to tip clearance in Figure 3.22. FL did not affect the efficiency sensitivity and slightly reduced the pressure ratio

(a) Spanwise loading distribution
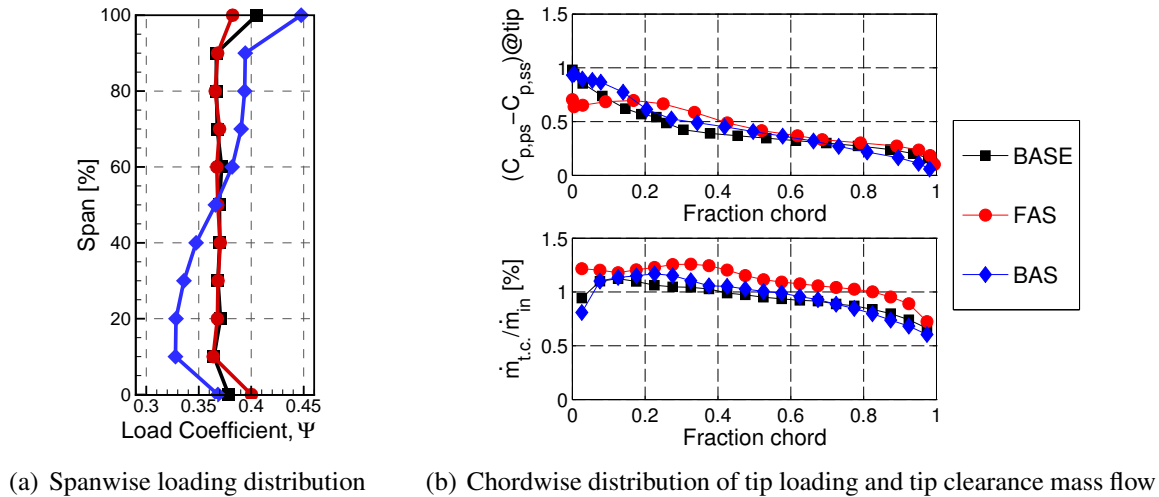
(b) Chordwise distribution of tip loading and tip clearance mass flow

Figure 3.21: Spanwise and chordwise distributions for different leans at design corrected mass flow for nominal tip clearance size

sensitivity. Also, BL did not affect efficiency sensitivity, but was detrimental to the pressure ratio sensitivity. The results are not consistent with both corollaries presented in Section 1.4.2, since FL rotor, which had aft-loading and obstructed the tip clearance flow path, predicted to have less sensitivity. Therefore, both corollaries in Section 1.4.2 are refuted.
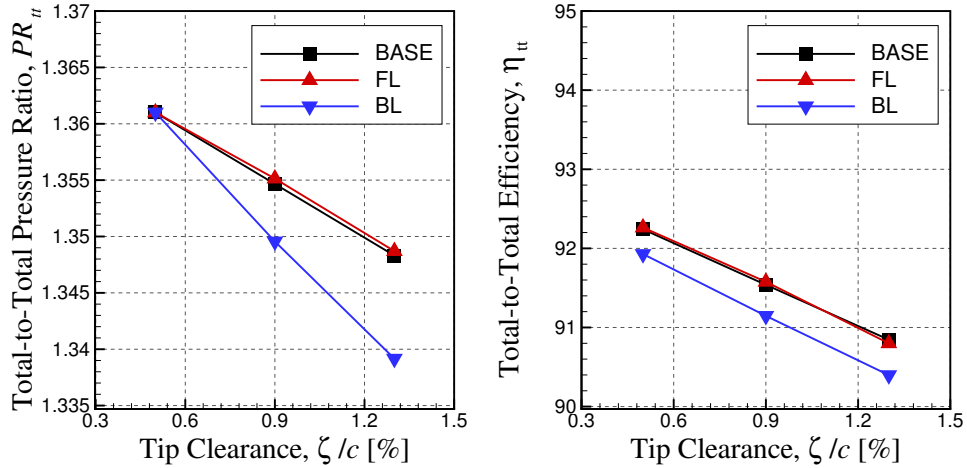
Figure 3.22: General sensitivity study for different leans

Figure 3.23 plots the results for the detailed sensitivity study. The tip blockage sensitivity was slightly reduced and the tip loss sensitivity was considerably increased by the BL rotor, which may explain its higher pressure ratio sensitivity. The FL rotor, on the other hand, reduced the tip loss
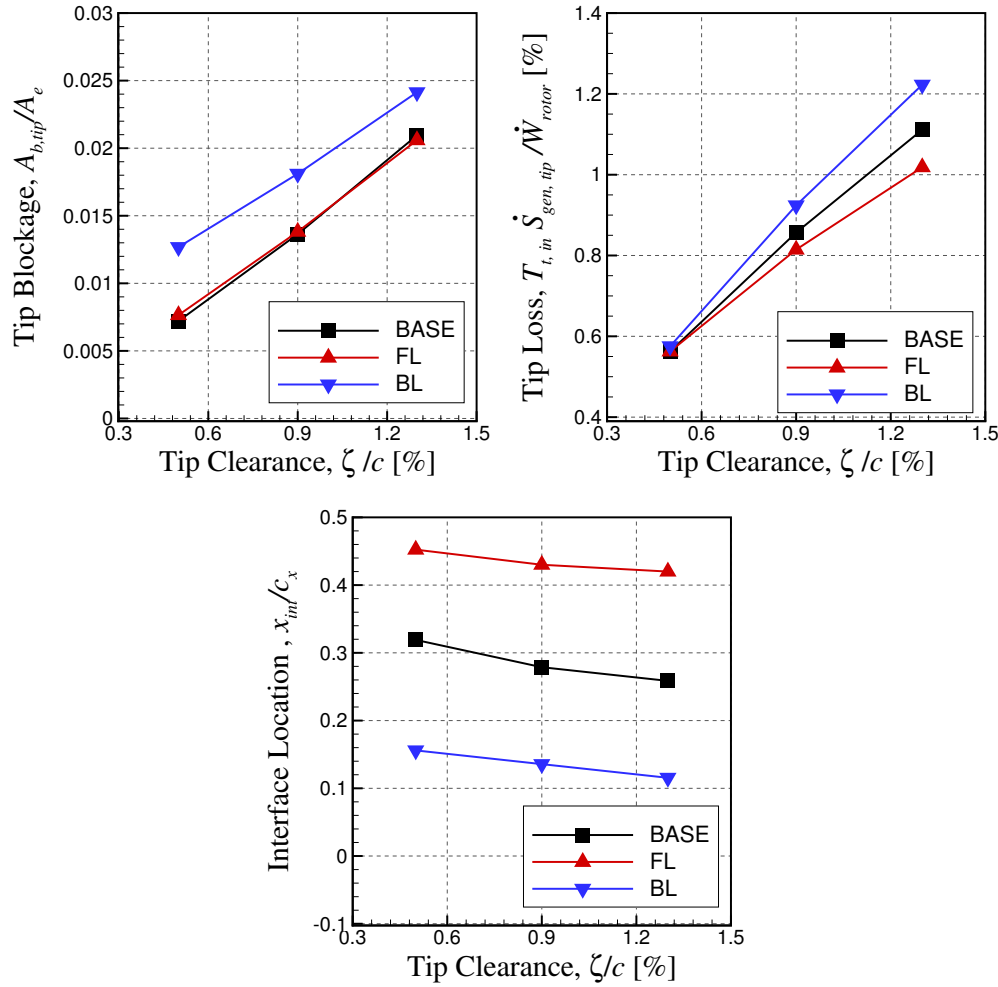
Figure 3.23: Detailed sensitivity study for different leans

sensitivity and did not noticeably affect the tip blockage sensitivity, however, only a small effect on the performance sensitivity was observed. The interface position plot shows that both FL and BL reduced the slope, with FL having higher interface position (more stall margin) and BL having lower interface position (less stall margin) than the BASE rotor. As in the case of sweep, the downstream shift of loading explains the shift of interface position. The fact that the downstream shift of loading and tip clearance flow, and obstruction of tip clearance flow path did not result in performance desensitization to tip clearance showed that the desensitization mechanism goes beyond this feature.

Effect of Chordwise Sweep Change

The effect of chordwise sweep on sensitivity to tip clearance is evaluated next. Forward (FCS) and aft chordwise swept (ACS) designs are shown in Figure 3.24. Similar to axial sweep, blade

hub and tip were swept with 20° sweep angle since literature (McNulty *et al.*, 2004; Ramakrishna and Govardhan, 2009a) suggested better nominal performance, stability and their sensitivity to tip clearance at 20° sweep.

(a) BASE

(b) FCS　　　　　　　　　　　　　　(c) ACS
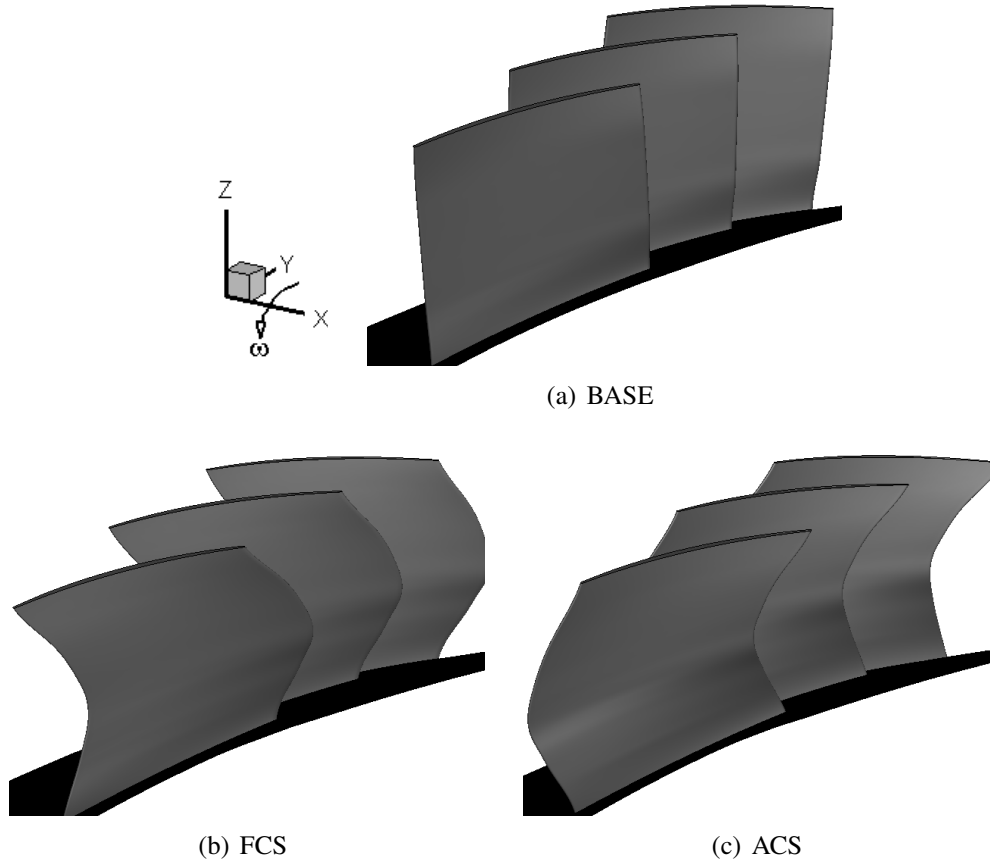
Figure 3.24: Design variation 4: Chordwise Sweep

The influence of chordwise sweep on spanwise loading distribution is presented in Figure 3.25(a). As in the case of BAS, boundary layer separations near the hub required a reduction of loading at lower spans and its increase at higher spans for both blades. There was a increase in loading coefficient of value 0.03, which proved to be ineffective in increasing tip pressure loading or sensitivity in analysis of BAS. The chordwise distribution of tip loading and tip clearance flow for chordwise sweep is presented in Figure 3.25(b). As expected from the literature review, FCS shifted the tip loading and tip clearance flow downstream while ACS did the opposite. FCS shifted the highest loading point to 0.4 chord, which was at the leading edge for the BASE rotor. Since FCS is composed of forward lean and forward sweep, it also reduced the tip clearance flow in the upstream chordwise region.

The results of the general sensitivity study in terms of the total pressure ratio and efficiency

(a) Spanwise loading distribution

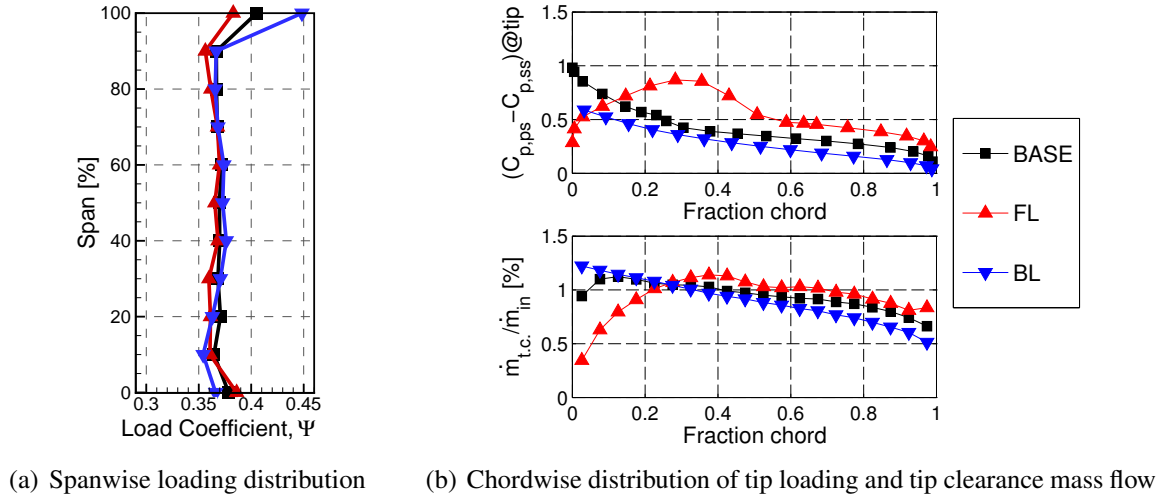(b) Chordwise distribution of tip loading and tip clearance mass flow

Figure 3.25: Spanwise and chordwise distributions for different chordwise sweeps at design corrected mass flow for nominal tip clearance size

are shown in Figure 3.26, which indicates that FCS reduced both pressure ratio and efficiency sensitivity to tip clearance. However, ACS despite its front loading, had lower efficiency sensitivity to tip clearance. Again these results contradicted the corollaries of rear loading and/or forward leaning would lower tip clearance sensitivity.
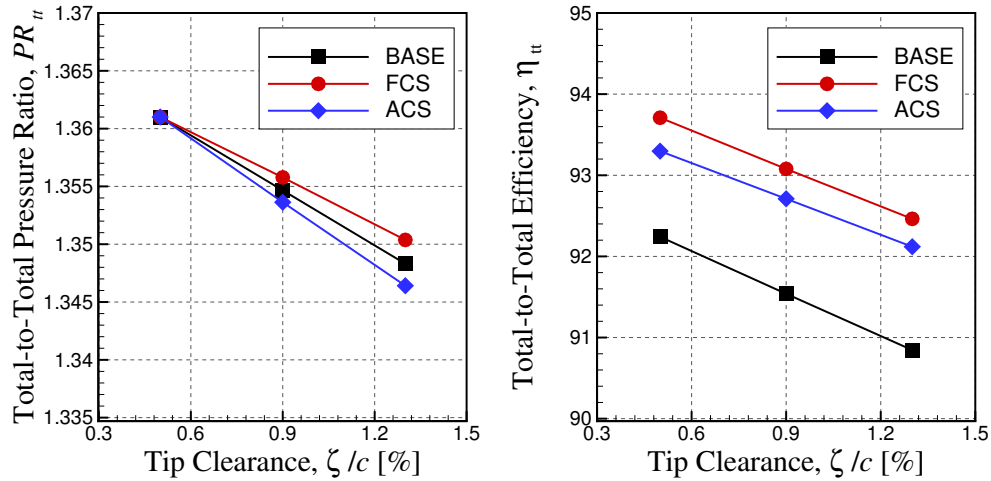
Figure 3.26: General sensitivity study for different chordwise sweeps

Analysis of chordwise sweep sensitivity to tip clearance also showed the effect of combining blades. FCS is combination of FAS and FL which exhibited reduced efficiency and/or pressure ratio sensitivity to tip clearance, one may conclude that that these effects are combined in the FCS.

The results in Figure 3.26 agree well with this conclusion. On the other hand, ACS is composed of BAS and BL, where the former reduced the pressure ratio sensitivity and the latter increased, and neither of them changed the efficiency sensitivity considerably. However, the results in Figure 3.26 shows that ACS had the lowest efficiency sensitivity to tip clearance. Therefore, combining lower sensitivity blade features seemed to work in favour of desensitization. However, combining lower and higher sensitivity blades could produce unexpected results. One can conclude that there is much more to explore in desensitization mechanisms than combining the good characteristics.

The results for the detailed sensitivity study are presented in Figure 3.27 and the results were consistent with the general sensitivity results. FCS had the lowest tip blockage sensitivity which explains the least pressure ratio sensitivity to tip clearance and ACS had the lowest tip loss sensitivity which was consistent with the least efficiency sensitivity to tip clearance among the configurations tested. Additionally, the interface position of FCS was increased and its sensitivity was reduced, thus translating into higher nominal stall margin and lower stall margin sensitivity, respectively.
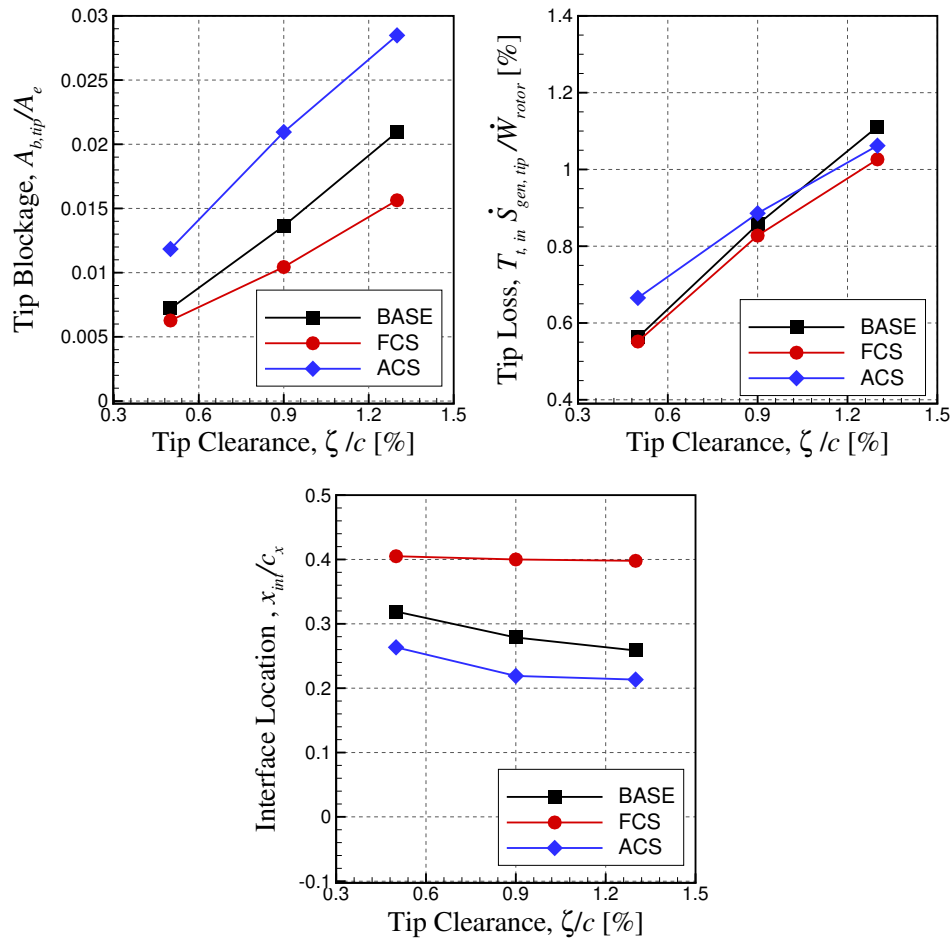
Figure 3.27: Detailed sensitivity study for different chordwise sweeps

Effect of Dihedral Change

The last design variation was dihedral; the positive (PD) and negative dihedral (ND) designs are shown in Figure 3.28. The blades were angled at 25°, as suggested in literature (Gallimore *et al.*, 2002a; Tschirner *et al.*, 2006).

(a) BASE

(b) ND   (c) PD
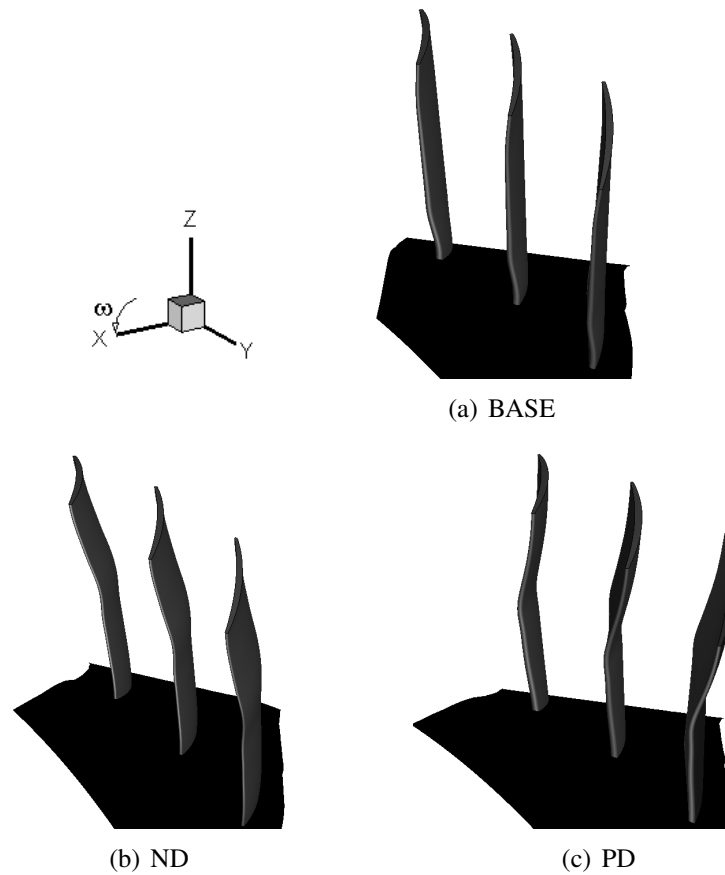
Figure 3.28: Design variation 5: Dihedral

Figure 3.29 plots the spanwise loading distribution (left plot) and the tip loading and tip clearance flow distribution (right plot) for ND, PD and BASE. The spanwise loadings were as close to BASE as possible. Only an increase in hub region for ND was observed. This increase in loading in hub region was not expected to affect pressure loading and/or sensitivity to tip clearance results. Figure 3.29(b) reveals that ND shifted the tip loading and tip clearance flow downstream and PD shifted them upstream. ND moved the highest loading point to 0.4 chord from the leading edge. ND was a combination of forward lean and backward sweep, thus was expected to reduce the tip clearance flow in the upstream chord region.
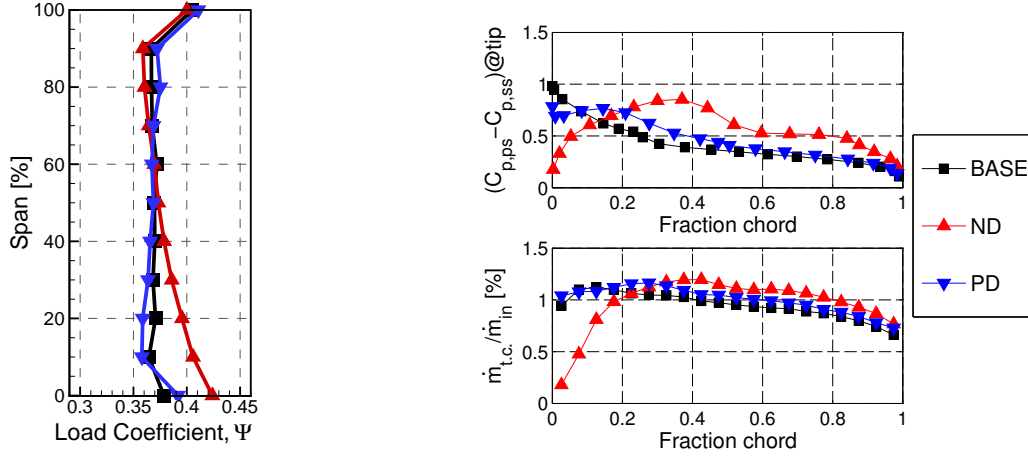
(a) Spanwise loading distribution

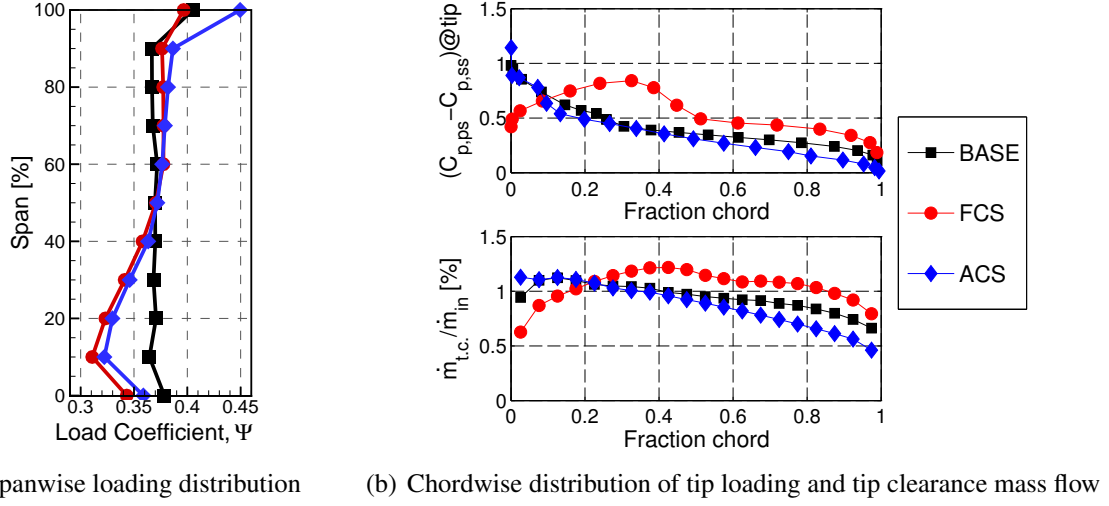(b) Chordwise distribution of tip loading and tip clearance mass flow

Figure 3.29: Spanwise and chordwise distributions for different dihedrals at design corrected mass flow and nominal tip clearance size

The results of the general sensitivity study in terms of the total pressure ratio and efficiency are shown in Figure 3.30. The figure indicates that in spite of the change in chordwise loading distribution, neither PD nor ND reduced the sensitivity of pressure ratio or efficiency.
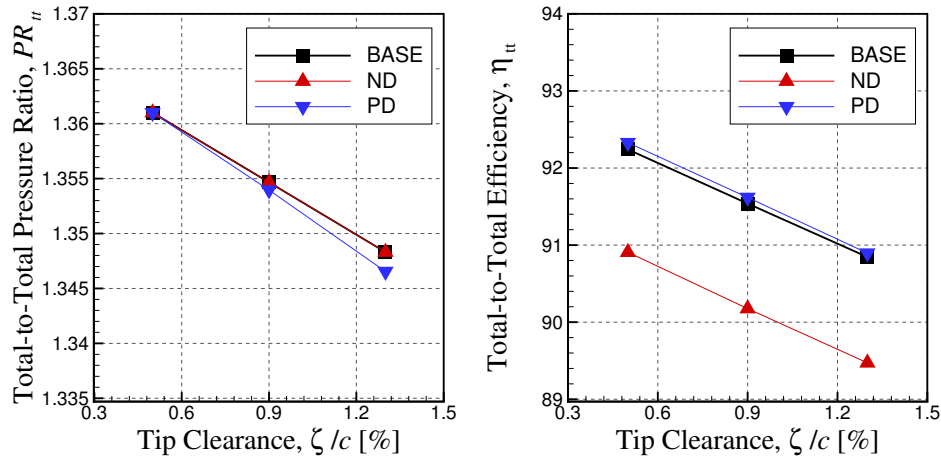
Figure 3.30: General sensitivity study for different dihedrals

The results for the detailed sensitivity study are shown in Figure 3.31. The tip blockage and tip loss curves supported the fact that that neither PD nor ND had a noticeable effect on tip blockage sensitivity or tip loss sensitivity to tip clearance. Additionally, interface position of ND was increased (expected higher stall margin) and its slope with tip clearance was slightly reduced which should translate to lower stall margin sensitivity to tip clearance.
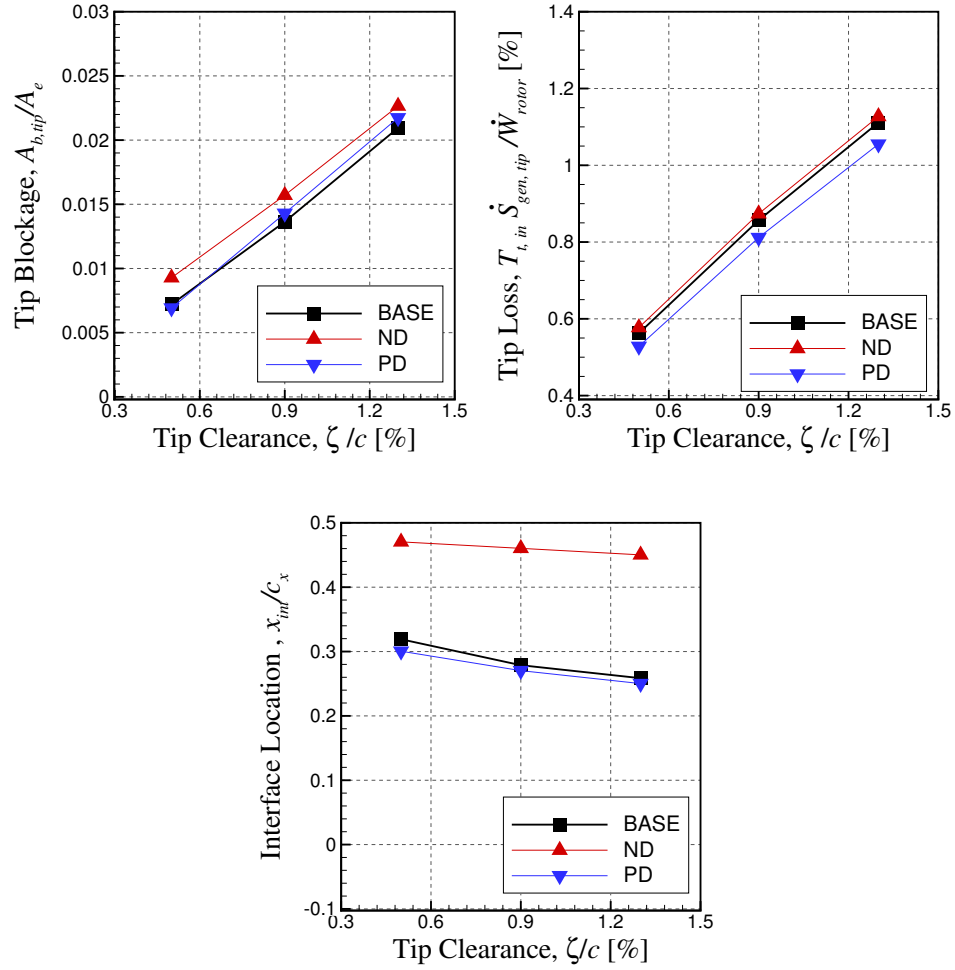
Figure 3.31: Detailed sensitivity study for different dihedrals

3.2.3 Summary

The preliminary study on the PWC rotor showed that both tip blockage and tip loss were sensitive to tip clearance. Thus, the hypothesis that tip blockage was the most sensitive parameter was proven wrong. Moreover, the corollaries, which suggest that shifting load to rear and obstructing the tip leakage flow path were the mechanisms necessary for desensitization, were also refuted. The reasons are listed below:

- The blades which only shifted load aft, namely rear cambered and forward axial swept blades, did not desensitize the performance, even the former deteriorated the sensitivity and the latter only reduced efficiency sensitivity to tip clearance.
- The forward leaned blade and the negative dihedral, which had both mechanisms, showed very slight effects on performance sensitivity to tip clearance.
- The forward loaded blades were expected to increase sensitivity to tip clearance, however,

some, such as forward cambered, backward axial swept and aft chordwise swept blades, reduced either pressure ratio or efficiency sensitivity to tip clearance.

The best geometry variation found in this Phase was the forward chordwise swept blade, which reduced the efficiency sensitivity and had the lowest pressure ratio sensitivity to tip clearance. The slope of incoming/tip clearance flow interface slope versus tip clearance size indicated reduced stall margin sensitivity.

3.3 Phase 3: Identification, Validation and Explanation of Desensitizing Flow Features

Having refuted the initial hypothesis and corollaries of desensitization based mainly on rearward chordwise load shift as associated desensitizing mechanisms (Section 1.4.2), the database from the design variation in Section 3.2.2 was analyzed to identify desensitizing flow feature(s). This is followed by validation and explanation through computational and analytical experiments.

3.3.1 Identification and Validation of Desensitizing Flow Features

To identify the flow features that are associated with performance and stability desensitization, the rotor design variations in Section 3.2.2 were regrouped according to performance sensitivity to tip clearance. The lower sensitivity group consisted of FC, FAS, BAS, FCS and ACS and the higher or unchanged sensitivity group consisted of RC, FL, BL, PD and ND. The clues in literature and the careful analysis of the flow field associated to the different design variations showed that two potential desensitization flow features were associated with the more successful designs, in terms of reduced performance sensitivity: reduced double leakage flow and high meridional momentum in the tip region.

The first desensitizing flow feature observed was the removal or reduction of double leakage. Double leakage flow is formed by the tip leakage flow that reaches the adjacent blade pressure side and extends to the adjacent tip clearance. Khalsa (1996) was the first to mention this phenomenon in tip blockage calculation followed by Sirakov and Tan (2002) who discussed double leakage in the context of the unsteady effects of stator wakes on a rotor. Since double leakage occurs when tip clearance flow is strong, it can be reduced or removed by decreasing tip loading or increasing blade pitch. McNulty *et al*. (2004) is the only work to infer double leakage reduction in a desensitization study with analyzing reversed flows at mid-tip clearance area, but that study failed to provide any validation or explanation.

The second desensitizing flow feature concluded was higher incoming meridional momentum in the blade tip region. The obvious effect would be decreasing the flow angle of tip clearance flow.

While Takata and Tsukuda (1977) and McNulty *et al.* (2004) mentioned that having higher axial or meridional momentum may have a favourable effect on stability and performance sensitivity to tip clearance, they neither validated nor explained this statement.

Tables 3.6 and 3.7 summarize the observations on double leakage ($\dot{m}_{d.l.}$) and incoming meridional momentum in tip region ($\dot{m}V_m$) values at the tip, for the lower and higher sensitivity group, respectively. The first column in both tables, double leakage, is non-dimensionalized by total tip leakage flow ($\dot{m}_{t.l.}$). The second column in both tables, incoming meridional momentum in tip region, is non-dimensionalized by mass flow ($\dot{m}$) and rotational velocity at tip (U_{tip}), which gives velocity ratio of meridional velocity to rotational velocity at tip (V_m / U_{tip}). The last two columns in both tables, show the change in pressure ratio sensitivity ($\Delta(\mathrm{d}PR/\mathrm{d}\zeta)$) and efficiency sensitivity to tip clearance ($\Delta(\mathrm{d}\eta/\mathrm{d}\zeta)$ with respect to the BASE rotor. For each design variation, performance sensitivity slopes were first calculated by dividing the difference of performance parameters of minimum and maximum tip clearance to the total tip clearance change. Then, for each blade feature the difference of performance sensitivity slope and respective sensitivity slope of BASE was divided to respective sensitivity slope of BASE. Therefore, the positive values show the increase in the performance sensitivity to tip clearance and the negative values show the reduction.

Table 3.6: Double leakage and incoming meridional momentum at tip for lower sensitivity blades at nominal tip clearance

Blade	$\dot{m}_{d.l.}/\dot{m}_{t.l.}$ [%]	V_m / U_{tip}	$\Delta(\mathrm{d}PR/\mathrm{d}\zeta)$ [%]	$\Delta(\mathrm{d}\eta/\mathrm{d}\zeta)$ [%]
BASE	7	0.447	-	-
FC	7	0.465	-15	-13
FAS	0	0.427	+1	-13
BAS	5	0.495	-15	+0.5
FCS	1	0.457	-16	-11
ACS	6	0.451	+15	-17

Table 3.7: Double leakage and incoming meridional momentum at tip for higher sensitivity blades at nominal tip clearance

Blade	$\dot{m}_{d.l.}/\dot{m}_{t.l.}$ [%]	V_m / U_{tip}	$\Delta(\mathrm{d}PR/\mathrm{d}\zeta)$ [%]	$\Delta(\mathrm{d}\eta/\mathrm{d}\zeta)$ [%]
BASE	7	0.447	-	-
RC	8	0.438	+61	+40
FL	11	0.488	-2	+4
BL	7.5	0.388	+76	+8
ND	8.2	0.483	≈ 0	+2
PD	2.5	0.430	+10	+2

In the lower sensitivity group in Table 3.6 it is clearly observed that lower sensitivity to tip clearance is linked to favourable flow features of reduced double leakage and/or increased incoming meridional momentum in the tip region. For example FC, which increased only the meridional momentum in the tip region, reduced performance sensitivity to tip clearance around 14%. On the other hand BAS, FCS and ACS, which had both favourable flow features, showed a higher reduction in performance sensitivity to tip clearance (up-to 17%). One can conclude that combining reduced double leakage and increased incoming meridional momentum in the tip region reduce performance sensitivity to tip clearance further. In the higher sensitivity group (Table 3.7), it would be expected to observe undesired flow features, such as increased double leakage and/or reduced incoming meridional momentum at the tip. RC and BL rotor, which had highest performance sensitivity to tip clearance increase (around 50%), showed both of these undesired flow features.

Some blades that showed favourable and undesired flow features together are also observed in Tables 3.6 and 3.7, such as FL, FAS, PD and ND. The answer relies in cancelling effects of double leakage and meridional momentum. Referring to Tables 3.6 and 3.7, double leakage rates and meridional momentum values can be checked. FAS had a little less meridional momentum than BASE blade, still it has lower performance sensitivity to tip clearance than BASE, since it had lower double leakage rate. Moreover, FL and PD had the highest meridional momentum near the blade tip, yet they had almost the same performance sensitivity as the BASE rotor, since they increased double leakage rate. Similar to FAS, ND has lower meridional momentum near the blade tip and low double leakage rate, and it had similar sensitivity to tip clearance with the BASE rotor. FC and BAS had higher meridional momentum than FCS, yet higher double leakage than FCS. Therefore, FC and BAS were not as good as FCS in terms of desensitization to tip clearance.

Validation of Flow Features

A computational experiment was carried out to validate the desensitization effects of high incoming meridional momentum. An inlet profile with high incoming total pressure near the shroud and low total pressure near the hub was given to a radially stacked blade, based on the BASE design, to increase meridional momentum in the blade tip region. The average inlet total pressure was kept the same. However, were the BASE rotor unchanged, a higher inlet velocity would lower tip loading and prejudice any desensitization effect. Thus, the BASE rotor's flow turning and stagger angles were modified to maintain the same spanwise loading distribution and corrected mass flow with the new inlet total pressure profile. This new blade was called *high meridional momentum at tip* (HMMT). In addition, an oppositely skewed total pressure profile was given to verify the counter effects, which is called *low meridional momentum at tip* (LMMT). At first, only a modest change on inlet total pressure profile was implemented. Subsequently, a more significant change was made on the total pressure of tip part to force additional meridional momentum to the blade

tip to accentuate the desensitization effect, which was called *very high meridional momentum at tip* (VHMMT). The inlet total pressure profiles are plotted in Figure 3.32(a); the resulting spanwise loading and the resulting spanwise meridional momentum distributions at leading edge plane are given in figures 3.32(b) and 3.32(c), respectively.

(a) Total pressure profiles (b) Spanwise loading distribution (c) Incoming meridional momentums
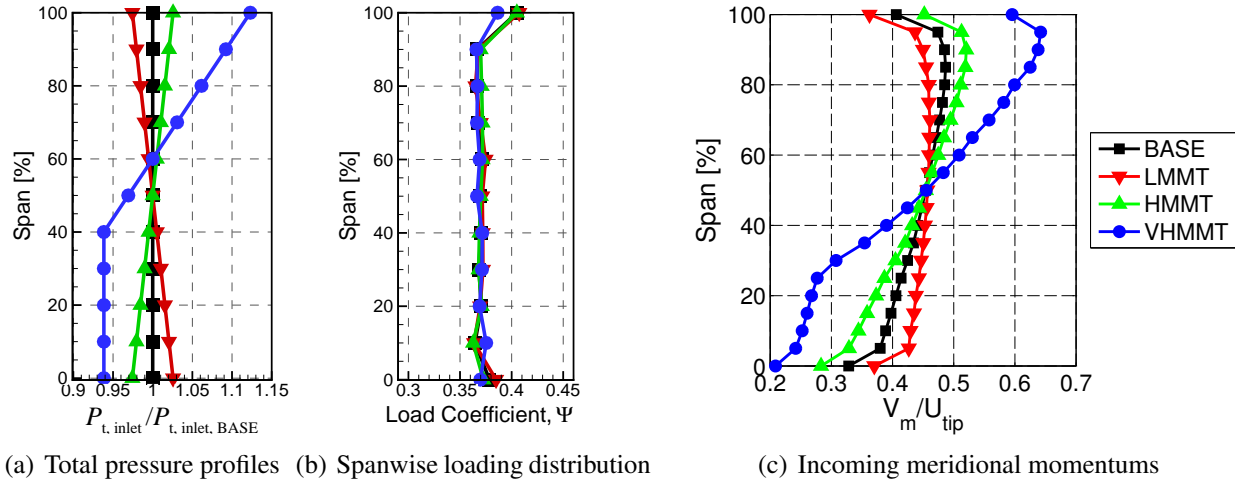
Figure 3.32: Inlet total pressure profiles for spanwise meridional momentum profiles and resulting incoming meridional momentums at leading edge plane and spanwise loading at 3.04 kg/s corrected mass flow

The nominal performance (at 0.4% chord tip clearance) of LMMT, HMMT, VHMMT are compared with the BASE design in Table 3.8. As observed, all design variations (except VHMMT) had same total pressure ratio and design corrected mass flow rate. VHMMT has slightly lower design corrected mass flow rate than the other blades. However to be consistent with the other three blades, all sensitivity studies were performed at the corrected mass flow of 3.04 kg/s.

Table 3.8: Influence of meridional momentum change on nominal performance

Property	BASE	LMMT	HMMT	VHMMT
Corrected Design Mass Flow Rate	3.04 kg/s	3.04 kg/s	3.04 kg/s	2.97 kg/s
Total-to-Total Pressure Ratio (@ $\dot{m}_c$=3.04 kg/s)	1.361	1.361	1.361	1.361
Total-to-Total Efficiency (@ $\dot{m}_c$=3.04 kg/s)	92.24%	92.00%	92.55%	92.65%

The general sensitivity to tip clearance of LMMT, HMMT and VHMMT is plotted in Figure 3.33 with respect to the BASE blade. As expected, for HMMT, the sensitivity of pressure ratio to tip clearance was reduced and there was a small reduction in the efficiency sensitivity to tip clearance, whereas LMMT showed an increase in sensitivity to tip clearance. Additionally, VHMMT had

very strong desensitizing effect in pressure ratio (62.2% reduction in slope versus the BASE), and a weaker desensitizing effect in efficiency (31.9% reduction in slope versus the BASE). Figure 3.33 also indicates that VHMMT increased the stall margin and reduced its sensitivity by 72.3%. The speedlines of VHMMT are given in Appendix E.2. As explained in previous section, sensitivity slopes were calculated from ratio of difference of value at minimum and at maximum tip clearance to total tip clearance size change.

Figure 3.33: General sensitivity of different spanwise meridional momentum profiles at corrected design mass flow of BASE design

Next, the corresponding detailed sensitivity are plotted in Figure 3.34. As expected, the slopes of tip blockage of HMMT and VHMMT were reduced while the opposite effect was observed for LMMT. There was an increase in the nominal (minimum tip clearance) tip loss for HMMT and VHMMT, but the slope of the tip loss was decreased in both cases. The interface positions of high meridional momentum blades HMMT and VHMMT were further downstream (higher stall margin) and their sensitivity to tip clearance was decreased, thus confirming the reduced sensitivity of stall
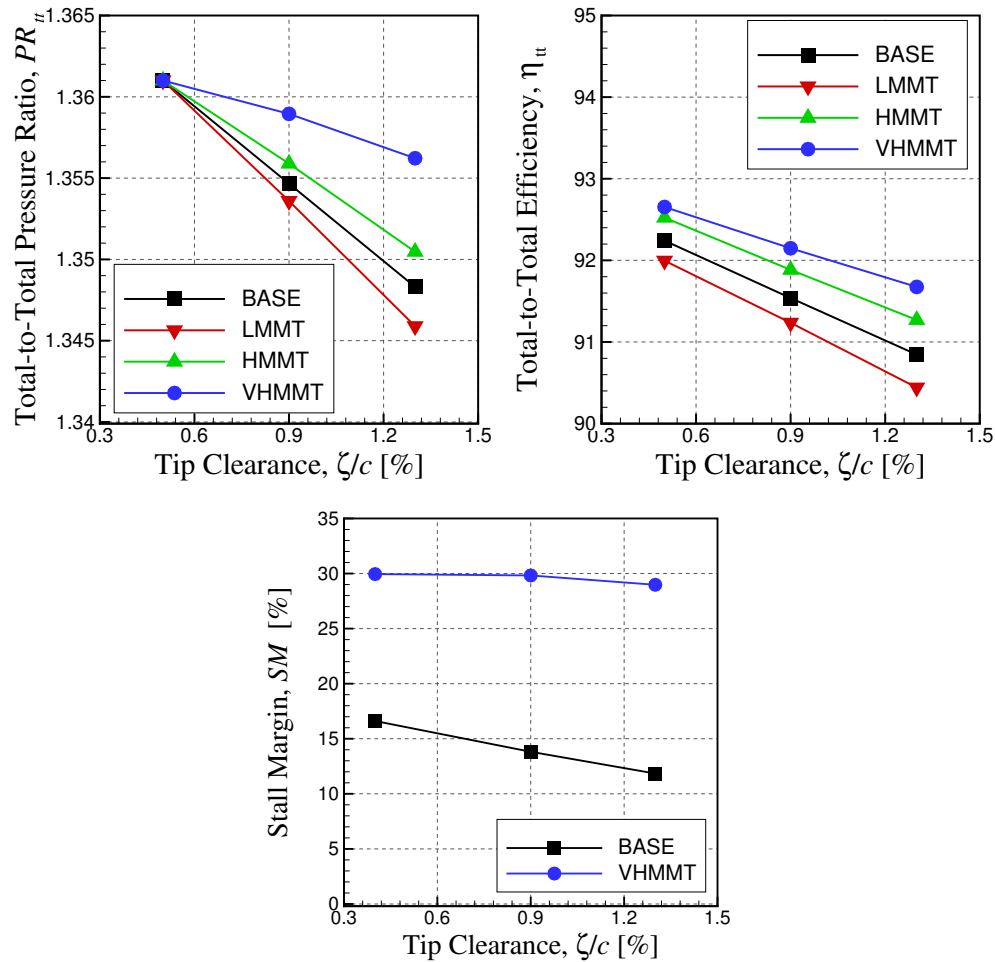
margin to tip clearance for the VHMMT rotor as shown in Figure 3.33.
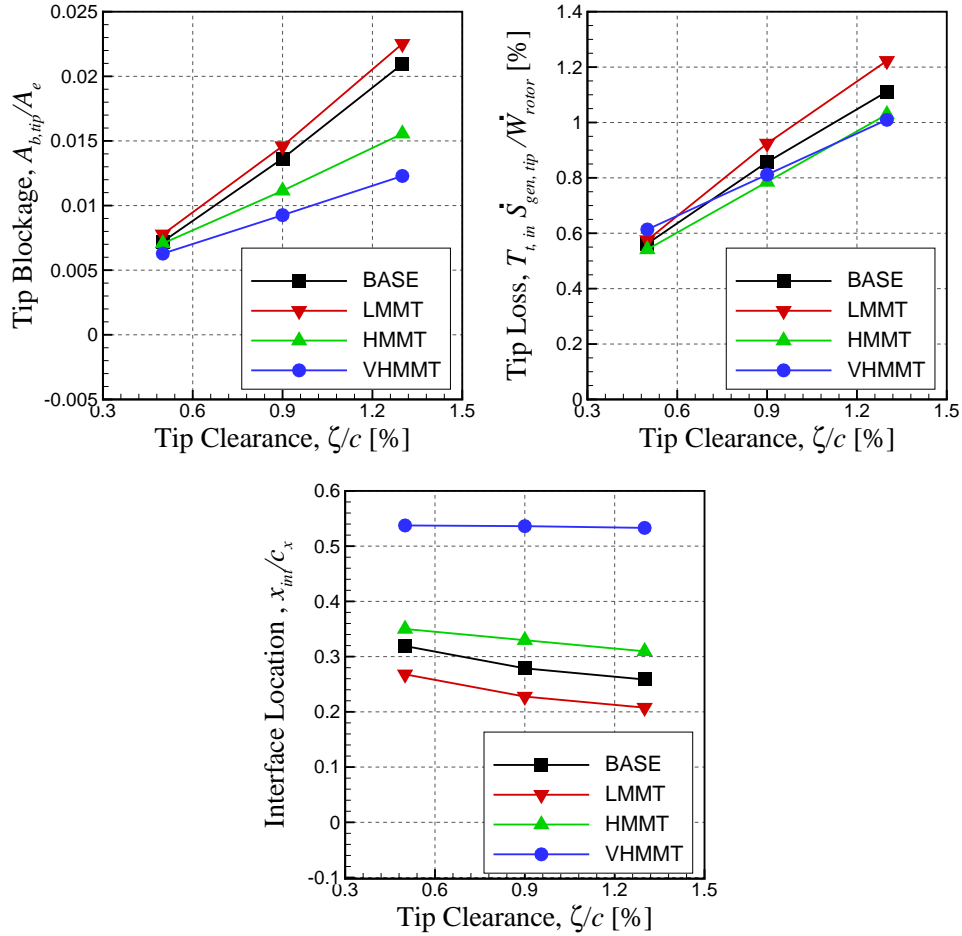
Figure 3.34: Detailed sensitivity of different spanwise meridional momentum profiles at corrected design mass flow of BASE design

To visualize the effect on the flow, Figure 3.35 plots the streamlines of the flow emanating from the tip clearance for these three designs at all three simulated tip clearance sizes. The increase in incoming tip meridional momentum pushed the tip clearance flow region downstream and toward the suction side and prevented its growth with tip clearance size toward the pressure side, especially in the case of the VHMMT design where it does not even reach the pressure side. In this case, since the tip clearance fluid did not *double leak* into the adjacent blade tip clearance, ensuring that tip clearance flow, coming only from suctioned core flow, had higher streamwise velocity as shown in Figure 3.36 by the chordwise streamwise velocity distribution in Figure 3.36(a) and its change from minimum to maximum tip clearance in Figure 3.36(b). Figure 3.36(a) indicates that overall chord the meridional momentum was increased by both blades. While the increased meridional momentum did initially increases mixing losses with the tip clearance flow, as evidenced by higher
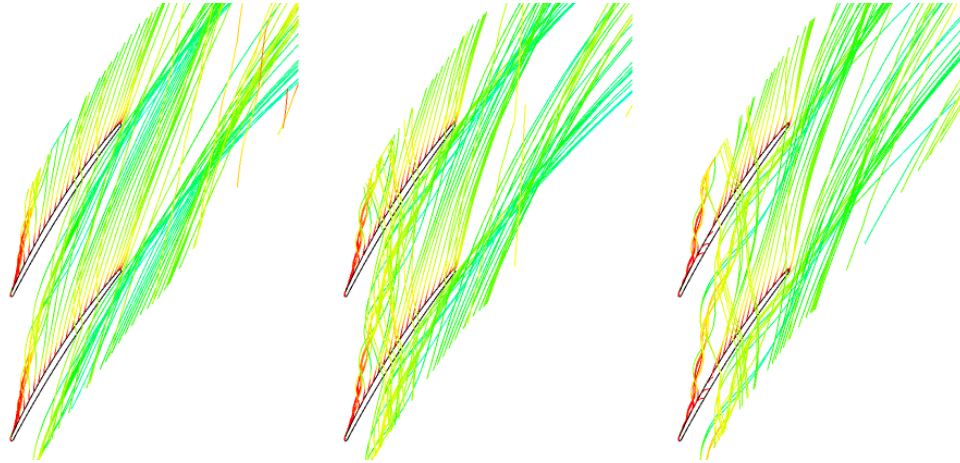
(a) BASE (from left to right ζ=0.4%, 0.9% and 1.3% chord)
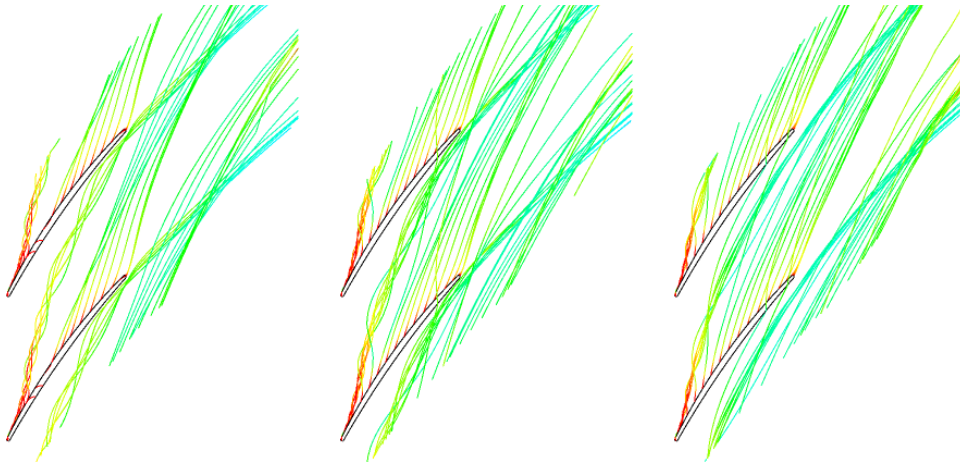
(b) HMMT (from left to right ζ=0.4%, 0.9% and 1.3% chord)
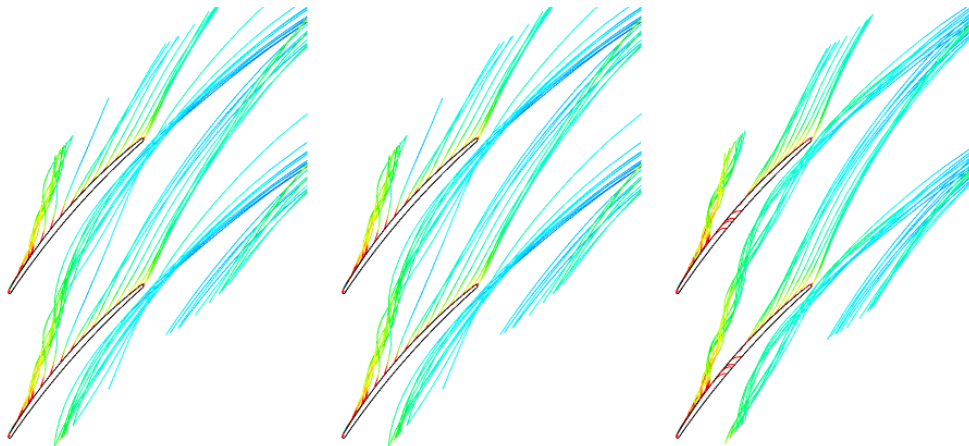
(c) VHMMT (from left to right ζ=0.4%, 0.9% and 1.3% chord)

Figure 3.35: Tip clearance flow streamlines for VHMMT, HMMT and BASE at corrected design mass flow of BASE design

tip losses for the HMMT and VHMMT versus the BASE rotor at minimum tip clearance, shown in Figure 3.34, removal of double leakage reduced the loss for VHMMT at higher tip clearance. Moreover, Figure 3.36(b) clearly shows the increase in the change of streamwise velocity due to tip clearance size increases for VHMMT. This change occurred between 0.3 to 0.7 chord, where the double leakage flow was mostly effective (Sirakov and Tan, 2002), thus, this change could lead to the elimination of the double leakage.

(a) Streamwise tip clearance flow

(b) Change of streamwise tip clearance flow
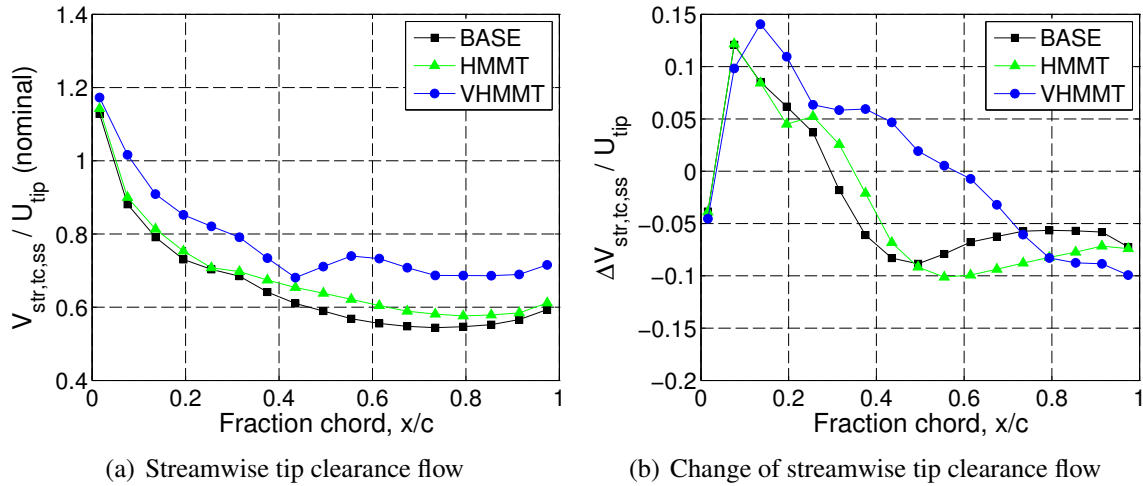
Figure 3.36: Streamwise tip clearance flow and its change from minimum to maximum tip clearance (mass-averaged-over-tip-clearance) at exit of tip clearance on blade suction side for the rotor designs in Figure 3.35

A numerical experiment was carried out to assess the effect of tip clearance double leakage on compressor rotor performance sensitivity to tip clearance using the design VHMMT, since it had no double leakage even at the highest tip clearance. The circumferential pitch size was incrementally reduced from 8° to 5.8°, by increasing number of blades from 45 to 62 blades. The five pitch sizes used were 8° (45 blades), 6.9° (52 blades), 6.6° (55 blades) and 6° (60 blades) and 5.8° (62 blades). To quantify the magnitude of double leakage, its mass flow rate was calculated. The calculation of double leakage mass flow rate is explained and speedlines of five test pitches are given in Appendix F.

Figure 3.37 plots double leakage mass flow rate, as non-dimensionalized by tip clearance mass flow rate, versus tip clearance for different pitch sizes (45, 52, 55, 60, 62 blades) at their design corrected mass flow rate. The figure shows that double leakage was completely absent for 45-blade design and started to appear at 52-blade design at the highest tip clearance. The general sensitivity study results for the five pitch sizes are shown in Figure 3.38. Moreover, for higher pitch sizes, such as 55, 60 and 62 blades, the slope of double leakage between medium to high tip clearance is

Figure 3.37: Double leakage proportion versus tip clearance at their design corrected mass flow rate for VHMMT design at different pitch sizes
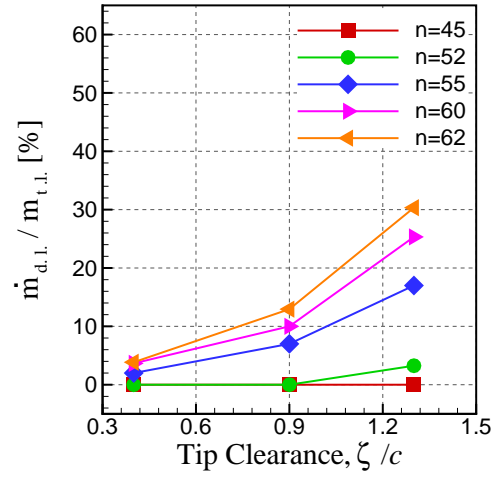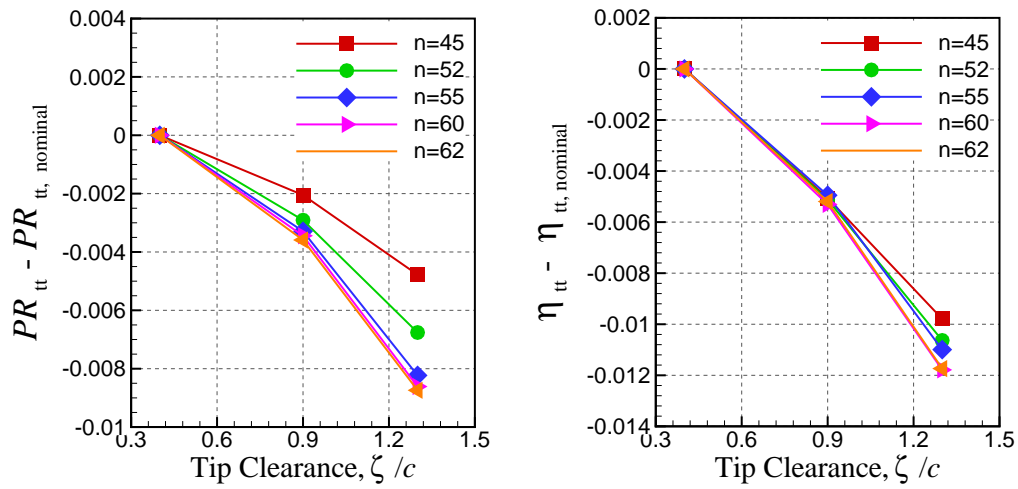

Figure 3.38: General sensitivity results at their design corrected mass flow rate for VHMMT design at different pitch sizes

higher than minimum to medium clearance slope, which showed that both double leakage and its rate were sensitive to tip clearance. Figure 3.39 combines the data of figures 3.38 and 3.37 by plotting the change in total-to-total pressure rise and efficiency between minimum and maximum tip clearance, versus double leakage flow at maximum tip clearance. Figure 3.39 shows a clear correlation between double leakage flow rate and pressure rise sensitivity to tip clearance size, with a significant reduction in this sensitivity as double leakage goes to zero. The same trend also applies to efficiency sensitivity to tip clearance size.
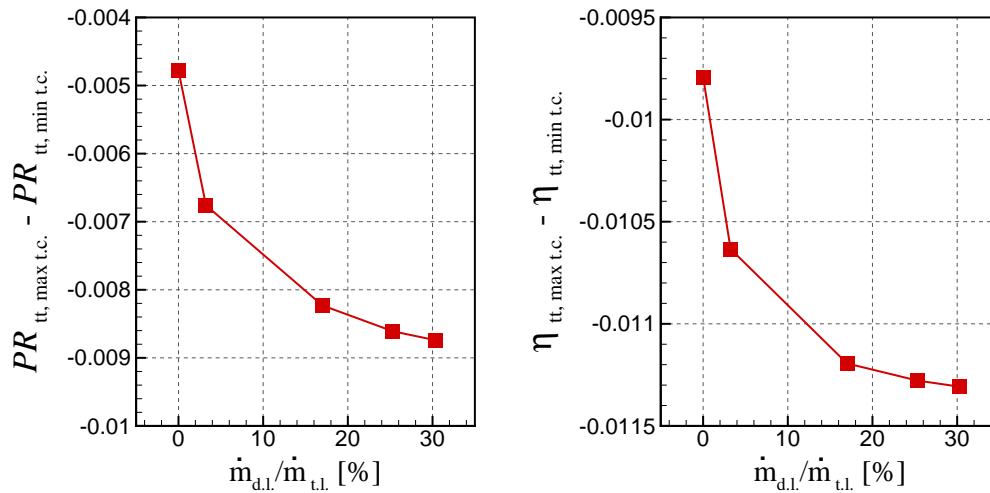
Figure 3.39: Sensitivity of total pressure ratio and efficiency (between minimum and maximum tip clearance) versus double leakage proportion at their design corrected mass flow rate for VHMMT design at different pitch sizes

3.3.2 Mechanisms Associated with Desensitization

This section explains the flow physics associated with desensitization through reduction or removal of double leakage and high meridional momentum at the blade tip.

Double Tip Leakage

Storer and Cumpsty (1991) decomposed the tip clearance flow velocity vector into normal and tangential components to the local blade camber line to explain formation tip clearance flow. The normal component is essentially an inviscid flow driven by the local pressure difference between the pressure and suction side (i.e. local blade loading) whereas as the streamwise component is that of the flow entering the tip clearance on the pressure side. Figure 3.40(a) plots the absence of double leakage, where this streamwise tip clearance flow velocity component is that of the local core flow on the tip region pressure side. Figure 3.40(b) plots the presence of double leakage,

where the streamwise tip clearance flow velocity component of double leaked flow becomes less than the local core flow on the tip region pressure side, since the initial leaked flow experiences tip mixing loss and tip blockage in the adjacent rotor passage. This is illustrated in Figure 3.40 which depicts the flow vectors at the blade tip of a blade tip radial cut. The flow vectors of flow leaking through a single tip clearance are colored black and those associated with fluid that have gone through two adjacent tip clearances are colored red and labeled as DL.

(a) Absence of double leakage flow
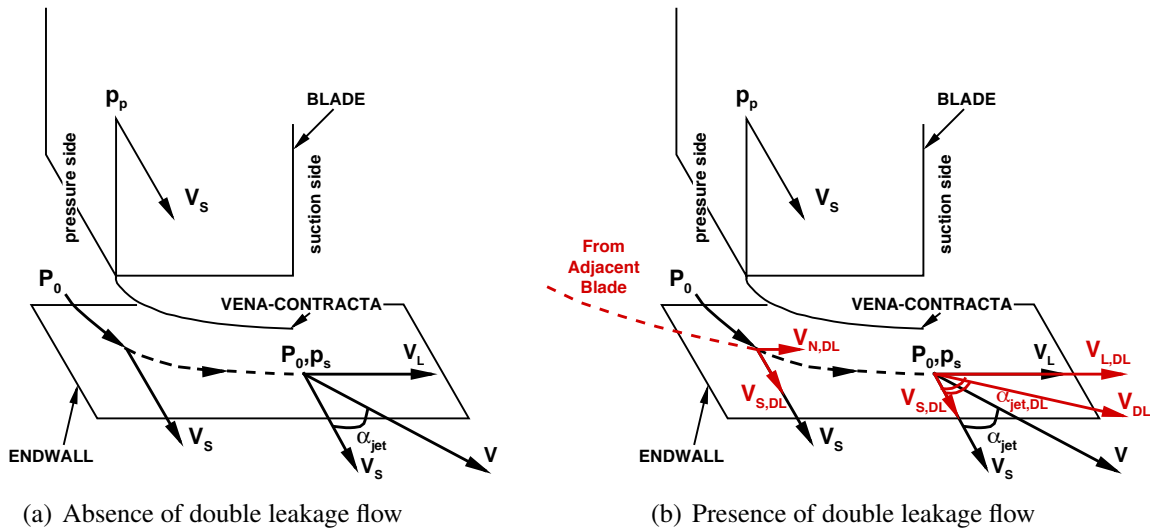
(b) Presence of double leakage flow

Figure 3.40: Radial cut of blade with blade tip velocities in absence and existence of double leakage flow (modified from Storer and Cumpsty (1991))

When double leakage occurred, some of the fluid entering the tip clearance on the pressure side comes from the adjacent blade tip clearance. This double leaking fluid had very low streamwise velocity, which resulted in increased leakage jet exit angle and flow vector difference and thus higher mixing loss and tip blockage. As the tip clearance increased, the amount of double leakage naturally increased, as shown in Figure 3.37, making the leakage jet angle and flow vector difference even greater and augmenting the mixing loss and tip blockage beyond what they would had been only an increase in tip clearance flow but at the same leakage jet exit angle as at lower tip clearance (as would be the case when double tip leakage is absent). Furthermore, it should be noted that the increase in leakage jet exit angle strengthened the tip clearance flow and led to even more double leakage than what would be encountered due to the geometric increase in tip clearance alone, which explains the increase in sensitivity with tip clearance in Figure 3.37 for cases with double leakage.

Double leakage increased in both spanwise direction and streamwise direction. Figure 3.41 illustrates the increase of double leakage proportion in spanwise direction. Similar to Figure 3.37, Figure 3.41 (b) shows the increase of double leakage proportion with tip clearance increase of BASE rotor. Moreover, Figure 3.42 illustrates the increase of double leakage proportion in stream-

wise direction. The streamlines at blade tip of BASE rotor clearly shows increase of double leaking fluid when tip clearance is increased.
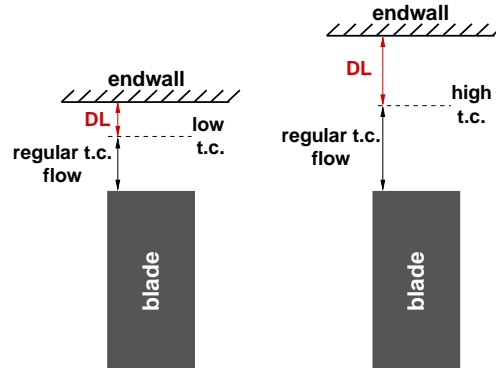
(a) Schematic of double leakage increase in spanwise direction
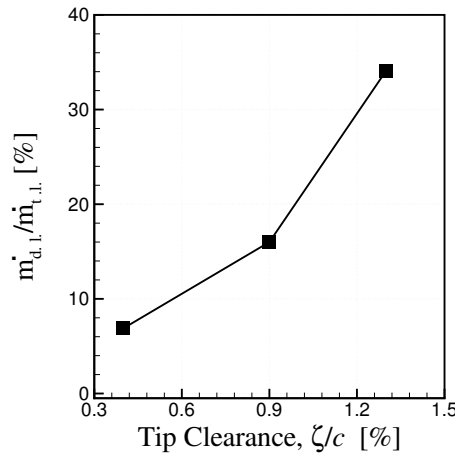
(b) BASE rotor double leakage proportion vs. tip clearance

Figure 3.41: Spanwise increase of double leakage proportion due to tip clearance increase

The above mechanism is evidenced in Figure 3.43 which plots the nominal and change between minimum and maximum tip clearance in the streamwise and normal velocity components of tip clearance flow on blade suction side for VHMMT design for three different pitch sizes (i.e. number of blades), with double leakage absent only for the 45-blade design. As observed from the figure, increasing number of blades, which is a direct way to increase double leakage, increased the loss of streamwise velocity, whereas change in normal velocity only shifted upstream and remained constant with increasing number of blades.

While tip loss and tip blockage determined the effects of double leakage on performance, the incoming/tip clearance flow interface position can be analyzed for the effects of double leakage on stability as suggested by Vo *et al.* (2008) and other authors. The interface position is determined by a momentum balance between tip clearance flow and incoming flow. Thus, lower streamwise

(a) Schematic of double leakage increase in streamwise direction

(b) BASE rotor streamlines at the blade tip
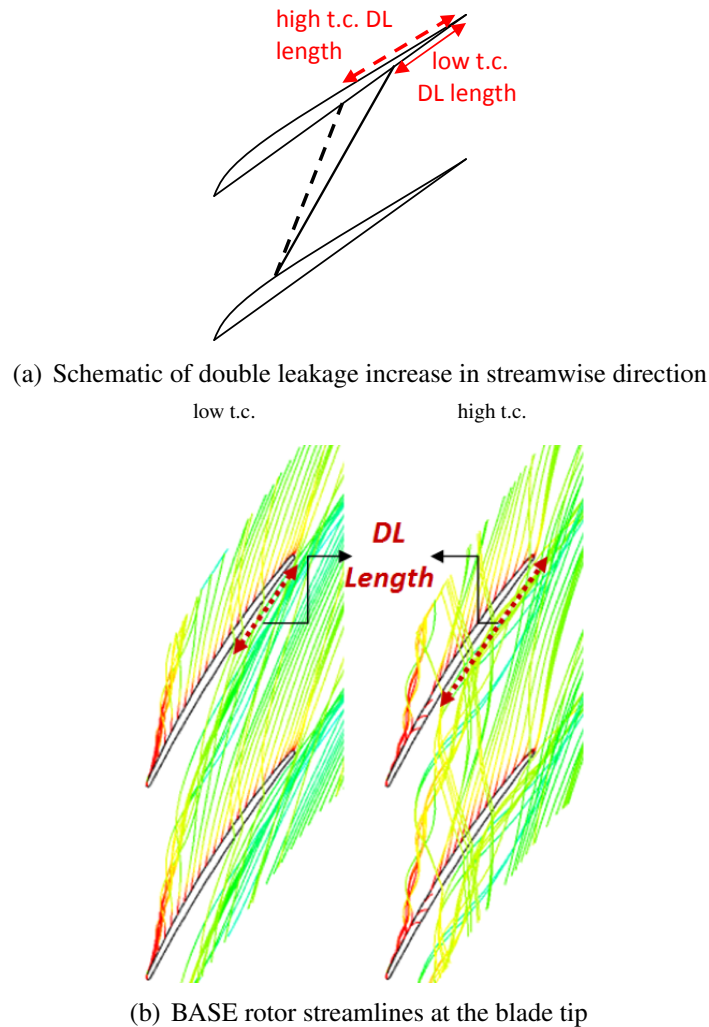
Figure 3.42: Streamwise increase of double leakage proportion due to tip clearance increase

velocity component in the tip clearance flow would move the interface position upstream putting the interface position closer to the leading edge plane and thus reducing nominal stall margin. Were the double leakage proportion constant with increasing tip clearance, the momentum of the tip clearance flow relative to the incoming flow (over the span corresponding to tip clearance height) would be the same and the position of the interface would not change, meaning that double leakage would not affect stall margin sensitivity to tip clearance. However, since Figure 3.37 shows that the double leakage proportion increases as the tip clearance increases, increasing tip clearance would reduce momentum at the tip clearance flow relative to the incoming flow and would shift the interface upstream, thus reducing stall margin, thus making this component sensitive to tip clearance. The above physical explanation on the effect of double leakage on performance and stall margin also supports the fact that the sensitivity of these parameters decreases when double leakage is reduced.

(a) Streamwise tip clearance flow

(b) Normal tip clearance flow

(c) Change of streamwise tip clearance flow

(d) Change of normal tip clearance flow
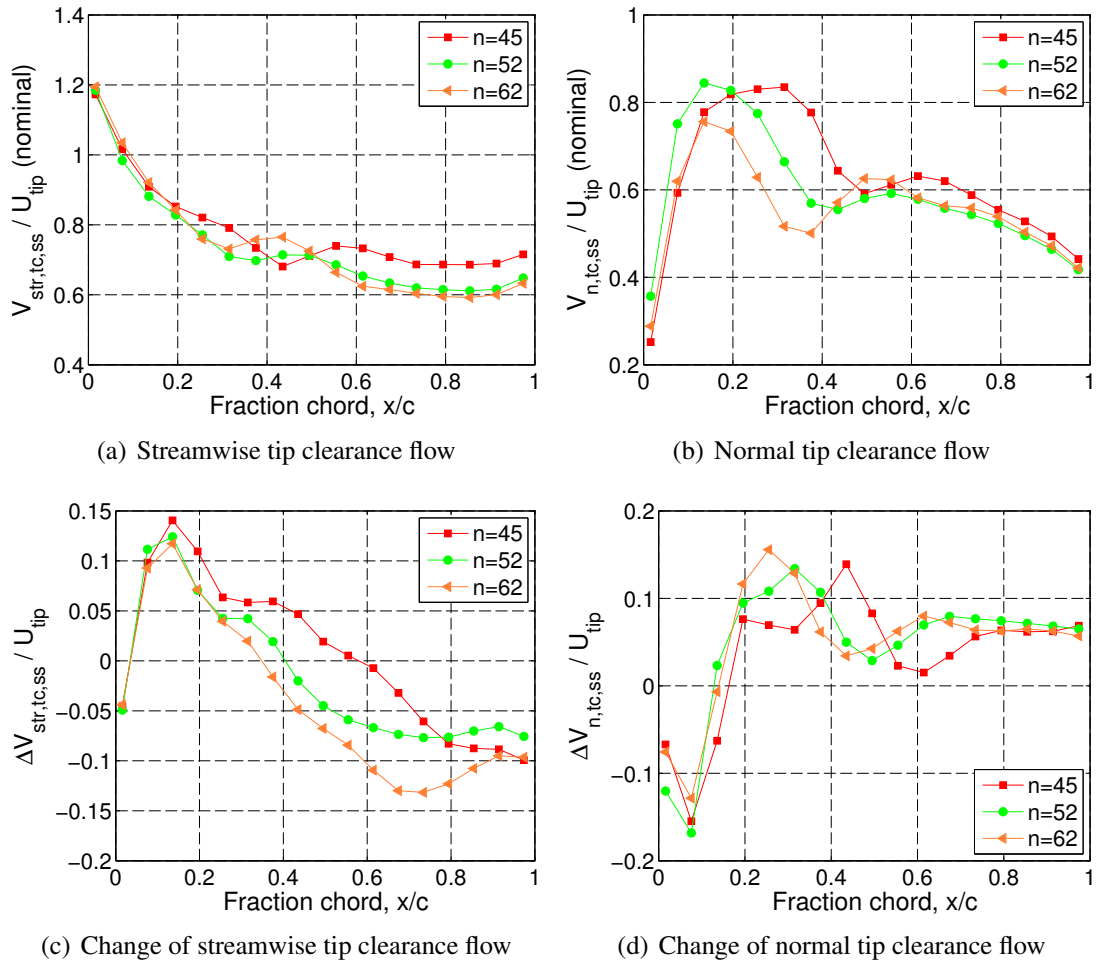
Figure 3.43: Tip clearance flow velocity components and their change between minimum and maximum tip clearance for different pitch sizes

High Incoming Momentum in the Tip Region

High incoming meridional momentum can desensitize performance and stability in two ways: The first mechanism is coupled to double leakage. Table 3.9 lists the incoming meridional momentum at the tip and double leakage rate for the blades, whose tip clearance flow streamlines are shown in Figure 3.35. Table 3.9 and Figure 3.35 clearly indicate that increasing incoming meridional momentum in the tip region reduced the double tip leakage rate. Thus, one can infer that at least part of the desensitization effect of high meridional momentum in the tip region was that it reduced or prevented double tip leakage by pushing the tip clearance flow both in the streamwise direction and toward the blade suction side.

This was performed in two ways, as illustrated in Figure 3.44, where *nominal blade case* is labeled as BASE and *high incoming meridional momentum blade case* is labeled as VH. The first

Table 3.9: Double leakage and meridional momentum at tip of blades in Figure 3.35 at nominal tip clearance

Blade	V_m / U_{tip}	$\dot{m}_{d.l.}/\dot{m}_{t.l.}[\%]$
BASE	0.447	7
HMMT	0.494	0.5
VHMMT	0.632	0

was simply from the increased momentum of the incoming flow. The other was from the fact that higher meridional momentum in the tip region means higher core velocity which implied that the tangential component of the tip clearance flow was higher which in turn reduced the leakage jet exit angle and flow vector difference between the tip clearance flow and the incoming/core flow. The above mechanism is evidenced in Figure 3.45, which illustrates increase of meridional momentum at the blade tip reduced the double leakage in HMMT rotor.
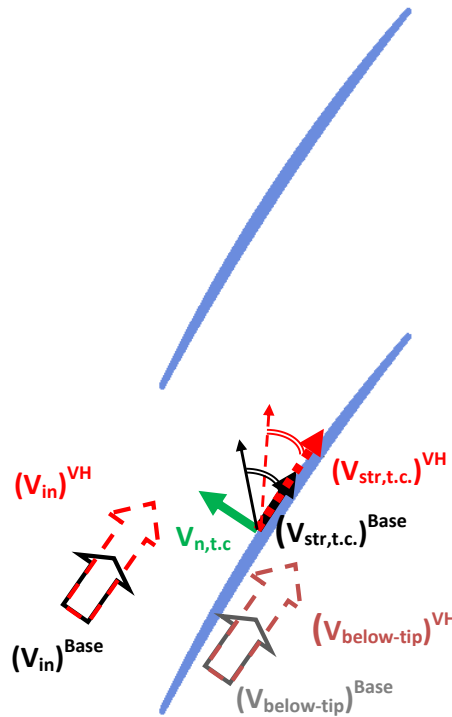
Figure 3.44: Coupled flow mechanism of both design strategies

The second desensitization mechanism associated with high meridional momentum in the tip region involved the effect of high incoming flow momentum on the generation of tip blockage, and mixing loss with tip clearance flow in the absence of double leakage. To assess this effect, an analytical experiment was carried out. The blockage model of Khalid *et al.* (1999) was used to
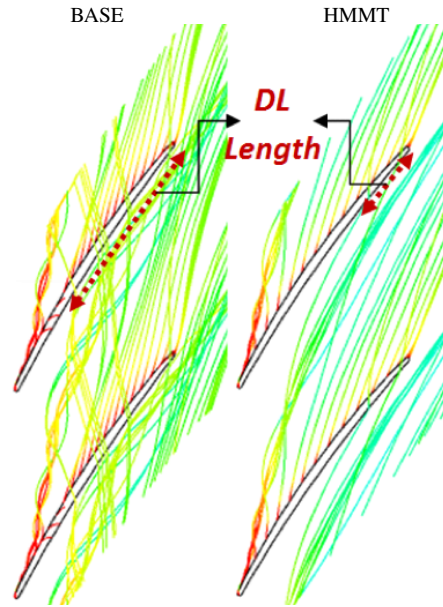
Figure 3.45: Streamlines at blade tip for blades BASE and HMMT

calculate rapidly tip blockage and mixing loss. First, the blockage and loss of the BASE rotor was calculated using this model. Subsequently, the incoming meridional momentum at blade tip in the leading edge plane is increased to calculate effects of higher meridional momentum.

As illustrated in Figure 3.46, Khalid *et al.* (1999) modelled tip blockage using a two-step approach, the first being the mixing of the incoming and tip leakage flow to form in initial velocity deficiency region followed by the growth of this blockage region as it convected up the pressure gradient towards the rotor trailing edge plane to form the final tip blockage region. A modelling assumption was that the mixing of tip clearance and incoming flows occurs at the incoming tip clearance flow interface, whose angle was set by the mixed flow direction. An additional assumption was that if the mixing point reaches the pressure side, then the mixed flow direction will be equal to the angle of the blade pressure side surface and the mixing will happen at the pressure side. Thus, this model excluded the effect of double tip leakage.

The input parameters were densities and velocities of incoming flow at the leading edge plane, densities and velocities at the tip clearance exit on the suction side and local pressures throughout blade passage in the tip clearance region. All these parameters were obtained from CFX simulation results of BASE rotor at design mass flow rate for 0.4% and 1.3% tip clearances. Incoming meridional momentum, which is non-dimensionalized by incoming mass flow rate and rotational velocity at blade tip, was calculated at the axial plane of the rotor tip leading edge and delimited by the tip clearance height and blade pitch.

First, the interface angle (i.e. mixed flow direction) was calculated from a momentum balance between the incoming and tip clearance flows. Subsequently, the viscous loss and initial tip
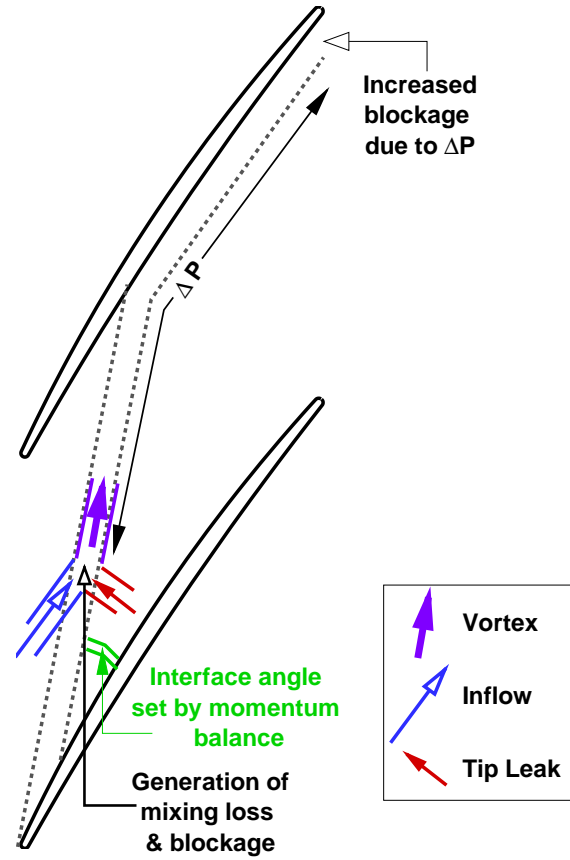
Figure 3.46: Schematic of the model by Khalid *et al.* (1999)

blockage was obtained from the mixing process and resulting streamwise velocity deficiency, respectively. Thereafter, the expansion of the initial tip blockage due to the pressure gradient was calculated and the tip blockage was updated. In the current implementation, the pressure gradient was assumed to be equal to the ratio of pressure difference of the local pressure and the exit pressure (labeled as ΔP in Figure 3.46), and the streamwise distance between local point and exit plane.

Figure 3.47 plots resulting blockage, mixing loss and interface position versus the increase in incoming meridional momentum per unit area for 0.4% and 1.3% tip clearances compared to the BASE rotor design. The sensitivity of each parameter to tip clearance can be taken as the distance between two curves. It can be observed that as the incoming meridional momentum increases, the tip blockage, mixing loss and the interface angle reduced. Most importantly, the sensitivity of these parameters to tip clearance, indicated by the difference between the 0.4% chord and 1.3% chord curves, reduced with increasing incoming tip meridional momentum. The sensitivity of tip blockage fell steadily with increasing tip clearance size. The sensitivity of mixing loss also reduced but tended toward a constant value. Whether the reality of this asymptote depends on the limit of modelling assumption, but the trend nevertheless showed reduced sensitivity to tip clearance. Since

tip blockage and mixing loss were directly related to rotor pressure rise and efficiency, this model showed that the sensitivity of rotor performance to tip clearance would reduce as in the incoming meridional momentum in the tip region increases. Last but not least, the sensitivity of interface angle reduced to zero, indicated by converging curves on last plot of Figure 3.47. Knowing that interface angle was directly related to stability, this model also indicated that increasing meridional momentum desensitizes stall margin to tip clearance.

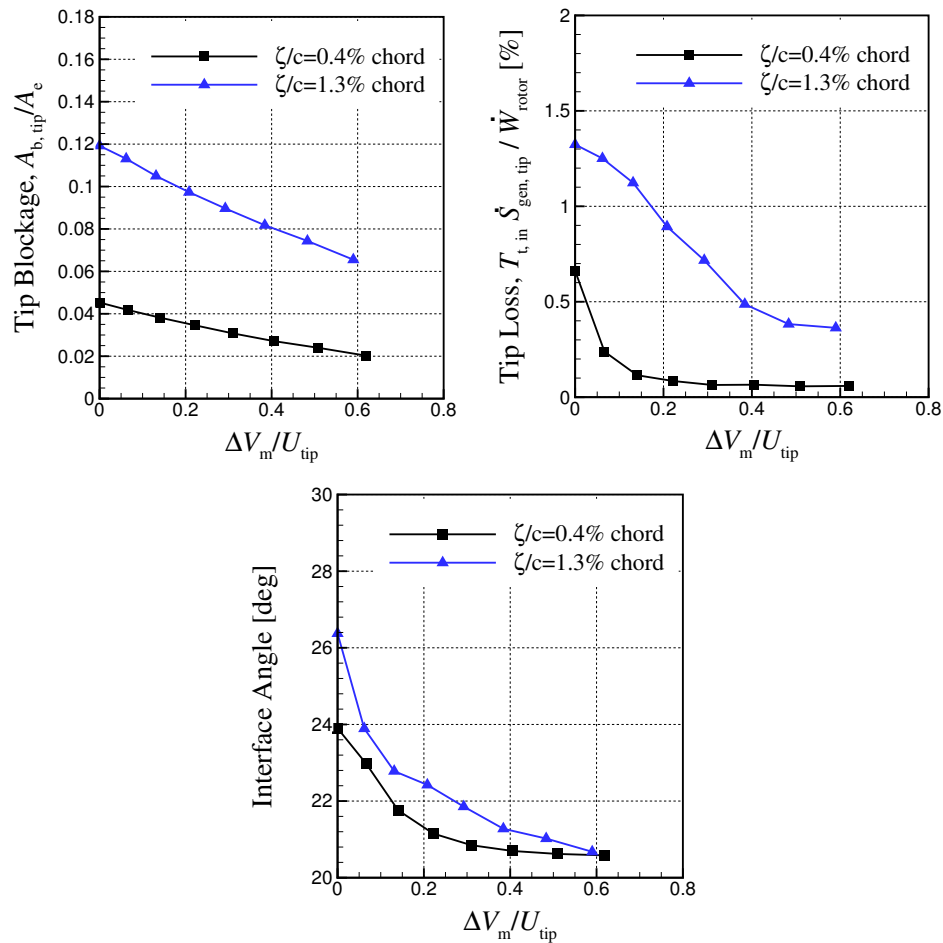Figure 3.47: Blockage, mixing loss and interface angle change due to meridional momentum increase as estimated using model of Khalid *et al.* (1999)

3.4 Phase 4: Blade Design Characteristics to Exploit Desensitizing Flow Features

With the identification and understanding of the two desensitizing flow features, it can be inferred that the sensitivity of performance and stability to tip clearance for an axial compressor rotor

design can be reduced if it incorporates either or both of these features. In this section the experience gathered with the design variations in section 4.2 is used to recommend two blade designs that incorporates these flow features for desensitization. It is noted that the purpose of this section is not to optimize any design but rather to simply show examples of rotor designs that incorporate these desensitizing flow features from successful reduction of sensitivity to tip clearance.

3.4.1   Full Forward Chordwise Swept Rotor

In Section 3.2.2, FCS was found to have the lowest pressure ratio and stability sensitivity and ACS had the lowest efficiency sensitivity. Table 3.6 showed that both blades had higher meridional momentum in the tip region and lower double leakage with FCS being the lower of the two.

Full forward chordwise sweep (FFCS) is proposed to combine the beneficial features of ACS and FCS, such that it would have higher meridional momentum at blade tip. FCS had moderate-high meridional momentum in the tip region and it had low double leakage rate. ACS had moderate-high meridional momentum in the tip region and it had moderate double leakage rate. The upper half of FCS and lower half ACS are proposed to be combined to achieve a a blade even less sensitive to tip clearance.

The FFCS rotor was iterated to have the same spanwise loading distribution as the BASE rotor. Figure 3.48 shows the resulting geometry of a 20° FFCS design versus BASE design. Figure 3.49 shows that spanwise loading of the final FFCS design iteration is similar to that of BASE rotor with differences lying within 0.03.

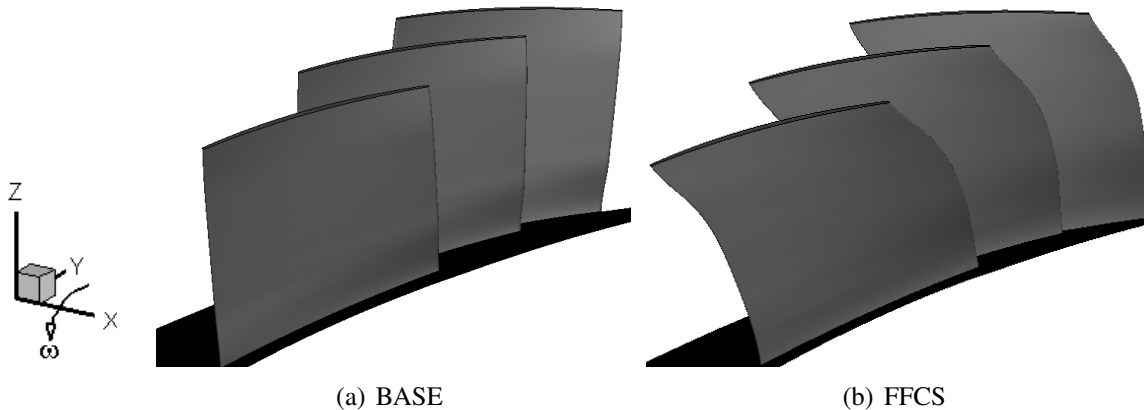(a) BASE   (b) FFCS

Figure 3.48: 3D view of BASE and FFCS designs

The nominal (minimum tip clearance) performance and stall margin for the FFCS and BASE rotors are listed in Table 3.10 demonstrating that nominal total pressure ratio is consistent. Additionally, nominal peak efficiency and nominal stall margin were increased in the case of FFCS
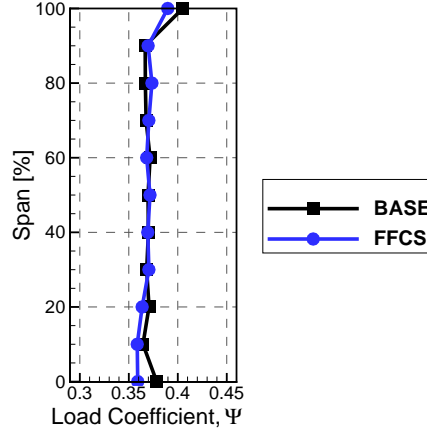
Figure 3.49: Spanwise loading distribution of FFCS

design. It is noted that the nominal performance and stall margin were checked at 3.04 kg/s corrected mass flow rate which was the design corrected mass flow rate for almost all of the studied rotors, since the design corrected mass flow of FFCS design was slightly higher than that of the BASE rotor.

Table 3.10: Nominal performance of FFCS versus BASE

Property	BASE	FFCS
Corrected Design Mass Flow Rate	3.04 kg/s	3.10 kg/s
Total-to-Total Pressure Ratio (@ $\dot{m}_c$=3.04 kg/s)	1.361	1.361
Total-to-Total Efficiency (@ $\dot{m}_c$=3.04 kg/s)	92.24%	93.48%
Stall Margin	16.05%	21.50%

Before moving on to the sensitivity study, the desensitizing flow features were checked. Figure 3.50 plots the spanwise distribution of pitch-averaged meridional momentum at the leading edge plane for the FFCS versus BASE, FCS and ACS rotors. It indicates that FFCS had higher meridional momentum near tip region compared to ACS, FCS and BASE. This proved that the combination of FCS and ACS worked well in achieving the intended desensitizing flow feature of increasing incoming meridional momentum in the tip region. This increase can be explained with Figure 3.51, which plots the pitch-averaged pressure in the meridional plane for the FFCS and BASE blades. One can observe that the lower static pressure region for the FFCS rotor was at the leading edge near the tip, which should induce more flow toward the tip region.

The FFCS design also reduces double leakage. Figure 3.52 plots the change in double leakage proportion of tip clearance flow for FFCS versus its constituents FCS, ACS and the BASE blade designs. The results show that the FFCS was able to achieve the same low double leakage as the FCS design.
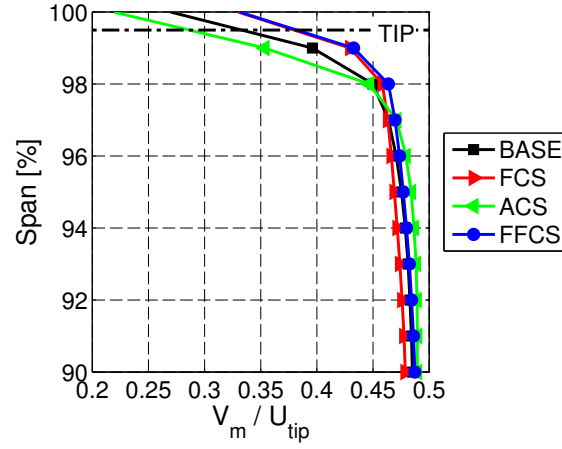
Figure 3.50: Spanwise distribution of meridional momentum per unit area for FFCS, FCS and ACS designs at the leading edge plane at design corrected mass flow rate of BASE
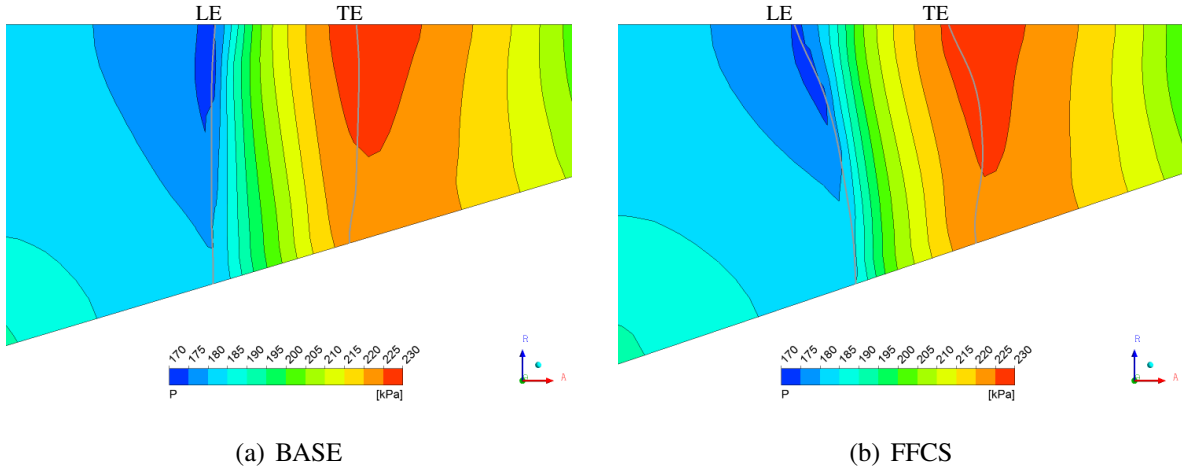

(a) BASE

(b) FFCS

Figure 3.51: The pressure field of FFCS and BASE at design corrected mass flow rate of BASE
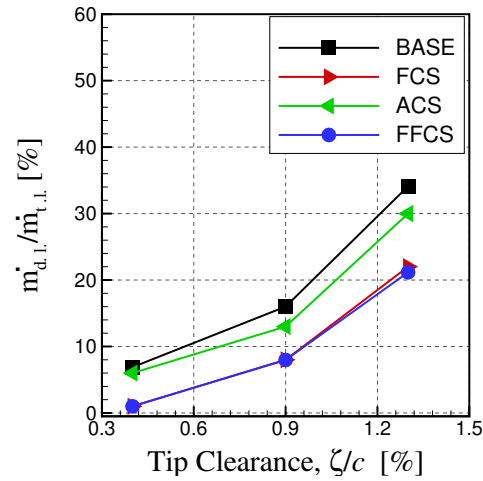

Figure 3.52: Change in double leakage proportion with tip clearance for FFCS versus FCS, ACS and BASE designs at design corrected mass flow rate of BASE

A sensitivity study is performed on FFCS next to validate the predicted lower sensitivity to tip clearance. The results of the general sensitivity study, in terms of the total pressure ratio and efficiency are shown in Figure 3.53 with the inclusion of the performance results of the FCS and ACS rotors for comparison. The figure indicates that FFCS had lower performance sensitivity than ACS, FCS and BASE blades, such that it has a reduction of 24.6% in efficiency to tip clearance sensitivity, 23.9% in total pressure ratio sensitivity to tip clearance and 90% in stall margin sensitivity to tip clearance when compared to the BASE rotor. Details of the performance and the speedlines of FFCS are given in Appendix E.3.
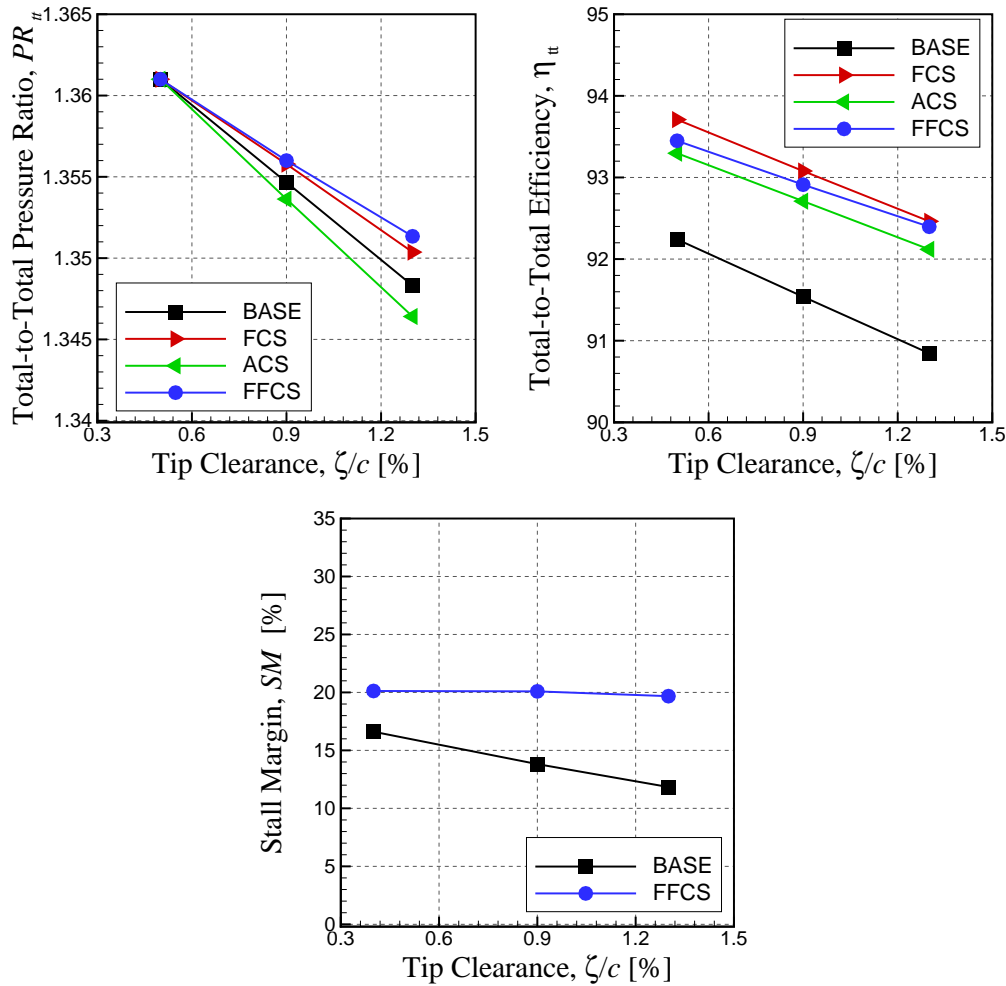
Figure 3.53: General sensitivity study for FFCS at corrected mass flow rate of 3.04 kg/s

The results for the detailed sensitivity study in terms of tip blockage, entropy generation rate (tip loss) and inflow/tip clearance flow interface position are presented in Figure 3.54. As expected, a reduction in tip blockage and tip loss was observed indicating reduced sensitivity with respect to tip clearance. Moreover, interface position was increased and its slope was decreased which means, respectively, higher nominal stall margin and reduced stall margin sensitivity to tip clearance.
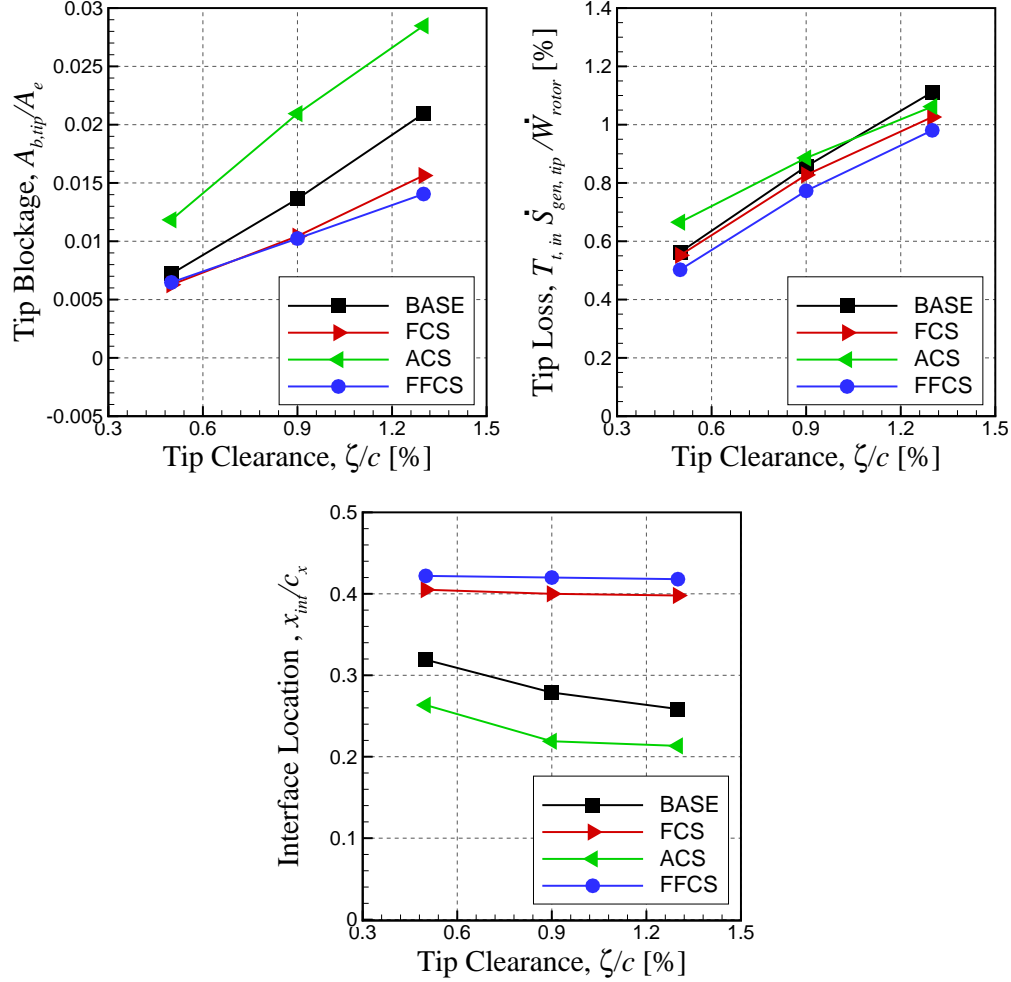
Figure 3.54: Detailed sensitivity study for FFCS at corrected mass flow rate of 3.04 kg/s

The sensitivity results thus confirmed that the combination of the desensitizing flow features of FCS and ACS produced a design, which is FFCS, with lower sensitivity to tip clearance than both FCS and ACS blades.

3.4.2 Partially Low Stagger Rotor

Double leakage can be reduced without increasing incoming tip momentum or pitch by lowering the stagger angle in the tip region. The partially low stagger (PLS) rotor was designed based on the BASE rotor design by preserving the stagger angle in the lower span region (below 50% span) and gradually reducing the stagger angle in the upper span region. However, initial PLS had higher corrected mass flow rate than the BASE rotor, and the stagger angle in the lower span region (below 50% span) was increased.

Figure 3.55 plots the PLS and BASE. The PLS rotor had almost the same (0.5° increase) hub profile as the BASE design. In the tip region, the PLS rotor has a 3° stagger angle reduction. More stagger angle reduction was not possible, due to the blade boundary layer separation and the need to replicate the constant spanwise loading of BASE profile. The resulting spanwise loading of PLS versus the BASE rotor is plotted in Figure 3.56, which shows similar spanwise loading.
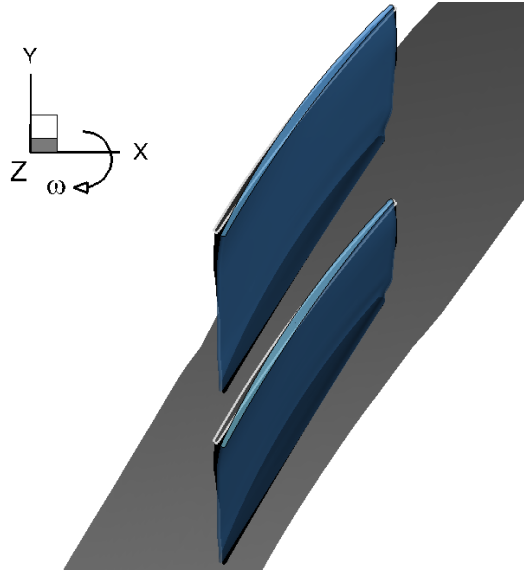
Figure 3.55: 3D view of PLS and BASE blades (blue: BASE, gray:PLS)
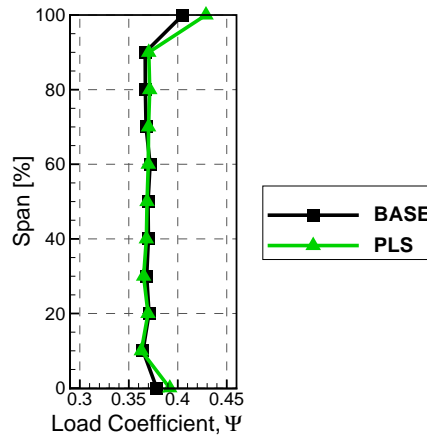

Figure 3.56: Spanwise loading distribution of PLS versus BASE at design conditions

The nominal (minimum tip clearance) performance and stall margin is listed in Table 3.11 indicating both the corrected design mass flow rate and the nominal total pressure ratio were preserved. Additionally, nominal peak efficiency was slightly increased and nominal stall margin was slightly decreased.

Table 3.11: Nominal performance of PLS versus BASE

Property	BASE	PLS
Corrected Design Mass Flow Rate	3.04 kg/s	3.04 kg/s
Total-to-Total Pressure Ratio	1.361	1.361
Total-to-Total Efficiency	92.24%	92.39%
Stall Margin	16.05%	15.70%

The removal/reduction of double leakage was assessed first by plotting the double leakage proportion with respect to tip clearance size in Figure 3.57 for the PLS design against the BASE and FFCS rotors. The results confirmed that the double leakage was least for PLS at all tip clearances and zero at minimum tip clearance. The comparison was made at corrected design mass flow rate of 3.04 kg/s, since the designs had the same total pressure ratio at that point.
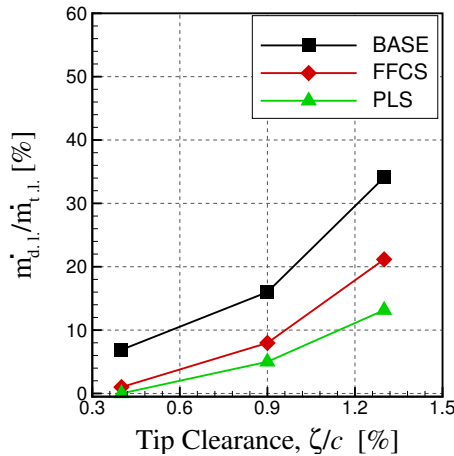
Figure 3.57: Double leakage proportion of PLS versus FFCS and BASE rotors at corrected mass flow rate of 3.04 kg/s

The high meridional momentum in the tip region was also checked. Since the corrected design mass flow rate of PLS was higher than FFCS and BASE blades, higher meridional momentum at the tip was expected if the blades were compared at corrected design mass flow rate of 3.04 kg/s. Figure 3.58 plots the spanwise distribution of meridional momentum (pitch-averaged) at the leading edge plane of PLS versus BASE and FFCS at corrected design mass flow rate of 3.04 kg/s. Figure 3.58 indicates that PLS has medium meridional momentum in the rotor tip region, such that it is higher than BASE, but less than FFCS.

The results of the general sensitivity study for PLS versus BASE and FFCS are shown in Figure 3.59, which indicates that, compared to the BASE blade, PLS decreased efficiency sensitivity by 29.1%, which was improved better than the FFCS blade, and decreased total pressure ratio sensi-
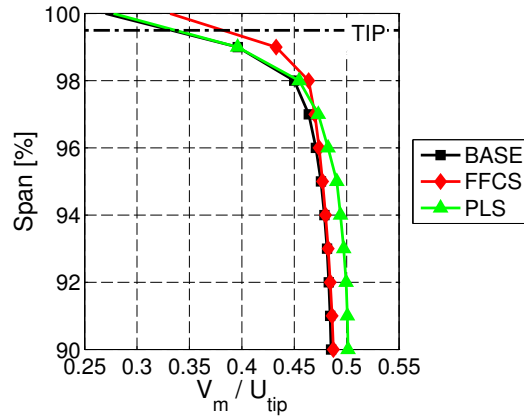
Figure 3.58: The spanwise distribution of meridional momentum of PLS at the leading edge plane at corrected mass flow rate of 3.04 kg/s

tivity by 15.9%, which was not improved as good as the FFCS blade. Figure 3.59 also shows that PLS provided a stability desensitization of 33% again worse than the FFCS blade, however, it had slightly worse stall margin than the BASE blade. The speedlines of PLS is given in Appendix E.4.

The results for the detailed sensitivity study in terms of tip blockage, entropy generation rate (tip loss) and inflow/tip clearance flow interface position are shown in Figure 3.60. As expected, a reduction in tip blockage and tip loss was observed, indicating a reduced sensitivity to tip clearance. Moreover, incoming/tip clearance flow interface position and its sensitivity to tip clearance was slightly reduced, which is consistent with Figure 3.59.

Figure 3.59: General sensitivity study for PLS at corrected mass flow rate of 3.04 kg/s

Figure 3.60: Detailed sensitivity study for PLS at corrected mass flow rate of 3.04 kg/s

Conclusion and Future Work
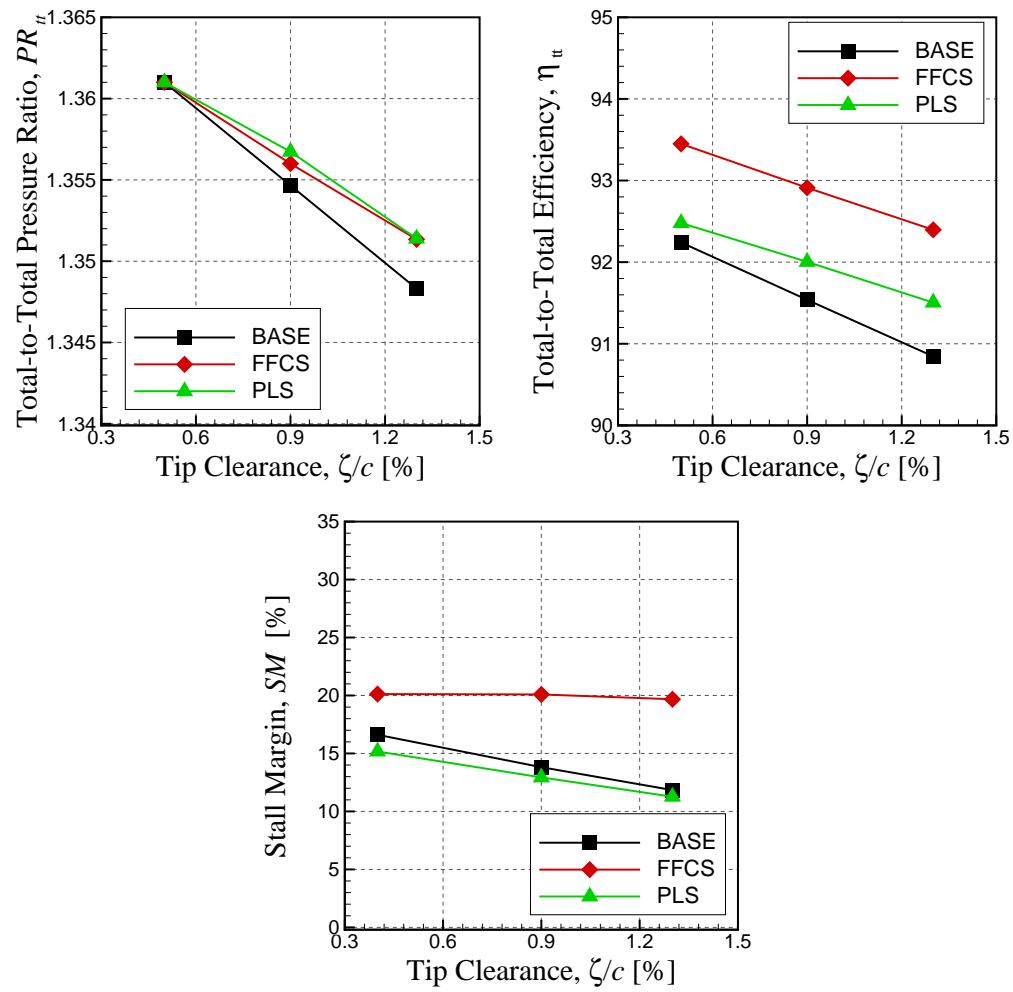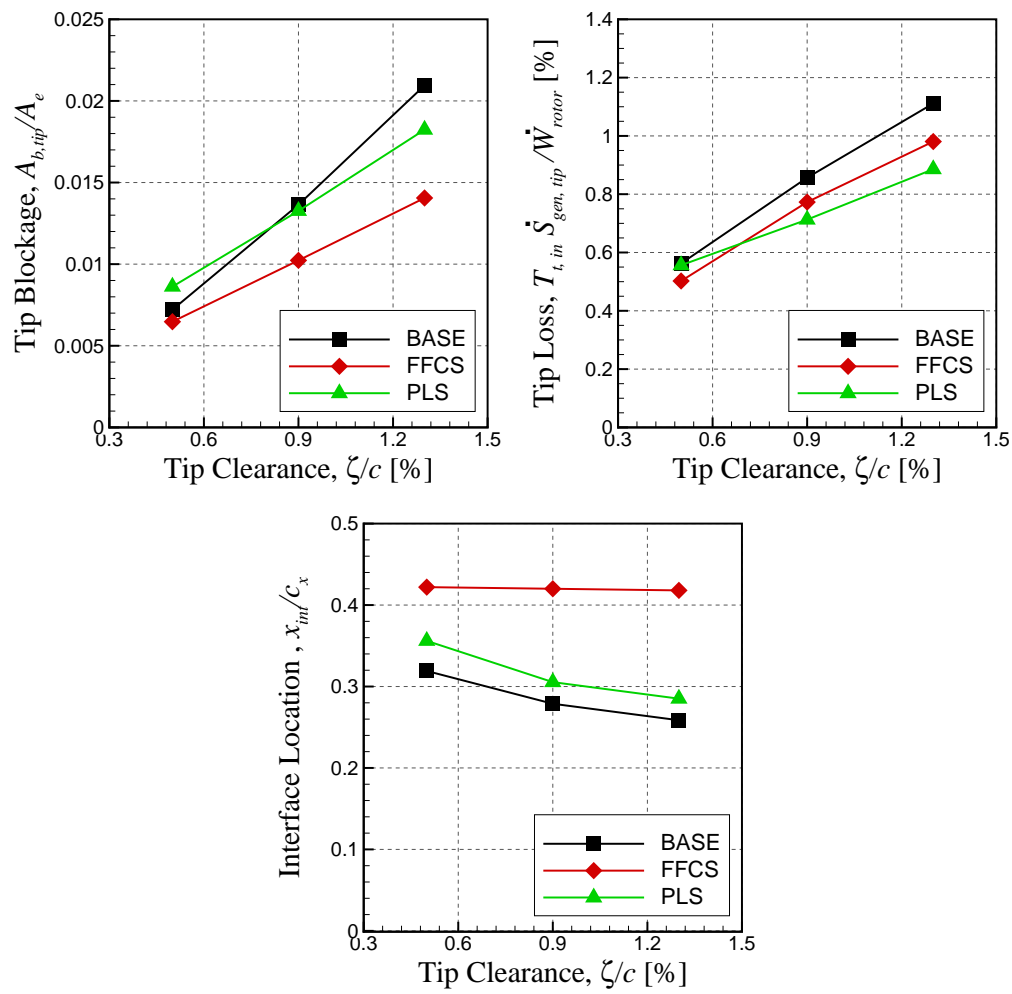
A computational study was carried out to determine the features for axial compressor blade design that would desensitize performance and aerodynamic stability to tip clearance without the need to reduce blade tip loading. A parametric design study, using variations in camber line and stacking line from a reference conventional radially-stacked axial rotor was carried out. The sensitivity of each design variation was computed from CFD simulations and the results compared to identify flow features that concur with the observed trends in sensitivity. These flow features were subsequently isolated, validated and explained through computational experiments and modeling. Two blade design characteristics that can exploit these features were then proposed and verified with CFD simulations.

The main conclusions/findings are:

1. Chordwise shift of blade tip loading distribution is not a potential desensitizing feature, contrary to what was implied from the literature.

2. Two flow features can reduce performance sensitivity to tip clearance: high incoming meridional momentum in the tip region, and a reduction or ideally, the elimination of double leakage flow.

3. Double leakage is detrimental to performance and stability because it reduces the streamwise momentum of the tip clearance flow and increases the tip clearance flow angle difference with the incoming flow. The proportion of double leakage with respect to total tip leakage rises with tip clearance. This explains explains the sensitivity increase in the presence of double leakage and conversely the desensitization effect of reducing or eliminating double leakage.

4. Incoming meridional momentum increase in the tip region reduces sensitivity to tip clearance both because of reduced double leakage and improved mixing with tip clearance flow, as demonstrated by an analytical model without double leakage flow.

5. Any blade design strategy that exploits both desensitizing flow features would reduce the performance and stability sensitivity to tip clearance. The increase of incoming meridional momentum can be achieved through forward chordwise sweep of the blade. The reduction of double leakage can be obtained without changing blade pitch by decreasing the blade stagger angle in the tip region. Both were numerically shown to be successful in reducing sensitivity to tip clearance.

The main contributions of this research are:

1. Identification of the flow features that desensitize performance and stability to tip clearance of an axial compressor rotor, including the explanations of the associated flow mechanisms;

2. Proposition of blade design characteristics that best embody the desensitizing flow features.

Based on the current research, the recommendations for future work include:

1. Investigate gas path design characteristics that can embody the desensitization flow features identified and further decrease sensitivity beyond what can be achieved with blade design alone;

2. Verify the applicability of the findings to stator blades with hub clearances;

3. Carry out experimental validation of the findings on a cascade and/or compressor test rig;

4. Optimize all design concepts based on the desensitization features; and finally,120

5. Investigate potential structural issues that may arise from incorporating the desensitizing features in a design.

References

AHN, C. S. and KIMI, K. Y. (2003). Aerodynamic Design Optimization of a Compressor Rotor with Navier-Stokes Analysis. *Proceedings of the Institution of Mechanical Engineers, Part A: Journal of Power and Energy*, 217, 179 – 183.

ANSYS (2006). Innovative Turbulence Modelling: SST Model in ANSYS CFX. Technical report, ANSYS Inc.

ARIMA, T., SONODA, T., SHIROTORI, M., TAMURA, A. and KIKUCHI, K. (1999). A Numerical Investigation of Transonic Axial Compressor Rotor Flow Using a Low-Reynolds-Number k-e Turbulence Model . *Journal of Turbomachinery*, 121, 44–58.

BEHESHTI, B. H., TEIXEIRA, J. A., IVEY, P. C., GHORBANIAN, K. and FARHANIEH, B. (2004). Parametric Study of Tip Clearance – Casing Treatment on Performance and Stability of a Transonic Axial Compressor. *Journal of Turbomachinery*, 126, 529–535.

BENINI, E. and BIOLLO, R. (2007). Aerodynamics of Swept and Leaned Transonic Compressor-Rotors. *Applied Energy*, 84, 1012–1027.

BERGNER, J., KABLITZ, S., HENNECKE, D., PASSRUCKER, H. and STEINHARDT, E. (2005). Influence of Sweep on the 3D Shock Structure in an Axial Transonic Compressor. *Proceedings of ASME Turbo Expo: Power for Land, Sea and Air*. Reno-Tahoe, Nevada, USA, GT2005–68835.

BIOLLO, R. and BENINI, E. (2008). Aerodynamic Behaviour of a Novel Three-Dimensional Shaped Transonic Compressor Rotor Blade. *Proceedings of ASME Turbo Expo: Power for Land, Sea and Air*. Berlin, Germany, GT2008–51397.

BONAIUTI, D., PITIGALA, A., ZANGENEH, M. and LI, Y. (2007). Redesign of a Transonic Compressor Rotor by Means of a Three-Dimensional Inverse Design Method: A Parametric Study. *Proceedings of ASME Turbo Expo: Power for Land, Sea and Air*. Montreal, Canada, GT2007–27486.

CAMP, T. R. and DAY, I. J. (1998). A Study of Spike and Modal Stall Phenomena in a Low-Speed Axial Compressor. *Journal of Turbomachinery*, 120, 393–401.

CORSINI, A. and RISPOLI, F. (2004). Using Sweep to Extend the Stall-Free Operational Range in Axial Fan Rotors. *Proceedings of the Institution of Mechanical Engineers, Part A: Journal of Power and Energy*, 218, 129 – 140.

CUMPSTY, N. A. (1989). *Compressor Aerodynamics*. Halsted Press.

DAY, I. J. (1993). Stall Inception in Axial Flow Compressors. *Journal of Turbomachinery*, 115, 1–9.

DENTON, J. (1997). Lessons from Rotor 37. *Journal of Thermal Science*, 6, 1–13.

DENTON, J. and XU, L. (1998). The Exploitation of Three-Dimensional Flow in Turbomachinery Design. *Proceedings of the Institution of Mechanical Engineers, Part C: Journal of Mechanical Engineering Science*, 213, 125–137.

DEPPE, A., SAATHOFF, H. and STARK, U. (2005). Spike-Type Stall Inception in Axial-Flow Compressors. *6th European Conference on Turbomachinery— Fluid Dynamics and Thermodynamics*. Lille, France, 178–188.

DOMERCQ, O. and ESCURET, J. (2007). Tip Clearance Effect on High-Pressure Compressor Stage Matching. *Proceedings of the Institution of Mechanical Engineers, Part A: Journal of Power and Energy*, 221, 759–767.

FREEMAN, C. (1985). Effect of Tip Clearance Flow on Compressor Stability and Engine Performance. *Lecture Series*, Von Karman Institute for Fluid Dynamics. 1985–5.

GALLIMORE, S., BOLGER, J., CUMPSTY, N., TAYLOR, M., WRIGHT, P. and PLACE, J. (2002a). The Use of Sweep and Dihedral in Multistage Axial Flow Compressor Blading, Part I: University Research and Methods Development. *Journal of Turbomachinery*, 124, 521–532.

GALLIMORE, S., BOLGER, J., CUMPSTY, N., TAYLOR, M., WRIGHT, P. and PLACE, J. (2002b). The Use of Sweep and Dihedral in Multistage Axial Flow Compressor Blading, Part II: Low and High-Speed Designs and Test Verification. *Journal of Turbomachinery*, 124, 533.

GOLLER, M., GUMMER, V., CLEMEN, C. and SWOBODA, M. (2005). Enhancement of Highly-Loaded Axial Compressor Stage Performance Using Rotor Blade Tip Tailoring. Part I–Numerical Design Studies. *Proceedings of the 6th European Conference on Turbomachinery Fluid Dynamics and Thermodynamics, Lille, France*. 88–99.

GREITZER, E. M. (1976). Surge and Rotating Stall in Axial Compressors, Parts I and II. *Journal of Engineering for Power*, 98, 190–217.

HAH, C. (2009). Large Eddy Simulation Of Transonic Flow Field In NASA Rotor 37. *AIAA 47th Aerospace Sciences Meeting*. Orlando, Florida, USA, NASA/TM 2009–215627.

HAH, C., BERGNER, J. and SCHIFFER, H. (2006). Short Length-Scale Rotating Stall Inception in a Transonic Axial Compressor: Criteria and Mechanisms. *Proceedings of ASME Turbo Expo: Power for Land, Sea and Air*. Barcelona, Spain, GT2006–90045.

HAH, C., SCHULZE, R., WAGNER, S. and HENNECKE, D. K. (1999). Numerical and Experimental Study for Short Wavelength Stall Inception in a Low-Speed Axial Compressor. *Proc. 14th Int. Symposium Air Breathing Engines*. Florence, Italy, ISABE–99–7033.

IANDOLI, C. L. and SCIUBBA, E. (2010). 3-D Numerical Calculation of the Local Entropy Generation Rates in a Radial Compressor Stage. *International Journal of Applied Thermodynamics*, 8.

JANG, C. and KIM, K. (2005). Optimization of a Stator Blade Using Response Surface Method in a Single-Stage Transonic Axial Compressor. *Proceedings of the Institution of Mechanical Engineers, Part A: Journal of Power and Energy*, 219, 595–603.

JANG, C., LI, P. and KIM, K. (2005). Optimization of Blade Sweep in a Transonic Axial Compressor Rotor. *JSME International Journal Pages B*, 48, 793–801.

KHALID, S. (1995). *The Effects of Tip Clearance on Axial Compressor Pressure Rise*. Doctoral thesis, Massachusetts Institute of Technology.

KHALID, S. A., KHALSA, A. S., WAITZ, I. A., TAN, C., GREITZER, E. M., CUMPSTY, N. A., ADAMCZYK, J. J. and MARBLE, F. E. (1999). Endwall Blockage in Axial Compressors. *Journal of Turbomachinery*, 121, 499–509.

KHALSA, A. S. (1996). *Endwall Blockage in Axial Compressors*. Doctoral thesis, Massachusetts Institute of Technology.

LEE, K., KIM, K. and SAMAD, A. (2008). Design Optimization of Low-Speed Axial Flow Fan Blade with Three-Dimensional RANS Analysis. *Journal of Mechanical Science and Technology*, 22, 1864–1869.

LIU, Y., YU, X. and LIU, B. (2008). Turbulence Models Assessment for Large-Scale Tip Vortices in Axial Compressor Rotor. *Journal of Propulsion and Power*, 24.

MARZ, J., HAH, C. and NEISE, W. (2002). An Experimental and Numerical Investigation Into the Mechanisms of Rotating Instability. *Journal of turbomachinery*, 124, 367–375.

MCNULTY, G., DECKER, J., BEACHER, B. F. and KHALID, S. A. (2004). The Impact of Forward Swept Rotors on Tip Clearance Flows in Subsonic Axial Compressors. *Journal of Turbomachinery*, 126, 445–454.

MOORE, F. K. and GREITZER, E. M. (1986). A Theory of Post-Stall Transients in Axial Compressors, Part 1 - Development of Equations. *Journal of Engineering for Gas Turbines and Power*, 108, 68–76.

PASSRUCKER, H., ENGBER, M., KABLITZ, S. and HENNECKE, D. (2003). Effect of Forward Sweep in a Transonic Compressor Rotor. *Proceedings of the Institution of Mechanical Engineers, Part A: Journal of Power and Energy*, 217, 357–365.

RAMAKRISHNA, P. and GOVARDHAN, M. (2009a). Combined Effects of Forward Sweep and Tip Clearance on the Performance of Axial Flow Compressor Stage. *Proceedings of ASME Turbo Expo: Power for Land, Sea and Air*. Orlando, Florida, USA, GT2009–59840.

RAMAKRISHNA, P. and GOVARDHAN, M. (2009b). Stall Characteristics and Tip Clearance Effects in Forward Swept Axial Compressor Rotors. *Journal of Thermal Science*, 18, 40–47.

RAMAKRISHNA, P. and GOVARDHAN, M. (2009c). Study of Sweep and Induced Dihedral Effects in Subsonic Axial Flow Compressor Passages, Part I: Design Considerations; Changes in Incidence, Deflection, and Streamline Curvature. *International Journal of Rotating Machinery*, 787145.

RAMAKRISHNA, P. and GOVARDHAN, M. (2010). Study of Sweep and Induced Dihedral Effects in Subsonic Axial Flow Compressor Passages, Part II: Detailed Study of the Effects on Tip Leakage Phenomena. *International Journal of Rotating Machinery*, 491413.

REID, L. and MOORE, R. (1978). Design and Overall Performance of Four Highly Loaded, High Speed Inlet Stages for an Advanced High-Pressure-Ratio Core Compressor. Technical report, NASA.

SHAO, W., JI, L. and CHENG, R. (2007). Basic Analysis of Tip Leakage Mixing Loss. *Proceedings of ASME Turbo Expo: Power for Land, Sea and Air*. Montreal, Quebec, Canada, GT2007–27616.

SIRAKOV, B. T. and TAN, C. S. (2002). Effect of Upstream Unsteady Flow Conditions on Rotor Tip Leakage Flow. *Proceedings of ASME Turbo Expo: Power for Land, Sea and Air*. Amsterdam, Netherlands, GT2002–30358.

STORER, J. A. and CUMPSTY, N. A. (1991). Tip Leakage Flow in Axial Compressors. *Journal of Turbomachinery*, 113, 252–258.

STORER, J. A. and CUMPSTY, N. A. (1994). An Approximate Analysis and Prediction Method for Tip Clearance Loss in Axial Compressors. *Journal of Turbomachinery*, 116, 648–656.

SUDER, K. and CELESTINA, M. (1996). Experimental and Computational Investigation of the Tip Clearance Flow in a Transonic Axial Compressor Rotor. *Journal of Turbomachinery*, 118, 218–229.

SUDER, K., CHIMA, R., STRAZISAR, A. and ROBERTS, W. (1995). The Effect of Adding Roughness and Thickness to a Transonic Axial Compressor Rotor. *Journal of Turbomachinery*, 117, 491–506.

SUDER, K. L. (1998). Blockage Development in a Transonic, Axial Compressor Rotor. *Journal of Turbomachinery*, 120, 465–476.

SZABO, I. (2008). *A Numerical Study of Water Injection on Transonic Compressor Rotor Performance*. Doctoral thesis, UNIVERSITY OF CINCINNATI.

SZABO, I. and TURNER, M. (2008). An Entropy Based Evaluation of Efficiency of a Transonic Compressor Rotor With Water Injection. *Proceedings of ASME Turbo Expo 2008: Power for Land, Sea and Air*. ASME, Berlin,Germany, GT–2008–50248.

TAKATA, H. and TSUKUDA, Y. (1977). Stall Margin Improvement by Casing Treatment—Its Mechanism and Effectiveness. *Journal of Engineering for Power*, 99, 121–133.

TSCHIRNER, T., JOHANN, E., MULLER, R. and VOGELER, K. (2006). Effects of 3D Aerofoil Tip Clearance Variation on a 4-Stage Low Speed Compressor. *Proceedings of ASME Turbo Expo: Power for Land, Sea and Air*. Barcelona, Spain, GT2006–90902.

VAD, J. and CORSINI, A. (2002). Comparative Investigation on Axial Flow Indutrial Fans of High Specific Perfomance with Unswept and Forward Swept Blades at Design and Off-design Conditions. *Proceedings of 9th International Symposium on Transport Phenomena and Dynamics of Rotating Machinery*. ISROMAC-9, Honolulu,Hawaii, USA, FD–ABS–0016.

VAN ZANTE, D. E., STRAZISAR, A. J., WOOD, J. R., HATHAWAY, M. D. and H., O. T. (2000). Recommendations for Achieving Accurate Numerical Simulation of Tip Clearance Flows in Transonic Compressor Rotors. *Journal of Turbomachinery*, 122, 733–742.

VO, H. (2001). *Role of Tip Clearance Flow on Axial Compressor Stability*. Doctoral thesis, Massachusetts Institute of Technology.

VO, H. D., TAN, C. S. and GREITZER, E. M. (2008). Criteria for Spike Initiated Rotating Stall. *Journal of Turbomachinery*, 130, 011023.

WADIA, A., HAH, C. and RABE, D. (2004). The Impact of Forward Sweep on Tip Clearance Flows in Transonic Compressors. *24th International Congress of the Aeronautical Sciences*. Yokohama, Japan, ICAS2004–6.2.1.

WISLER, D. C. (1985). Aerodynamic Effects of Tip Clearance, Shrouds, Leakage Flow, Casing Treatment, and Trenching in Compressor Design. *Lecture Series*, Von Karman Institute for Fluid Dynamics. 1985–5.
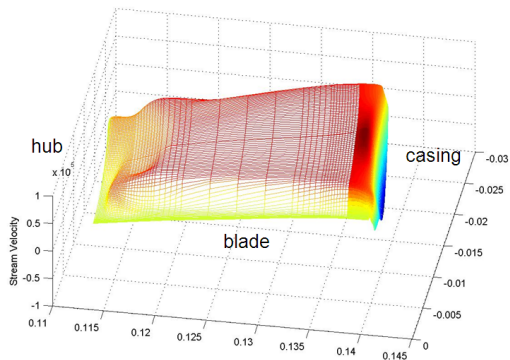
Appendix A

Sources of Losses and Stall

A.1 Tip Blockage

The blockage calculation is based on the 3-D streamwise velocity deficit formulation proposed by Khalid *et al*. (1999). The calculation of blockage includes following steps:
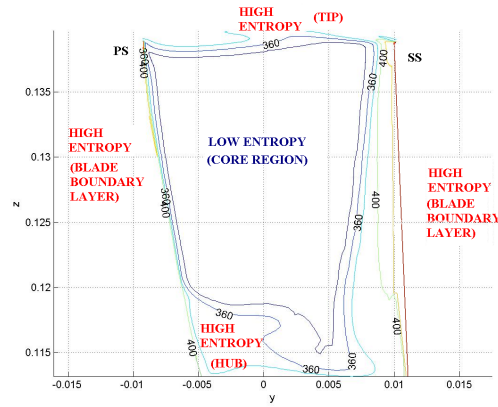
1. First, the relative velocity (u_{rel}) and direction (α_{rel}) for each span is calculated at trailing edge plane.

$$u_{rel} \quad = \quad \sqrt{V_x^2 + V_{\theta,rel}^2} \tag{A.1}$$

$$\alpha_{rel} \quad = \quad \arctan(\frac{V_{\theta,rel}}{V_x}) \tag{A.2}$$

(a) Streamwise Velocity Distribution   (b) Entropy Contours

Figure A.1: Streamwise Velocity Distribution

2. Second, the streamwise direction (α_{str}) for each span position at the trailing edge plane is calculated. The streamwise angle is defined as the core flow angle. The core flow angle is chosen

as pitch-averaged low-entropy flow angle. An example for streamwise velocity distribution is shown in Figure A.1. It can be observed that there are high gradients in streamwise velocity near high entropy regions like near hub and near shroud. In these high entropy-regions the nearest edge of the low-entropy region (core region) is used. Knowing the direction, the velocity component in the streamwise direction (u_{str}) can be found in a straight-forward manner, as given below.

$$s_{@span} = s_{low} \implies \alpha_{str} = \left(\frac{\sum (\alpha_{rel} \, \Delta(\theta))}{\sum \Delta(\theta)} \right)_{@span} \tag{A.3}$$

$$s_{@span} = s_{high} \implies \alpha_{str} = (\alpha_{rel})_{@edge} \tag{A.4}$$

$$u_{str} = u_{rel} \times \tan(\alpha_{rel} - \alpha_{str}) \tag{A.5}$$

3. Next, using gradient vector of streamwise velocity ($\nabla(\rho u_{str})$) composed of radial and tangential gradients, the core and blockage regions are differentiated. Moreover, higher values of radial gradient of streamwise velocity is used to isolate the tip blockage region. In Figure A.2, the core flow, boundary blockage and tip blockage regions (isolated with this technique) are shown. Then, the tip blockage area is calculated as a integral area of momentum deficit of the edge momentum ($\rho_e u_e$) associated with the near location in the core flow region

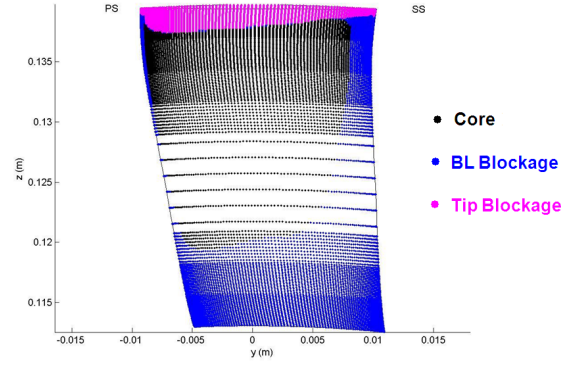$$A_b = \iint \left(1 - \frac{\rho u_{str}}{\rho_e u_e} \right) dA \tag{A.6}$$

Figure A.2: Blockage Area
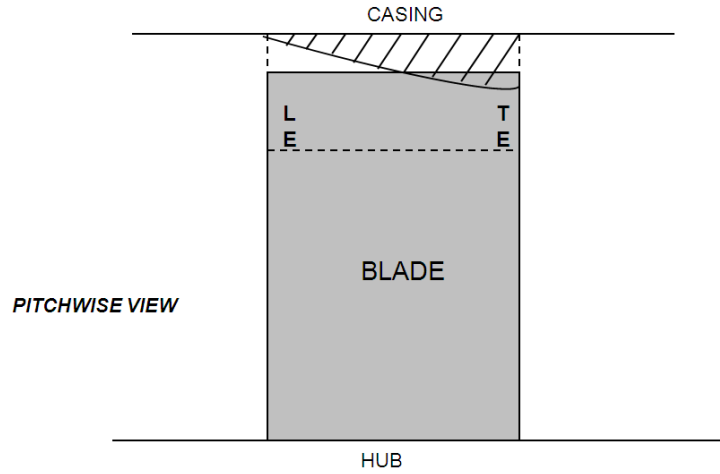
A.2 Tip Loss

Figure A.3: Definition of tip loss

Tip loss is defined as the entropy generation rate at the tip region. The formulation of entropy generation rate is given in section A. Tip loss is created by shear/mixing layer between tip clearance and incoming flow and it is located in the tip blockage region. Thus, after tip blockage region is calculated, a control volume just including tip blockage region is selected as shown in Figure A.3. Then, entropy generation rate is volume-integrated in that control volume.

The entropy generation rate can be found by summing viscous losses and and heat losses in the simulation. The viscous and heat losses are calculated simply by using velocity gradients and temperature gradients, respectively. The formulation and details are given by Iandoli and Sciubba (2010); Szabo and Turner (2008); Szabo (2008).

$$\dot{S}_{gen} \quad = \quad \frac{ds}{dt} = \dot{s}_v + \dot{s}_t \tag{A.7}$$

$$
\begin{aligned}
\dot{s}_v \quad &= \quad \mu\frac{\Phi}{T} \\
&= \quad \frac{\mu_k + \mu_\epsilon}{T}\left\{2\left[\left(\frac{\partial u}{\partial x}\right)^2 + \left(\frac{\partial v}{\partial y}\right)^2 + \left(\frac{\partial w}{\partial z}\right)^2\right] + \left(\frac{\partial v}{\partial x} + \frac{\partial u}{\partial y}\right)^2\right. \\
&\quad + \left. \left(\frac{\partial v}{\partial z} + \frac{\partial w}{\partial y}\right)^2 + \left(\frac{\partial w}{\partial x} + \frac{\partial u}{\partial z}\right)^2 - \frac{2}{3}\left(\frac{\partial u}{\partial x} + \frac{\partial v}{\partial y} + \frac{\partial w}{\partial z}\right)^2\right\}
\end{aligned}
\tag{A.8}
$$

$$
\begin{aligned}
\dot{s}_t \quad &= \quad k\frac{\nabla^2 T}{T^2} \\
&= \quad \frac{k}{T^2}\left\{\left(\frac{\partial T}{\partial x}\right)^2 + \left(\frac{\partial T}{\partial y}\right)^2 + \left(\frac{\partial T}{\partial z}\right)^2\right\}
\end{aligned}
\tag{A.9}
$$

Appendix B

Blade Design Program

The blade design is performed with an in-house blade generation program. The blade design program incorporates a mean-line and through-flow code. In a mean-line approach, the blade calculations are made at the mid-span location. In a through-flow, the flow remains in concentric stream-tubes as it passes through the turbomachine, and no mass transfer occurs across the meridional streamlines. The inputs and outputs of the program are listed below:

1. Inputs:
   - hub radius
   - hub-to-tip radius ratio
   - inlet conditions (stagnation pressure and temperature)
   - camber line shape parameter: Single circular arc or double circular arc parameters can be selected.
   - chordwise thickness distribution: Example symmetrical profiles can be employed or thickness distribution can be edited manually.
   - flow coefficient: Flow coefficient (ϕ) is axial velocity (V_x). divided by rotational velocity (U). The mean value flow coefficient is supplied to program.

$$\varphi \quad = \quad \frac{V_x}{U} \tag{B.1}$$

   - tip mach number: Blade tip mach number (M_{tip}) is defined as rotational speed (U_{tip}) at tip divided by speed of sound (a_{tip})

$$M_{tip} \quad = \quad \frac{U_{tip}}{a_{tip}} \tag{B.2}$$

   - load coefficient: For any blade, the spanwise load factor distribution (ψ) is calculated by the difference between inlet and exit total enthalpies ($h_{t,2} - h_{t,1}$) divided by square of rotational velocity (U). This formula can be non-dimensionalized and a simple function of 2D angles (where α_1 is absolute inlet angle and β_2 is relative exit angle of flow) and flow coefficient (ϕ) can be found.

$$\psi \;=\; \frac{h_{t,rel,2} - h_{t,rel,1}}{U^2} = 1 - \phi\,(tan\,\alpha_1 + tan\,\beta_2) \tag{B.3}$$

– loss correlation: The loss is defined as total relative pressure difference between the inlet and exit. The axial velocity is assumed to be constant through the stream tube, so the stream tube direction and exit area is decided by the loss. The loss correlation employed in the design program is an empirical correlation for NACA 65 profile.

– deviation correlation: The deviation is defined as difference of flow exit angle (β_2) and blade exit angle (β_2'). In blade design program, deviation is calculated empirically and the blade exit angle is changed to have intended flow exit angle. The deviation correlation employed in the design program is an empirical correlation for NACA 65 profile.

2. Outputs:
   – blade profile coordinates at each span
   – design pressure ratio
   – design mass flow

The program works essentially as follows: for each span,

- local speed is calculated using flow coefficient, tip mach number and inlet conditions
- velocity triangles are employed to get required inlet/exit flow angles to meet loading coefficient
- loss correlations are used to set meridional streamlines and to calculate design mass flow and pressure ratio
- deviation is taken into account to set blade inlet/exit angles
- camber line shape and thickness distribution are applied

Appendix C

Performance and Stability of PWC Rotor

The speedlines of PWC rotor is shown in Figure C.1. It is noted that capturing the stall point is highly challenging. In terms of computational time, it is found in the present case that transient simulations are required below the optimum efficiency corrected mass flow, due to oscillations in the flow field. The transient simulations are time consuming, because of much smaller time steps. In addition, one has to wait for the oscillations in the flow field to settle into a periodic state with constant amplitude. Moreover, transient oscillations usually displays multiple frequencies which make determining the period for time averaging more challenging. Once the period is determined, each run has to be restarted in order to specify number of iterations for time-averaging of required variables.
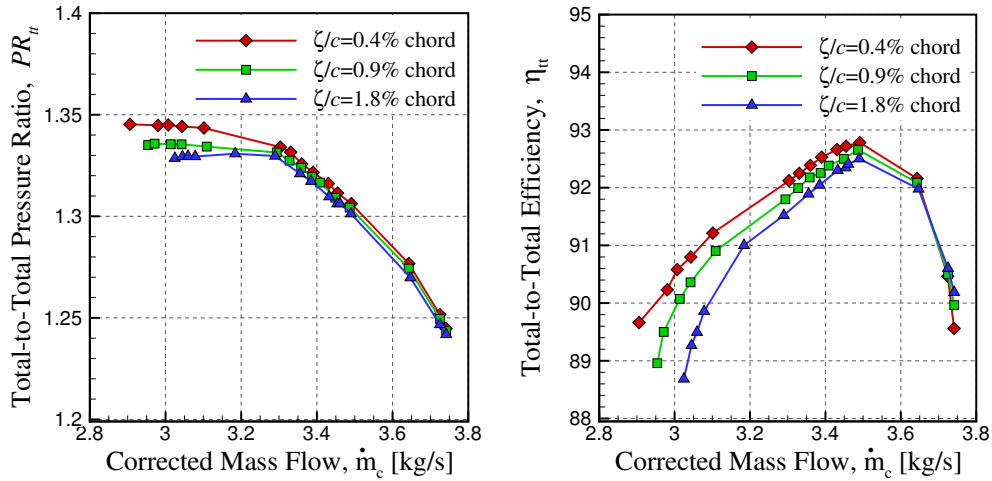
Figure C.1: Total-to-total pressure ratio and efficiency curves for PWC rotor geometry at different tip clearances (repeated Figure 3.5)

The computational setup can also prevent the capture of the stall point. The simulations are run by specifying inlet total pressure distribution and exit static pressure. The mass flow is reduced by increasing the value of exit static pressure. Thus, this approach cannot capture any solutions (including the stall point), that lie at a mass flow lower than the zero-slope peak of the total-to-static pressure rise characteristic. The variation of total-to-static pressure ratio (domain inlet P_t to domain exit P_s) with corrected mass flow rate for different tip clearance sizes is given in Figure

C.2. The figure indicates that the last points of simulation have almost the zero-slope peak of the total-to-static pressure rise. Thus, numerical simulations can not capture a lower mass flow.
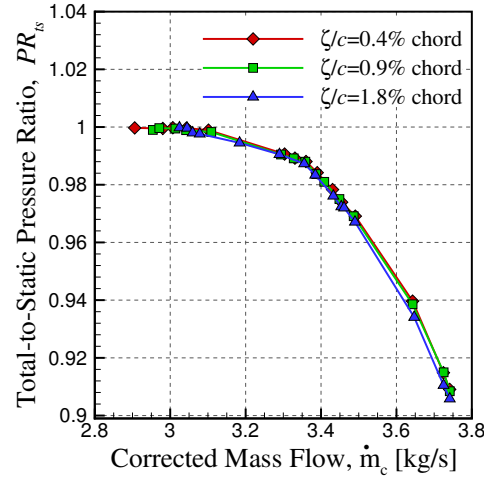

Figure C.2: Total-to-static pressure ratio curves for PWC rotor at different tip clearances (repeated Figure 3.6

Near stall simulations of PWC Rotor shows some hub/boundary layer separation bubbles appear in lower mass flow rates which expands and cause stall due to corner/boundary layer separation. Figure C.3 plots axial shear contours on suction side for PWC Rotor at lowest tip clearance size. Figure indicates that the separation bubbles near hub and lower span at $\dot{m}_c$=3.10 kg/s expands and cause massive flow separation before stall at $\dot{m}_c$= 2.90 kg/s. Thus, stall occurs due to corner stall , rather than inflow/tip clearance flow mixing.

(a) $\dot{m}_c$=3.10 kg/s   (b) $\dot{m}_c$= 2.90 kg/s
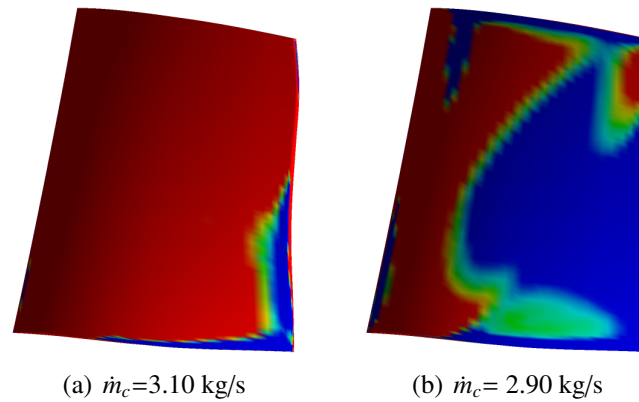
Figure C.3: Axial shear contours on suction side for PWC Rotor of ζ/c=0.4%chord

Appendix D

Reference Blade Design (BASE) Rotor

D.1   Double Circular Arc (DCA) Profile

DCA profile is a transonic speed rotor profile for axial turbomachinery. It is generated by one circular arc on suction side and one circular arc on pressure side. For thickness, a circle, whose diameter equals to the blade thickness, is located at mid-chord. Both circular arcs should be tangent to this circle. Moreover, the leading edge and trailing edge are small circles of machinable radius that are tangent to these circular arcs. A schematic of DCA profile is shown in Figure D.1.
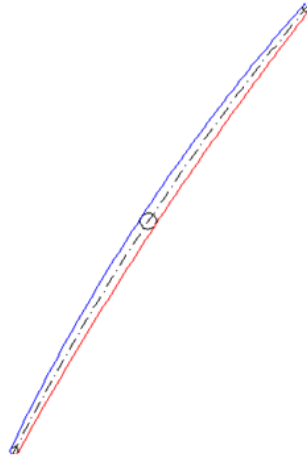
Figure D.1: Schematic of DCA

D.2   Design iterations of BASE blade

The input loading distribution of PWC Rotor is changed when designing the BASE Rotor. This change is due to boundary layer separations due to high incidence and high flow turning near the hub region. The BASE design is iterated to have no boundary layer separations.

To remove the boundary layer separation on the first DCA blade suction side near the hub, the design is iterated by modifying the loading distribution. The loading near the hub is reduced and the loading at higher span is increased to compensate. This process is performed until the

loading distribution become constant, as shown in figure D.2(a). This procedure proved to be unsuccessful in eliminating suction side boundary layer separation completely. Modification of loss correlations only caused more problems with premature choking. Following feedback from PWC, the spanwise blade profile at each span is altered in inlet and/or exit camber directly. If there is a separation near leading edge due to incidence, the blade inlet angle is aligned to inlet flow. If there is a separation near trailing edge due to deviation, the blade exit angle is increased to aligned to exit flow. Eventually, a non-separated blade is achieved, however, it has lower overall loading than PWC rotor. Thus, the loading of outer span is increased to compensate and come as close as possible to the overall loading (i.e. pressure ratio) of the PWC rotor. The loading distributions of a few iterations and final loading distributions are presented in Figure D.2(b).

(a) Reference blade design trials

(b) Final reference blade (BASE) design (Repeated Figure 3.10)
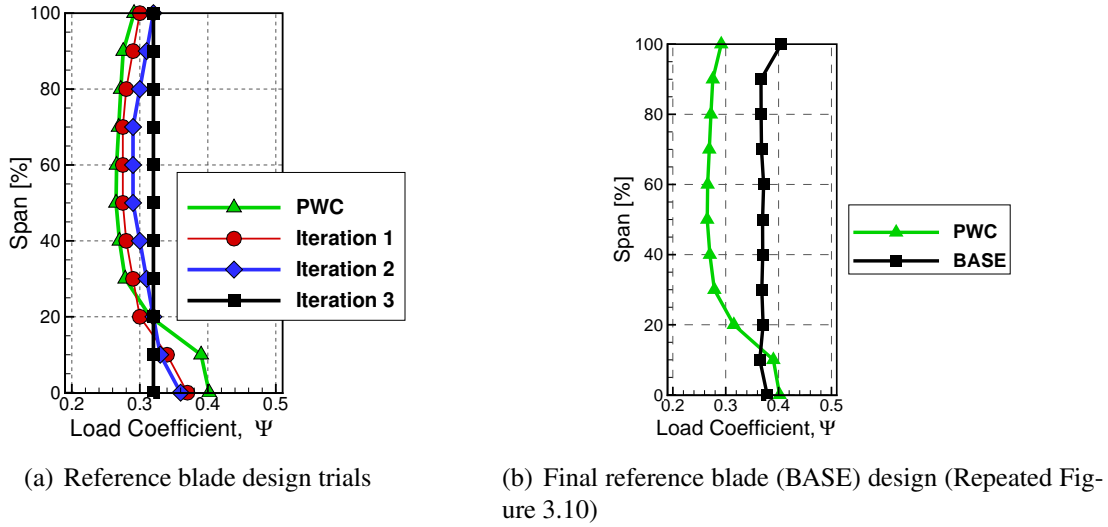
Figure D.2: Iterations of DCA

D.3 Performance and stability of BASE blade

A preliminary assessment of the tip criticality of revised DCA design (BASE) is initiated. This is performed by carrying out steady simulations up to convergence limit to assess the proposed tip clearance flow-related spike stall criteria as well as insuring that there is no boundary layer separation on the blade surfaces (as explained in Chapter 3). The total-to-total pressure ratio, adiabatic efficiency and total to static pressure ratio curves are shown in Figure D.3. The highest efficiency is achieved at corrected mass flow of 3.04 kg/s with 1.361 total pressure ratio and 92.24% total-to-total efficiency. For comparison PWC rotor has its highest efficiency point at corrected mass flow if 3.49 kg/s with 1.306 total pressure ratio and 92.78% total-to-total efficiency. Therefore, the

reference blade has higher loading and almost same efficiency, in other words higher performance, but lower design mass flow, compared to PWC rotor.

(a) Total-to-total pressure ratio

(b) Total-to-total efficiency
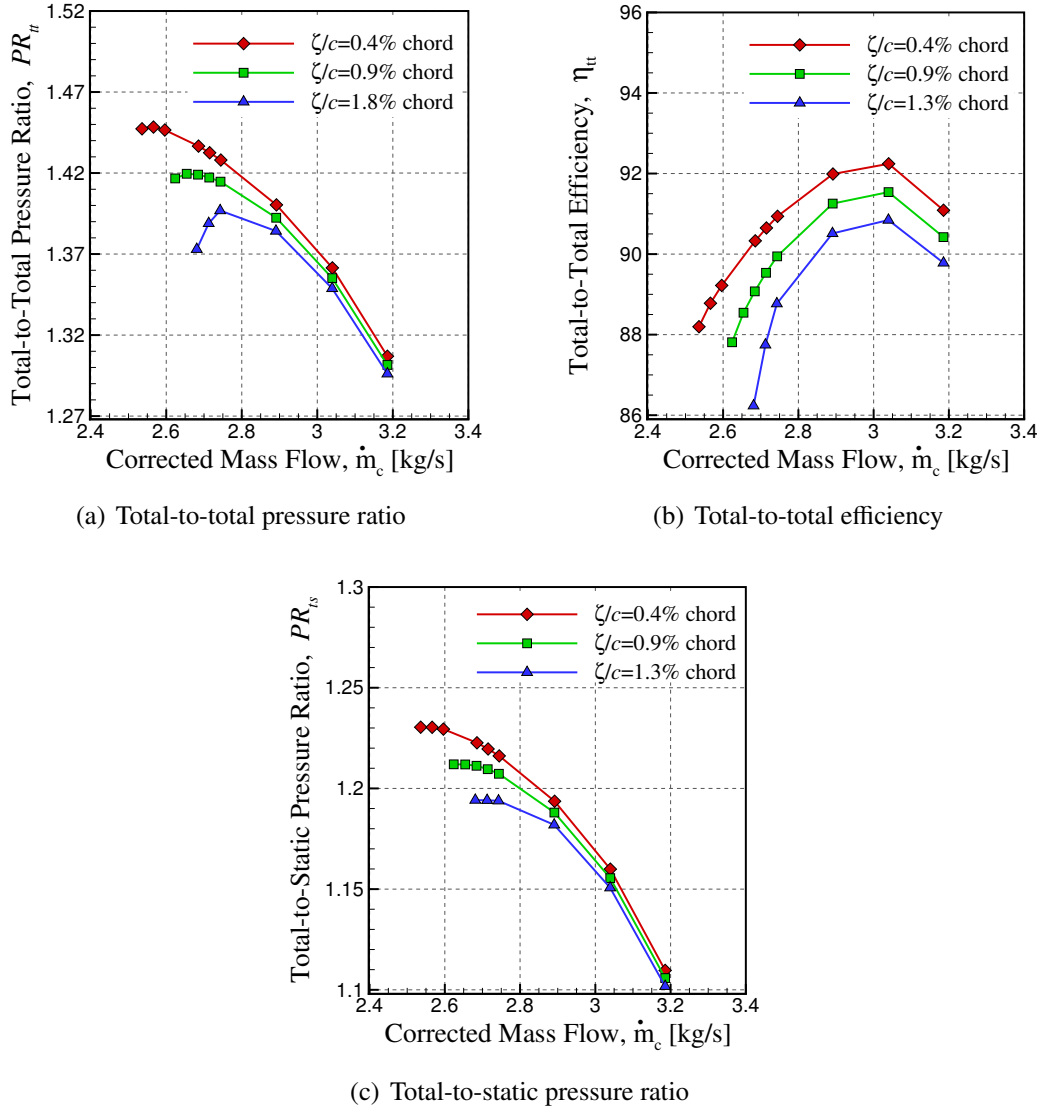

(c) Total-to-static pressure ratio

Figure D.3: Simulation of speedlines for BASE rotor

Between 3.26 kg/s and 2.80 kg/s steady simulations converged to steady solution. However, below 2.80 kg/s, the steady simulations started to oscillate. To be on safe side, for the simulations between 2.80 kg/s and 2.90 kg/s, a transient simulations is run using the steady simulation as initial condition. Therefore, below 2.80 kg/s transient simulations are run. All transient simulations shown are converged. The last converged simulation for 0.005 inch tip clearance size is achieved at corrected mass flow 2.49 kg/s with a almost zero slope total-to-static-pressure rise (Figure D.3). The two proposed spike stall inception criteria are assessed in figure D.4. The entropy contours

(a) Entropy contours at blade tip

(b) Axial wall shear contours
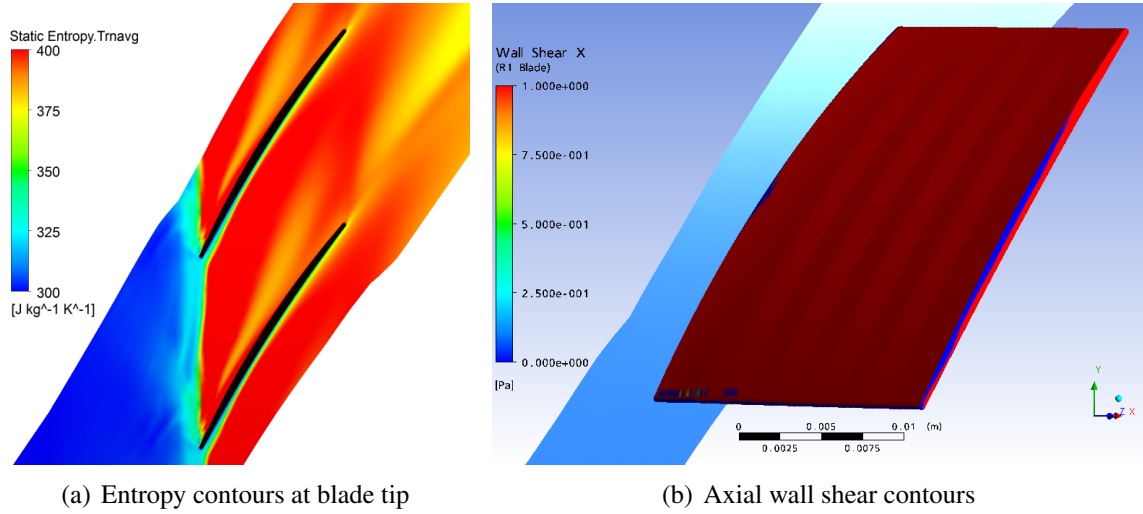
Figure D.4: Assessment of spike stall criteria for BASE rotor at $\dot{m}_c$=2.54 kg/s for ζ=0.4% chord)

at the blade tip in Figure D.4(a), indicate that the incoming/tip clearance flow has reached the leading edge plane. Figure D.4(b) plots axial shear contours at corrected mass flow 2.54 kg/s (last converged point) of 0.005 inch tip clearance size. A small boundary layer separation region is observed at this last converged point of 0.005 inch tip clearance size. Since the total-to-static pressure ratio characteristics has reached beyond zero slope, it may be possible that the actual stall point lies beyond this point and can not be captured computationally due to exit static pressure boundary condition. The results point to the need for a stall transient simulation beyond the zero-slope peak of the total-to-static pressure ratio characteristics to confirm tip criticality.

To run a stall-transient the back pressure is increased a little and flow field is checked to achieve either backflow at trailing edge or boundary layer separation. The backflow at trailing edge is observed first at corrected mass flow rate of 2.49 kg/s. The entropy contours at blade tip and axial wall shear contours of corrected mass flow rate of 2.49 kg/s is plotted in Figure D.5. One can observe that the incoming/tip clearance flow interface reached leading edge before the separation bubble expands. This proves that BASE blade is tip critical.

The last converged solutions so far for tip clearances of 0.9% and 1.3% chord are achieved at 2.62 kg/s and 2.68 kg/s, respectively. The entropy contours at blade tip and backflow at trailing edge plane for 0.9% and 1.3% chord tip clearance at these points is shown in Figure D.6 and D.7, respectively. It can be observed that the incoming/tip clearance interface has reached the leading edge plane for both tip clearances. Also, the narrow range axial shear stress contours on the blade suction surface is plotted for 0.9% and 1.3% chord tip clearance in figures D.6(b) and D.7(b). No separation regions are observed, except a small region in near leading edge.
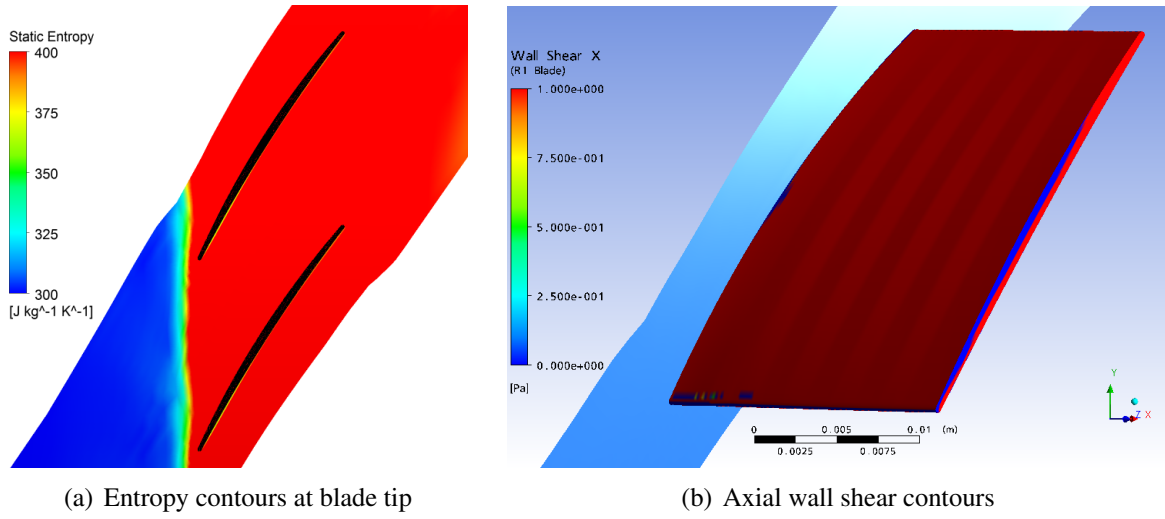
(a) Entropy contours at blade tip

(b) Axial wall shear contours

Figure D.5: Assessment of spike stall criteria for BASE rotor at $\dot{m}_c$=2.49 kg/s for ζ=0.4% chord

(a) Entropy contours at blade tip

(b) Axial wall shear contours
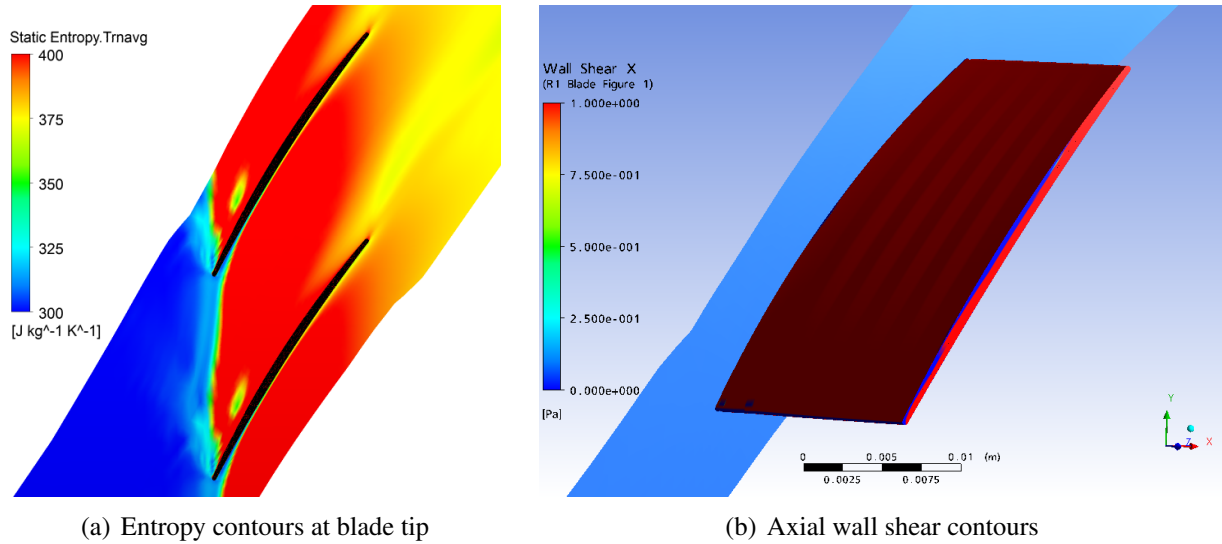
Figure D.6: Assessment of spike stall criteria for BASE rotor at $\dot{m}_c$=2.62 kg/s for ζ = 0.9% chord

(a) Entropy contours at blade tip

(b) Axial wall shear contours
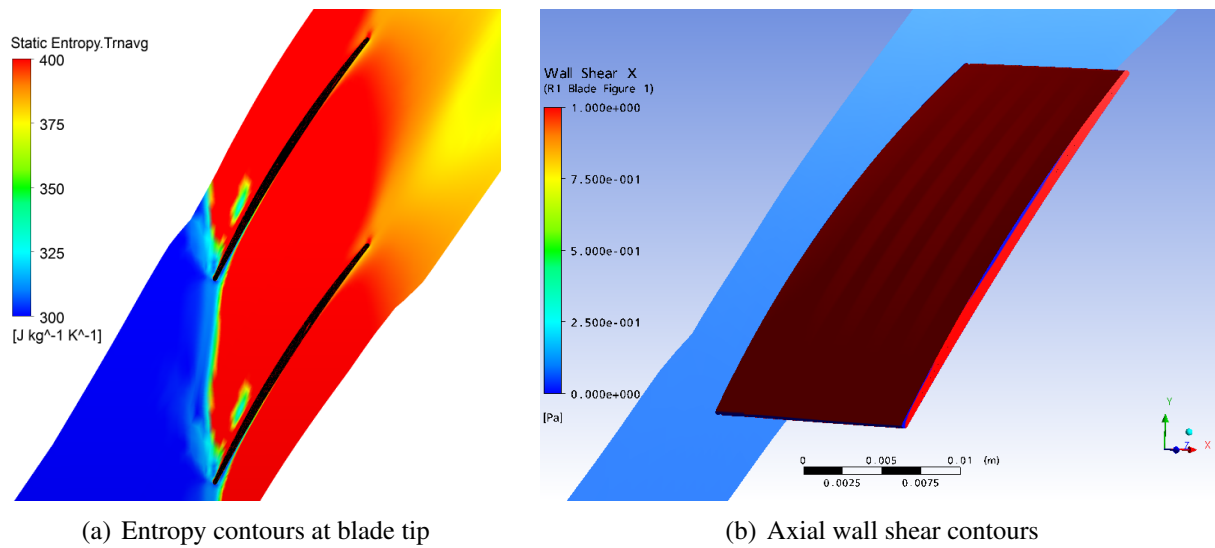
Figure D.7: Assessment of spike stall criteria for BASE rotor at $\dot{m}_c$=2.68 kg/s for ζ = 1.3% chord

Appendix E

Performance and Stability of Selected Blade Designs

E.1   Nominal performance of design variations in section 3.2.2

The nominal (at $\zeta = 0.4\%$ chord) performance of each design variation is illustrated in Tables E.1 to E.5. As observed, all design variations have same total pressure ratio and corrected design mass flow rate. FCS has the highest nominal efficiency and PD has lowest nominal efficiency.

Table E.1: Nominal performance of blades obtained by camberline design variation

Property	BASE	RC	FC
Corrected Design Mass Flow Rate	3.04 kg/s	3.04 kg/s	3.04 kg/s
Total-to-Total Pressure Ratio	1.361	1.361	1.361
Total-to-Total Efficiency	92.24%	92.05%	93.50%

Table E.2: Nominal performance of blades obtained by axial sweep design variation

Property	BASE	FAS	BAS
Corrected Design Mass Flow Rate	3.04 kg/s	3.04 kg/s	3.04 kg/s
Total-to-Total Pressure Ratio	1.361	1.361	1.361
Total-to-Total Efficiency	92.24%	92.95%	92.60%

Table E.3: Nominal performance of blades obtained by lean design variation

Property	BASE	FL	BL
Corrected Design Mass Flow Rate	3.04 kg/s	3.04 kg/s	3.04 kg/s
Total-to-Total Pressure Ratio	1.361	1.361	1.361
Total-to-Total Efficiency	92.24%	92.24%	91.95%

Table E.4: Nominal performance of blades obtained by chordwise sweep design variation

Property	BASE	FCS	ACS
Corrected Design Mass Flow Rate	3.04 kg/s	3.04 kg/s	3.04 kg/s
Total-to-Total Pressure Ratio	1.361	1.361	1.361
Total-to-Total Efficiency	92.24%	93.78%	93.30%

Table E.5: Nominal performance blades obtained by dihedral design variation

Property	BASE	ND	PD
Corrected Design Mass Flow Rate	3.04 kg/s	3.04 kg/s	3.04 kg/s
Total-to-Total Pressure Ratio	1.361	1.361	1.361
Total-to-Total Efficiency	92.24%	90.95%	92.35%

E.2 Performance and stability of very high meridional momentum design

The performance and stability of a conceptual rotor, very high meridional momentum design (VHMMT, are given in this section. First, the nominal performance of VHMMT is given in Table E.6 and the speedlines of VHMMT are plotted in Figure E.1. Since the total-to-static pressure ratio curve is almost flat, computationally, the last points of speedline are reached.

Table E.6: Nominal performance of very high meridional momentum design

Property	BASE	VHMMT
Corrected Design Mass Flow Rate	3.04 kg/s	2.97 kg/s
Total-to-Total Pressure Ratio (@ $\dot{m}_c$=3.04 kg/s)	1.361	1.361
Total-to-Total Efficiency (@ $\dot{m}_c$=3.04 kg/s)	92.24%	92.65%

Next, incoming/tip clearance flow interface is checked via entropy contours at blade tip plane at last points of speedlines for VHMMT rotor in left side of Figure E.2. As observed at all tip clearances incoming/tip clearance flow interface is almost reached to leading edge. Moreover, the boundary layer separations at blade tip plane at last points of speedlines for VHMMT rotor is also depicted on right side of Figure E.2 which shows very small separation region near leading edge. Thus, it is confirmed that VHMMT rotor is a tip critical blade.
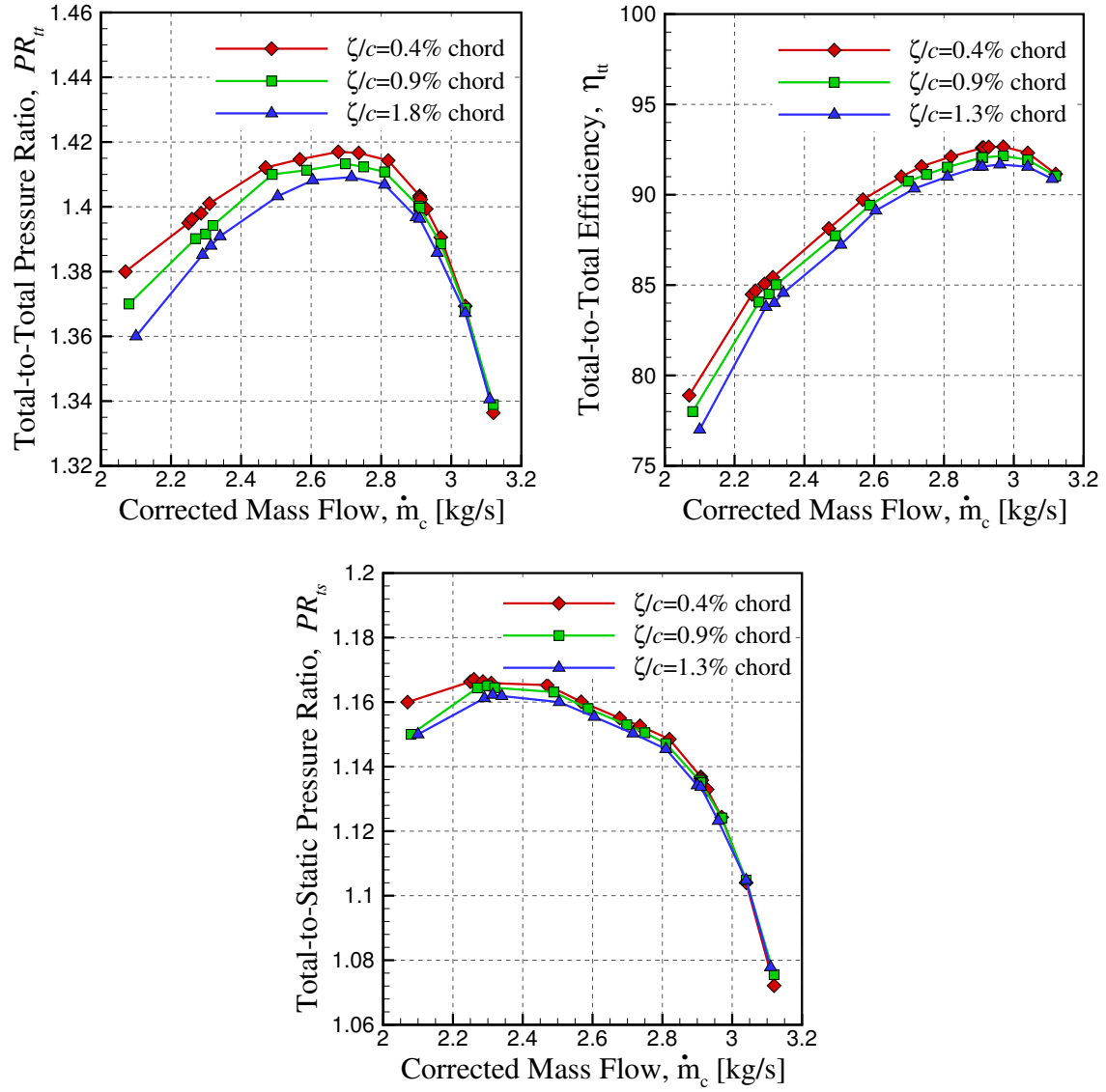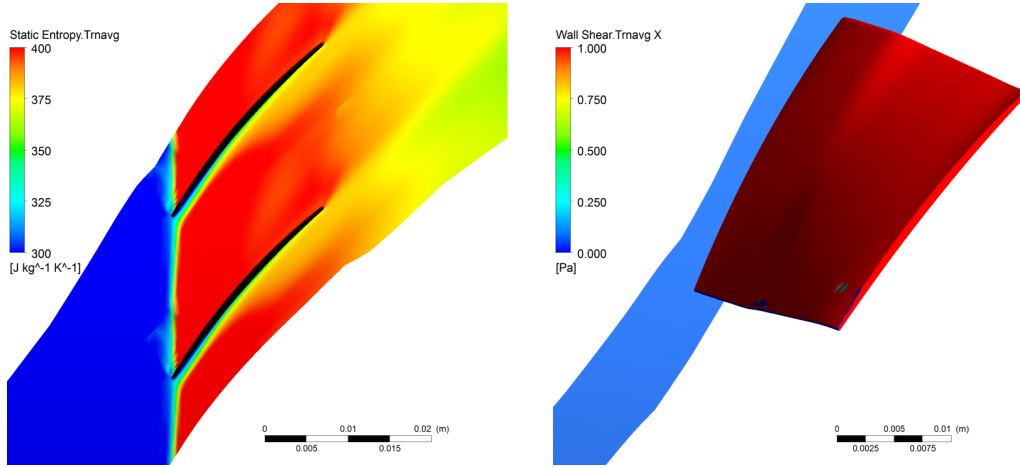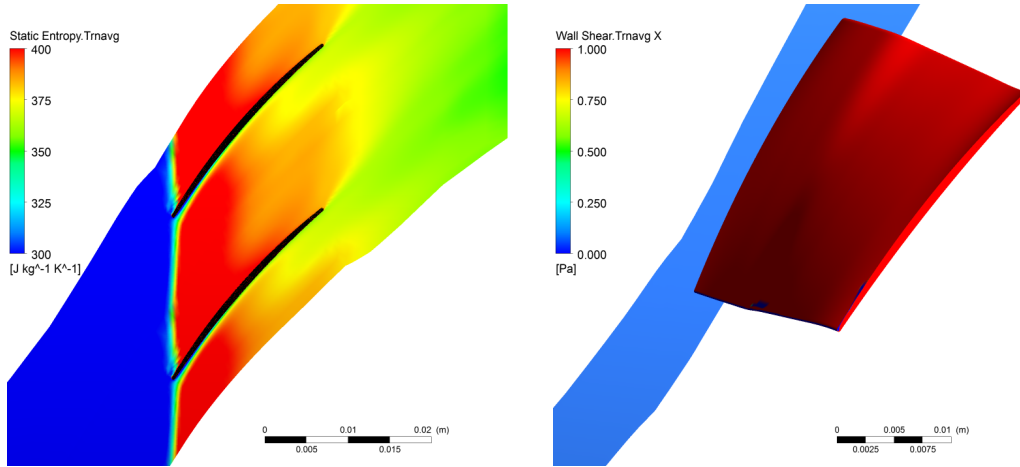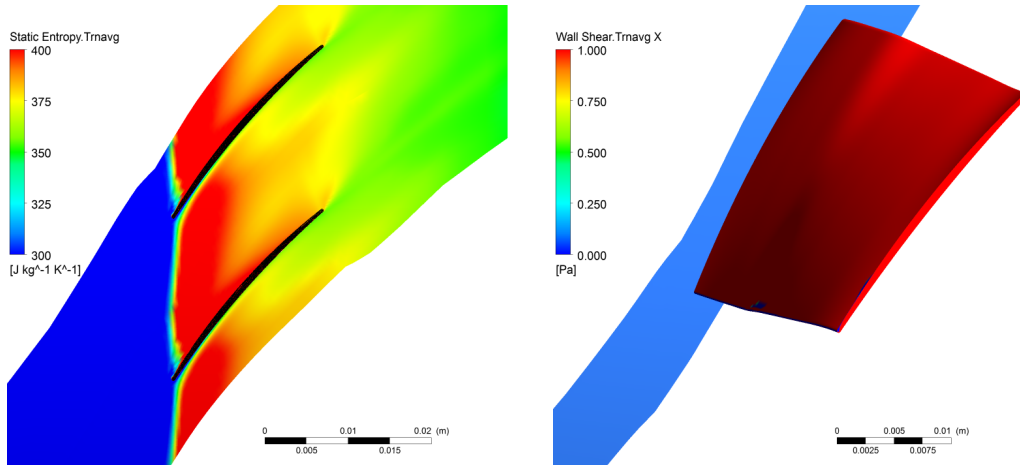
Figure E.1: Speedlines of VHMMT rotor

(a) t.c=0.005 in, $\dot{m}_{c,stall}$=2.07 kg/s

(b) t.c=0.010 in, $\dot{m}_{c,stall}$=2.08 kg/s

(c) t.c=0.015 in, $\dot{m}_{c,stall}$=2.10 kg/s

Figure E.2: Entropy contours at blade tip plane (left plots) and axial wall shear contours on blade surface (right plots) at last points of speedlines for VHMMT rotor

E.3 Performance and stability of FFCS rotor

The performance and stability of first rotor designed assessing desensitizing flow features, which is FFCS, are given in this section. First, the speedlines simulated for FFCS rotor are plotted in Figure E.3. It can be observed that computationally the last points are reached, since the slope of total-to-static pressure ratio curve is almost zero.
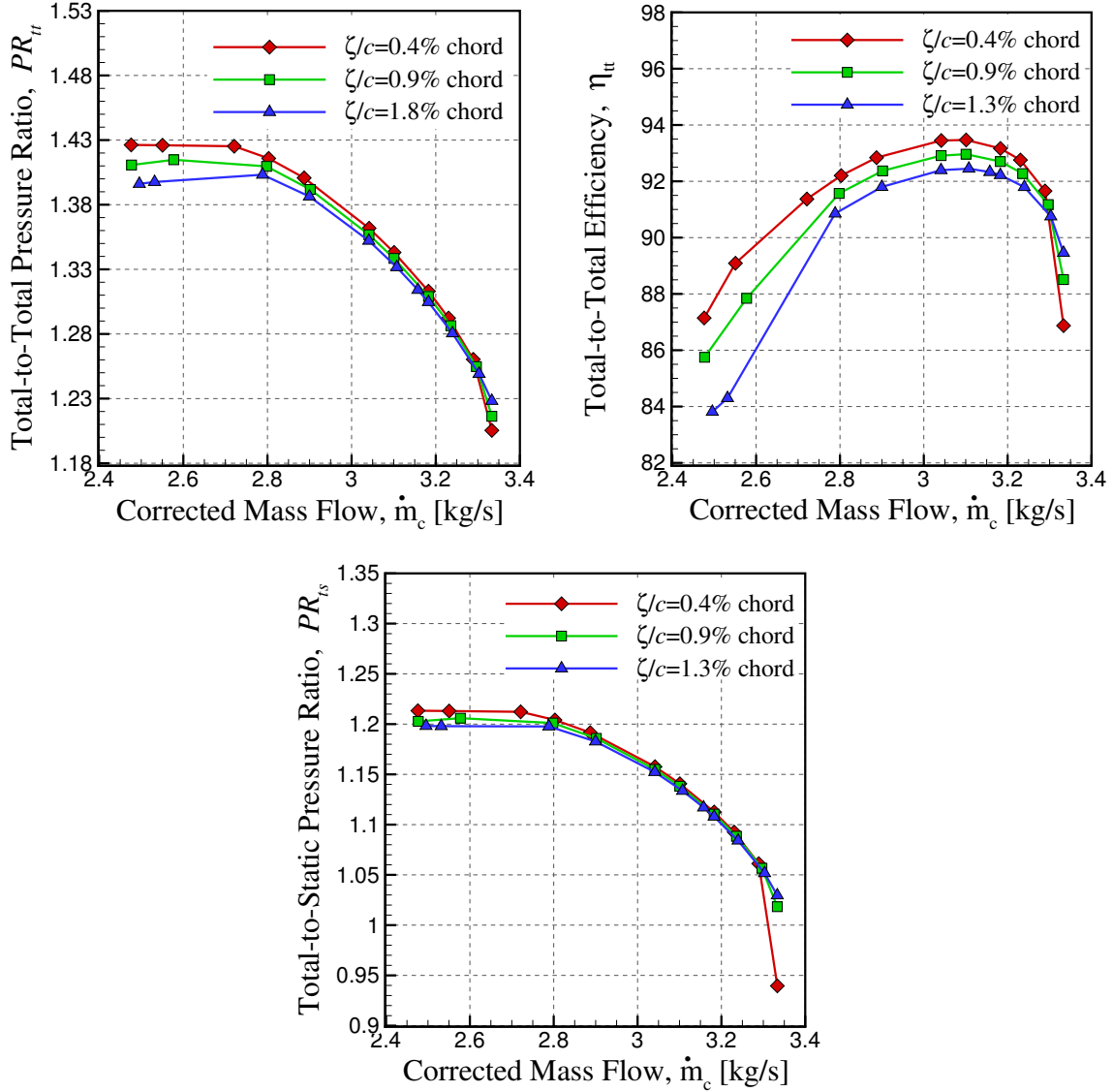
Figure E.3: Simulation of speedline for FFCS

Next, Figure E.4 plots entropy contours at blade tip plane at last points of speedlines for FFCS rotor. As observed at all tip clearances incoming/tip clearance flow interface have not reached to leading edge. Also, the boundary layer separations at blade tip plane at last points of speedlines for
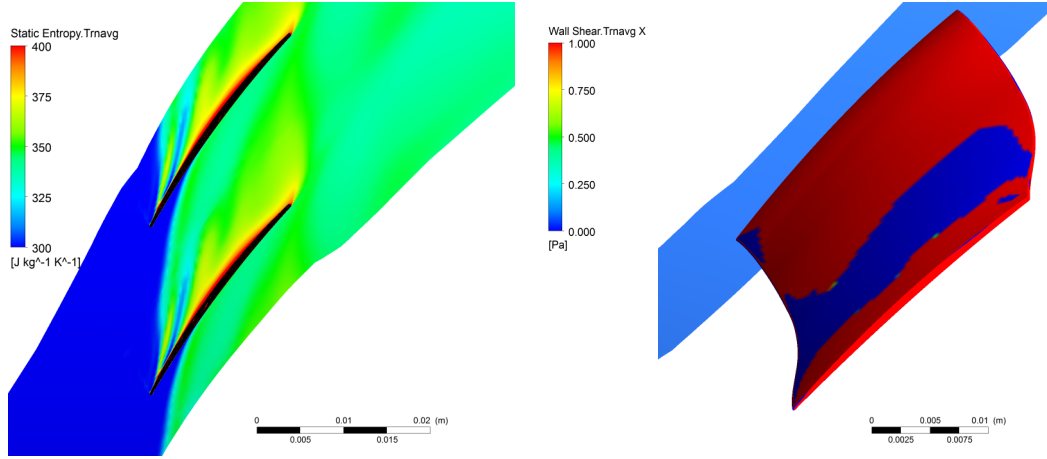
(a) t.c=0.005 in, $\dot{m}_{c,stall}$=2.46 kg/s
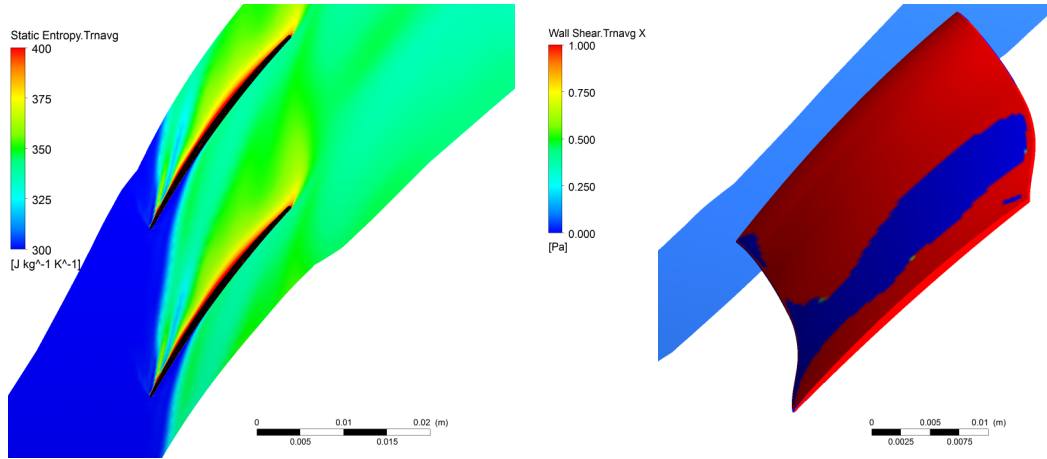
(b) t.c=0.010 in, $\dot{m}_{c,stall}$=2.47 kg/s
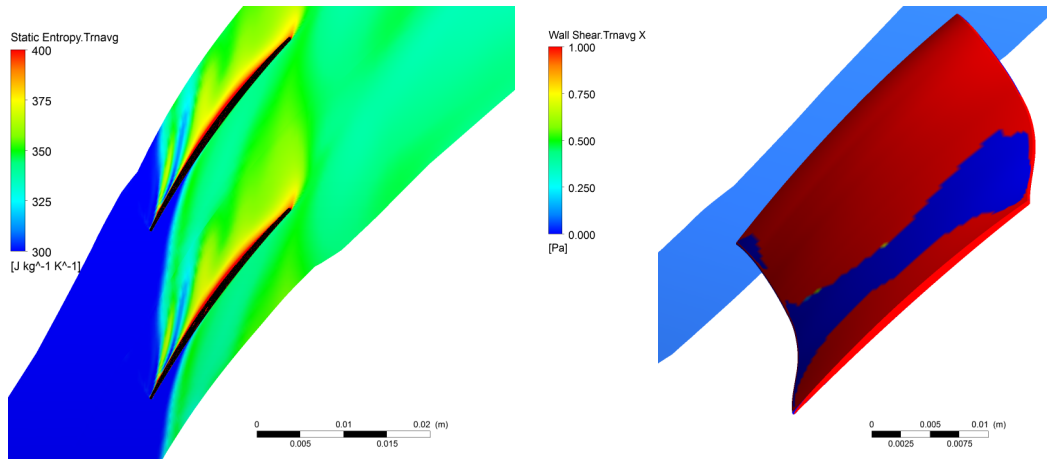
(c) t.c=0.015 in, $\dot{m}_{c,stall}$=2.49 kg/s

Figure E.4: Entropy contours at blade tip plane (left plots) and axial wall shear contours on blade surface (right plots) at last points of speedlines for FFCS rotor

FFCS rotor is also depicted in Figure E.4 which shows a blade boundary layer separation region near 80% span. Having non-zero interface position and boundary layer separation predicts that FFCS rotor is not tip critical. Therefore, a stall transient simulation is performed. In stall transient simulation as mass flow decreases the separation region expands, as shown in Figure E.5, thus, the stall occurs due to blade boundary layer separation from 80% span to blade tip. Therefore, FFCS rotor is not tip critical.

(a) $\dot{m}_c$=2.40 kg/s   (b) $\dot{m}_c$=2.30 kg/s
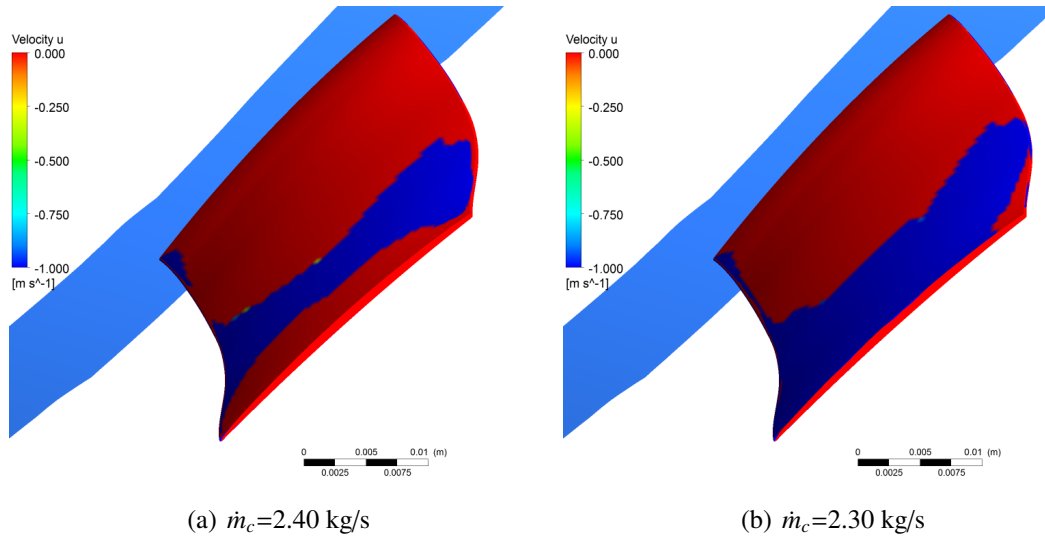
Figure E.5: Axial wall shear contours at stall transient for FFCS rotor at t.c=0.005 in

E.4   Performance and stability of PLS blade

The performance and stability of second rotor designed assessing desensitizing flow features, which is PLS, are given in this section. First, the speedlines simulated for PLS rotor are plotted in Figure E.6. It can be observed that computationally the last points are reached, since the slope of total-to-static pressure ratio curve is almost zero.

Next, Figure E.7 plots entropy contours at blade tip plane at last points of speedlines for PLS rotor. Similar to BASE rotor, at all of the tip clearances incoming/tip clearance flow interface have reached to leading edge. Also, the blade boundary layer separations at blade tip is observed in Figure E.7. Performing stall transient simulations confirms that PLS is not tip critical rotor, as shown in Figure E.8 by leading edge interface and no expansion of separation region. Therefore, the PLS rotor is tip critical.
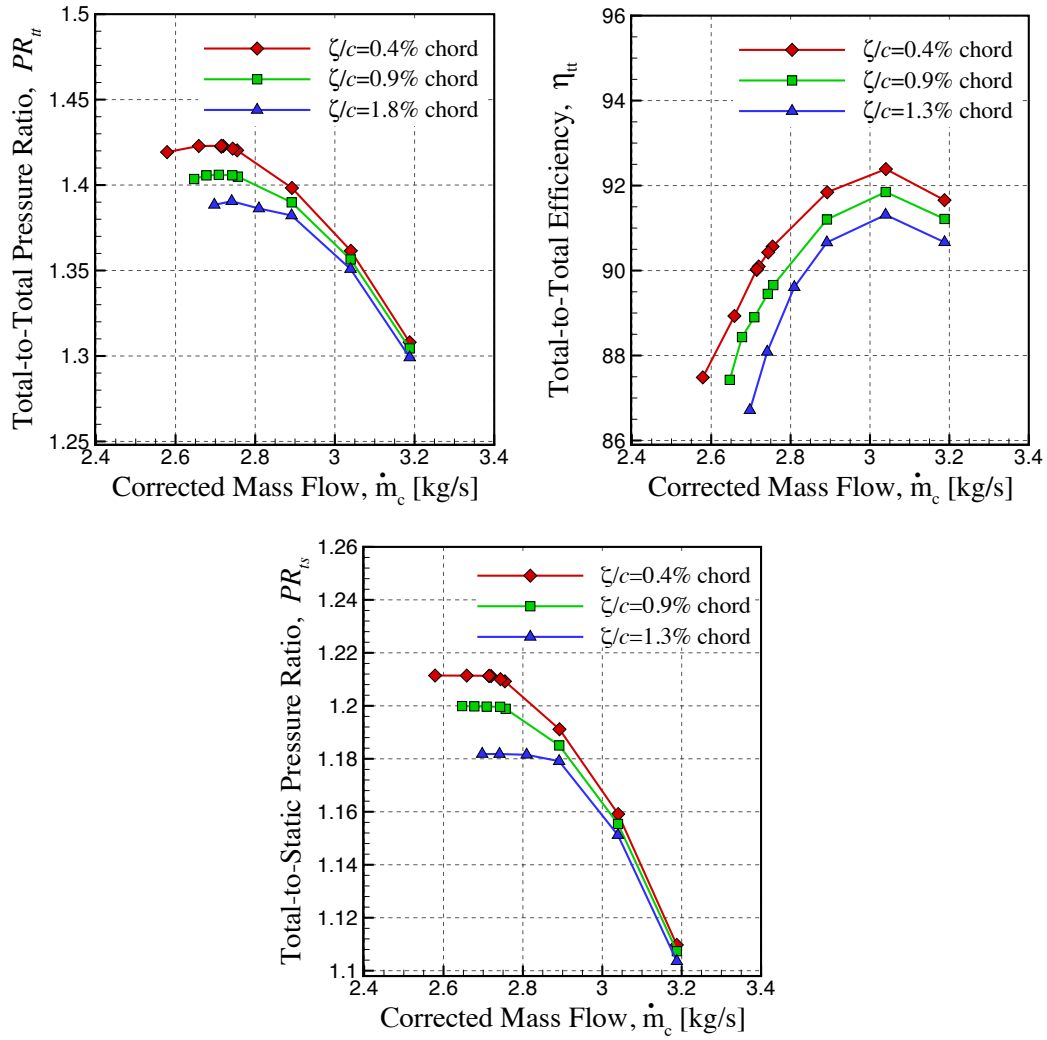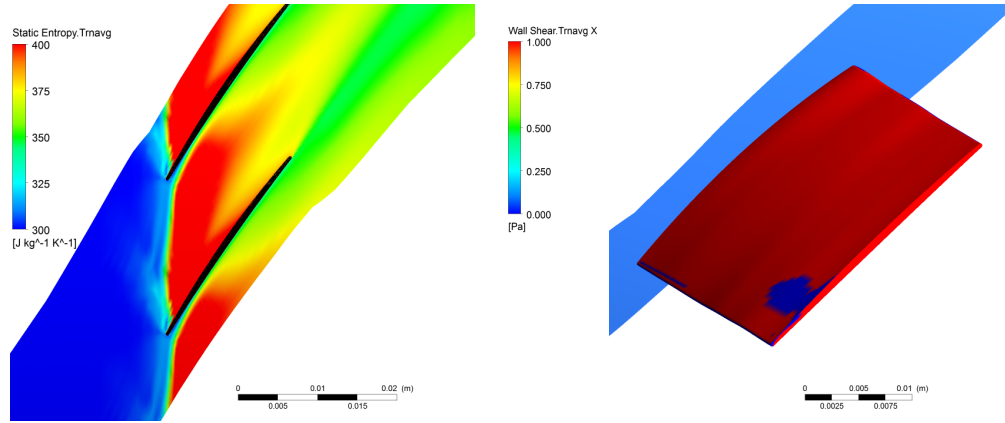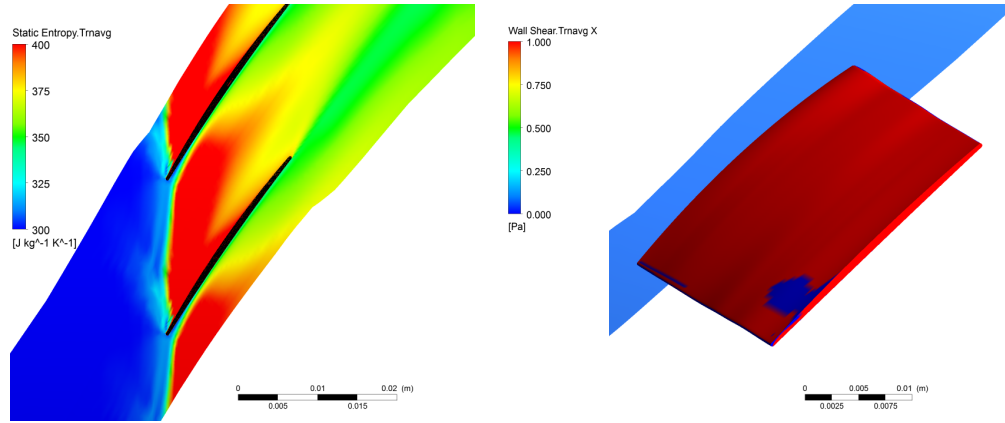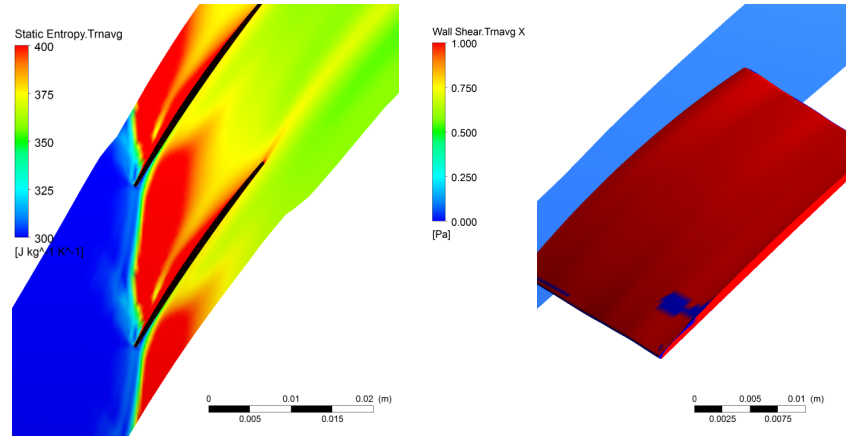
Figure E.6: Simulation of speedline for PLS rotor

(a) t.c=0.005 in, $\dot{m}_{c,stall}$=2.58 kg/s

(b) t.c=0.010 in, $\dot{m}_{c,stall}$=2.65 kg/s

(c) t.c=0.015 in, $\dot{m}_{c,stall}$=2.70 kg/s

Figure E.7: Entropy contours at blade tip plane (left plots) and axial wall shear contours on blade surface (right plots) at last points of speedlines for PLS rotor
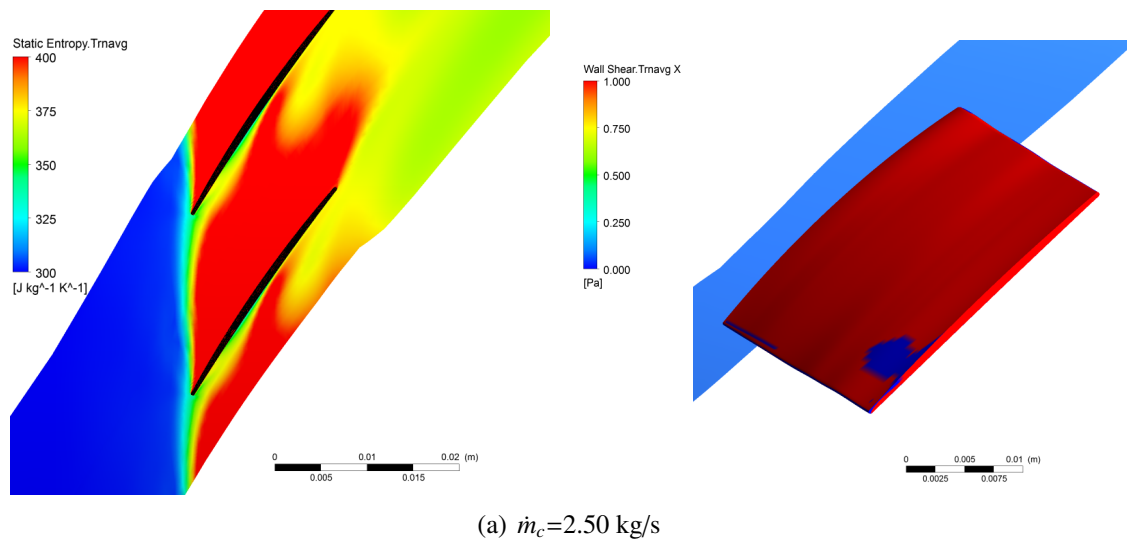
(a) $\dot{m}_c$=2.50 kg/s

Figure E.8: Incoming/tip clearance flow interface position and axial wall shear contours at stall transient for PLS rotor at t.c=0.005 in

Appendix F

Calculation of Double Leakage

To demonstrate double leakage calculation three pitch sizes (8, 6.9 and 5.8 degree or 45, 52, 62 blades) of VHMMT design is used. The simulated speedlines for these pitch sizes are shown in Figure F.1. (Tip clearances of 0.005, 0.01 and 0.015 inches corresponds to 0.4%, 0.9% and 1.3% chord, respectively.) Figure F.2 presents the tip clearance flow streamlines for these pitch sizes at corrected design (peak efficiency) mass flow, showing that even at lowest tip clearance size (0.4% chord) the smallest pitch (5.8 degree or 62-blade) design features double leakage, which can be identified by streamlines emanating from the tip clearance with markedly higher flow angle with respect to the blade suction surface.
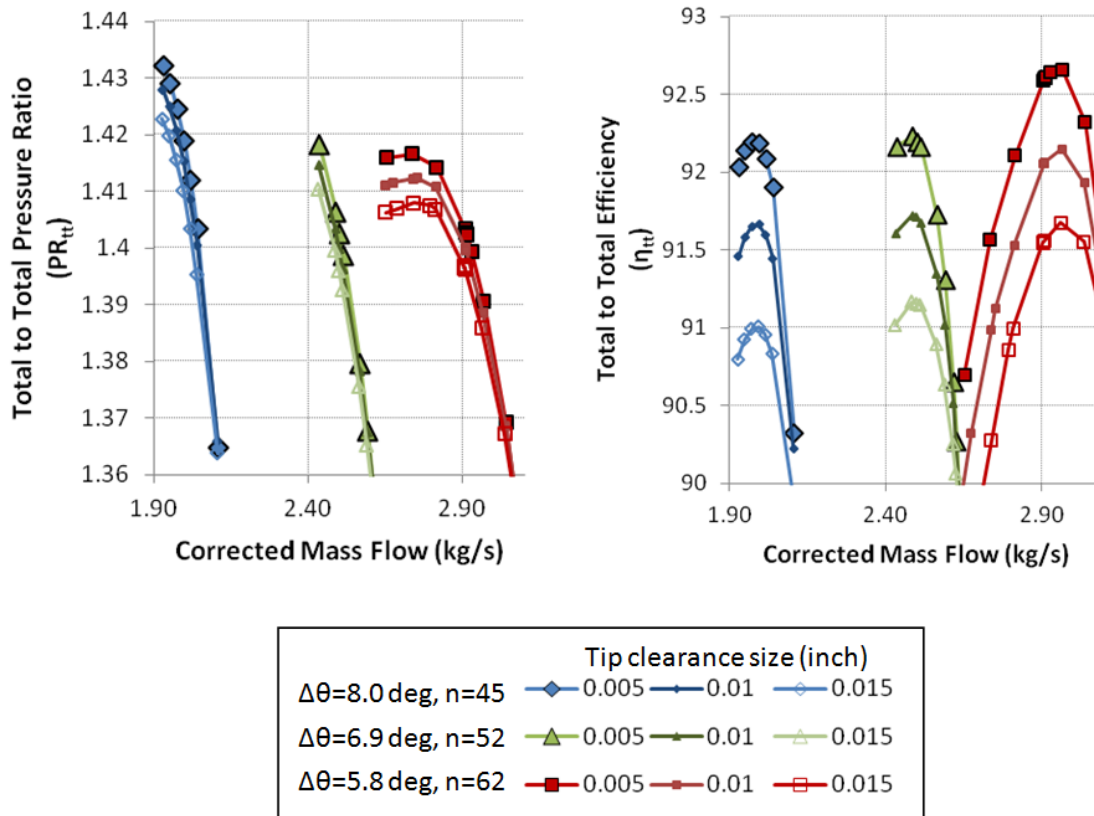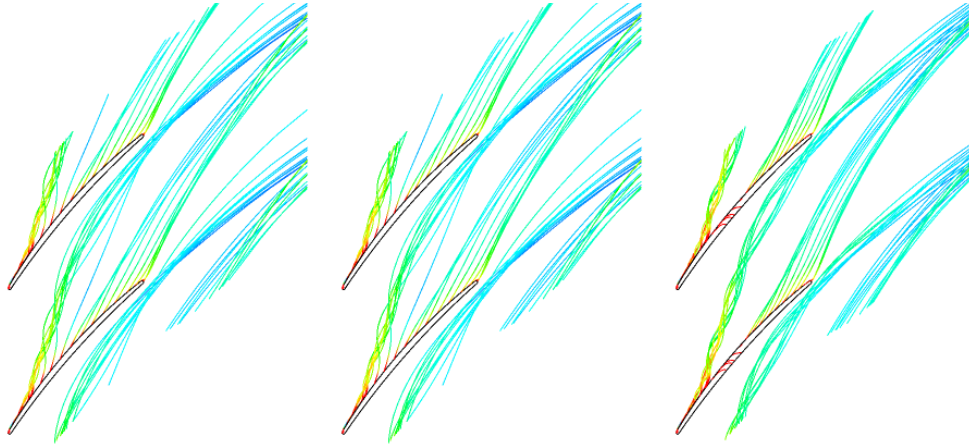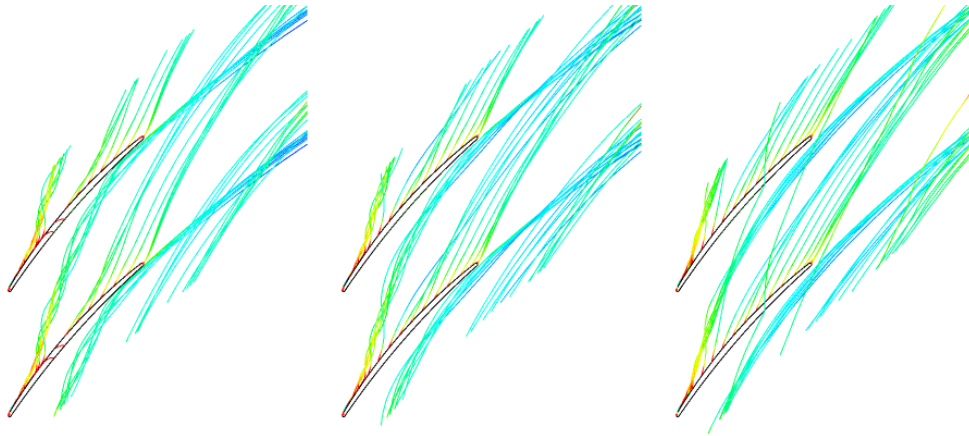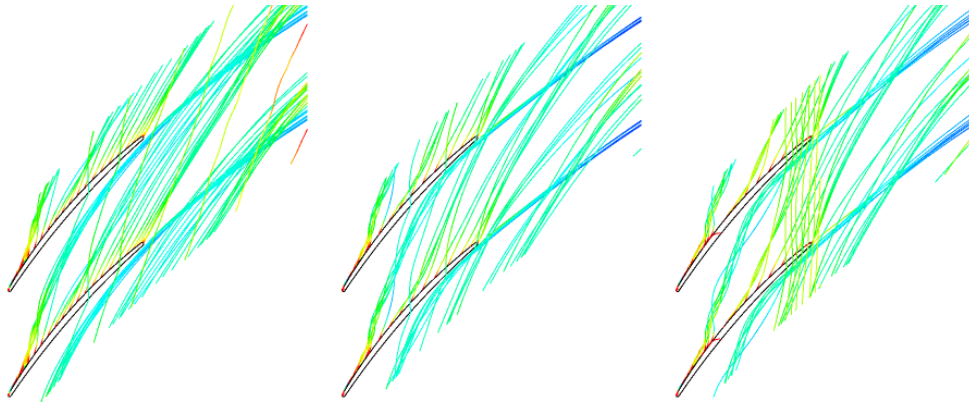

Figure F.1: Simulated speedlines for very high tip meridional momentum blade (VHMMT at three different pitch sizes (45, 52, 62 blades)

(a) 45 blades (from left to right ζ/c=0.4%, 0.9% and 1.3% chord)

(b) 52 blades (from left to right ζ/c=0.4%, 0.9% and 1.3% chord)

(c) 62 blades (from left to right ζ/c=0.4%, 0.9% and 1.3% chord)

Figure F.2: Tip clearance flow streamlines tip clearance size at three different pitch sizes for VH-MMT at corrected design (peak efficiency) mass flow

Streamlines are not practical trace for calculating double leakage mass flow rate. Therefore, another method to identify double leakage is used with streamlines. Double leaking fluid enters the tip clearance with higher entropy. Figure F.3 plots the static entropy at the tip clearance entrance for the three pitch sizes at the maximum tip clearance, showing in the 62-blade case that double-leakage is easily identified as the second peak in entropy downstream of the maximum tip leakage flow location (corresponding to the first entropy peak near blade tip). As streamlines provide the valuable information if the blade is susceptible to double leakage, the second peak entropy area (formed by double leakage) is used to identify and compute the mass flow associated with double leakage fluid.

(a) Δθ=8 deg, n=45

(b) Δθ=6.9 deg, n=52
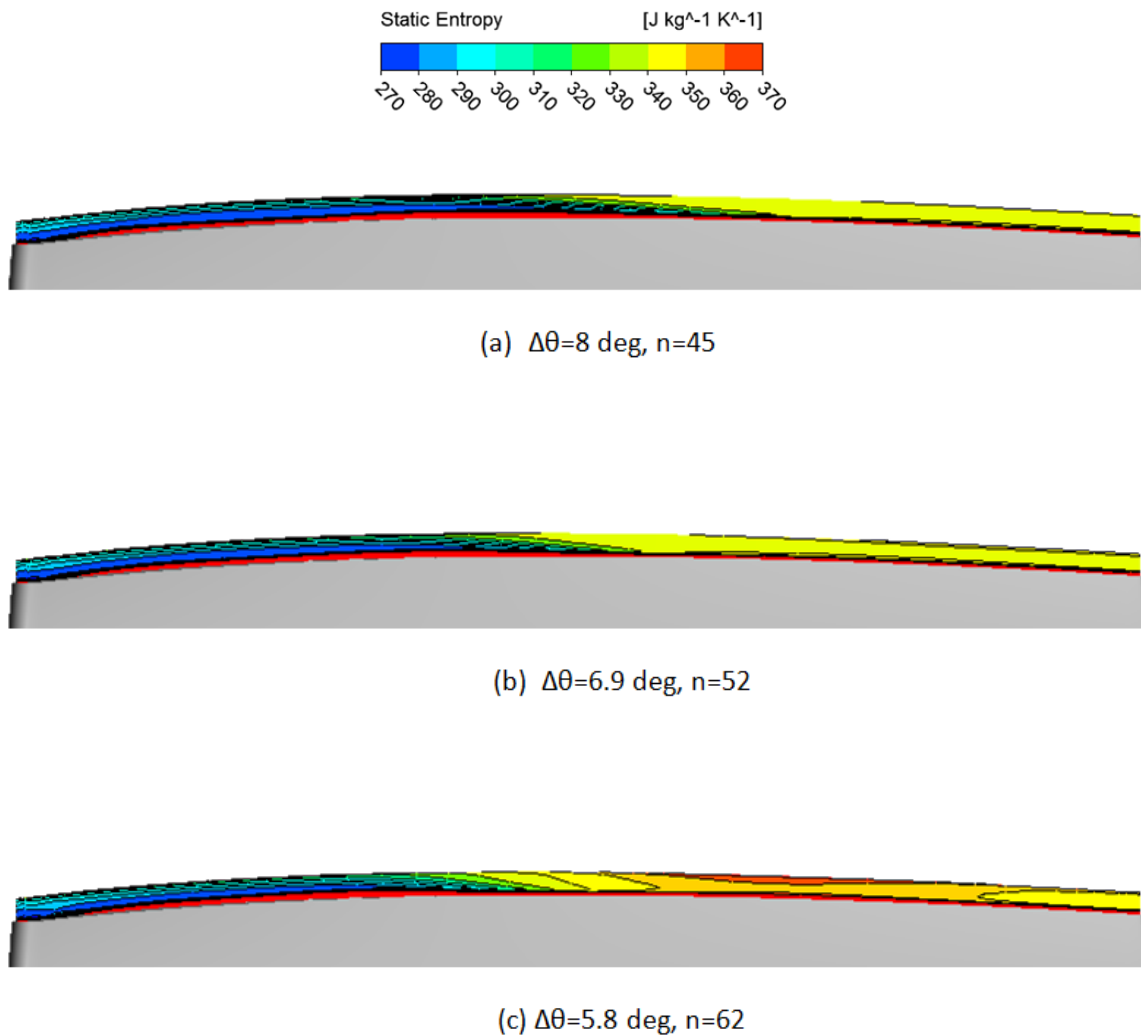
(c) Δθ=5.8 deg, n=62

Figure F.3: Contour of static entropy at tip clearance entrance at optimum efficiency and 0.015 in tip clearance for VHMMT at three pitch sizes (45, 52, 62 blades)